Plasmonic nanolipogels for combined photothermia and photodynamic therapy

Filipa Costa e Sá
Master in Applications in Biotechnology and Synthetic Biology
Department of Chemistry and Biochemistry and Biology
Faculty of Sciences of the University of Porto
2024/2025

Plasmonic nanolipogels for combined photothermia and photodynamic therapy

Filipa Costa e Sá

Dissertation carried out as part of the Master in Applications in Biotechnology and Synthetic Biology,
Department of Chemistry and Biochemistry, Department of Biology
2024/2025

Supervisor
Andreia Almeida Granja, Junior Researcher, LAQV, Requimte
Faculty of Pharmacy, University of Porto

Co-supervisor
Elisabete Maria Santos Castanheira Coutinho, Assistant Professor, University of Minho

U.PORTO
FACULDADE DE FARMÁCIA
UNIVERSIDADE DO PORTO

Universidade do Minho
Escola de Ciências

Acknowledgements

I would like to express my profound gratitude to my research supervisors, Dra. Andreia Granja and Dra. Elisabete Castanheira Coutinho, for the opportunity to work with them, for their continuous support, guidance, and availability throughout this project. Their expertise and advise were essential for my academic and personal growth.

I am profoundly grateful to Dr. Sérgio Veloso, for his kindness, his support, valuable suggestions and patience during every stage of this work. His words motivated me to overcome all the challenges that were met during the last year. It was a privilege to learn from you.

I would like to thank, Eva Marta, for the emotional support and exchange of ideas during this project. Working alongside you was a pleasure, and I truly appreciated sharing this experience with you.

I would like to thank, Ana Paula, Ricardo, Raquel, Maria João, Rui and all the laboratory colleagues for the kind words, patience and the friendly environment that made the day-to-day work much more enjoyable.

I want to thank all the friends I made during the Master, especially Beatriz, Pedro, Aimone, Filipe, Daniel, David and Inês, for making the last two years worth it. I thank you for all the dinners, the good moments and the friendship. It wouldn't be the same without all of you.

I would like to express my deepest gratitude to my parents and my brother, for their unconditional love, patience, and encouragement throughout this journey. Their support and belief in me provided the strength and motivation needed to complete this work. I am truly thankful for their support in every step, as this accomplishment would not have been possible without them. I want to extend my gratitude to my friend Barbara for her constant positivity and willingness to listen that made the toughest moments easier to face.

I wish to acknowledge the Center of Physics of the University of Minho and Porto (CF-UM-UP) and the LAQV/ Requimte of the Faculty of Pharmacy of the University of Porto for providing the resources and access to the space to carry out this research work.

Resumo

O cancro é uma das principais causas de mortalidade e morbidade em todo o mundo. Atualmente, os pacientes de cancro são tratados através de terapias tradicionais, como a quimioterapia, que causam vários efeitos secundários, uma vez que não são específicos para os tecidos tumorais.

A nanotecnologia e os nanomateriais têm vindo a surgir como uma solução para contornar alguns problemas presentes na biomedicina atual. Os nanogeis têm sido estudados devido às suas propriedades físico-químicas e à sua biocompatibilidade.

Neste trabalho, um nanogel plasmónico carregado com mitoxantrona e 2-deoxy-D-glucose foi desenvolvido com o objetivo de ser aplicado para terapia combinada do cancro. O nanossistema foi completamente caracterizado por técnicas espetroscópicas e por microscopia eletrónica, tendo sido testado para o transporte e entrega controlada e sequencial de dois fármacos diferentes. O uso de um nanogel tem como finalidade melhorar a biodisponibilidade dos fármacos no local do tumor, evitando a sua ação em tecidos saudáveis. Para além disso, a sua libertação controlada permite diminuir a toxicidade e a dose de fármaco necessária. Por outro lado, as partículas plasmónicas têm a capacidade de converter radiação NIR em calor, tornando as células mais sensíveis à ação dos fármacos e permitindo atingir uma libertação sequencial dos diferentes fármacos, através da sensibilidade a diferentes estímulos endógenos e exógenos.

Os resultados obtidos indicam que o sistema desenvolvido tem potencial para ser usado como agente de terapia multimodal do cancro, uma vez que não provocou efeitos citotóxicos em diferentes linhas celulares testadas, apresenta uma boa capacidade de encapsulação de fármacos e de conversão fototérmica, aumentando a eficiência da ação antitumoral.

Palavras-chave: Terapia combinada do cancro, nanogéis, partículas plasmónicas, entrega de fármacos.

Abstract

Cancer is one of the leading causes of mortality and morbidity worldwide. Currently, cancer patients are treated with traditional therapies such as chemotherapy, which cause several side effects due to their lack of specificity for tumor tissues.

Nanotechnology and nanomaterials have emerged as promising solutions to overcome some of the limitations of current biomedical approaches. Among them, nanogels have been studied due to their physicochemical properties and high biocompatibility.

In this work, a plasmonic nanogel loaded with mitoxantrone and 2-deoxy-D-glucose was developed with the aim of being applied in combined cancer therapy. This system was thoroughly characterized using spectroscopic techniques and electron microscopy, and it was tested for the controlled and sequential delivery of two different drugs. The use of a nanogel aimed to improve the bioavailability of the drugs at the tumor site, avoiding their action on healthy tissues. Moreover, its controlled release reduces both toxicity and the required drug dose. In addition, the plasmonic particles have the ability to convert near-infrared (NIR) radiation into heat, making cancer cells more sensitive to the drugs and enabling the sequential release of different therapeutic agents in response to various endogenous and exogenous stimuli.

The results indicate that the developed system has potential to be used as a multimodal cancer therapy agent, as it did not cause cytotoxic effects in the tested cell lines and showed good drug encapsulation capacity and photothermal conversion efficiency, enhancing the antitumor effect.

Keywords: Combined therapy of cancer, nanogels, plasmonic particles, drug delivery.

Table of Contents

List of Tables vii

List of Figures viii

List of Abbreviations x

1. Introduction 1

1.1. Cancer 1

1.2. Nanotechnology 1

1.3. Nanogels 1

1.3.1. Chitosan nanogels 2

1.3.2. Alginate nanogels 5

1.3.3. Alginate-chitosan nanogels 7

1.3.3.1. Drug delivery applications 8

1.4. Nanoparticles 9

1.4.1. Plasmonic nanoparticles 10

1.4.1.1. Mesoporous silica coating 12

1.4.1.2. Liposomes coating 13

1.5. Plasmonic nanolipogels 16

1.6. Mitoxantrone 17

1.7. 2-Deoxy-d-glucose 18

1.8. Combination therapy 20

2. Experimental Section 22

2.1. Development of the plasmonic nanolipogels 22

2.1.1. Preparation of plasmonic particles 22

2.1.1.1. Synthesis of AuNRs 22

2.1.1.2. AuNRs' coating with mesoporous silica 23

2.1.1.3. Addition of lipid bilayer 23

2.1.1.4. Characterization of the plasmonic nanoparticles 23

2.1.2. Preparation of the plasmonic nanogels 24

2.1.2.1. Modification of chitosan 24
2.1.2.2. Preparation of the nanogel formulation 24
2.1.2.3. Characterization techniques 25
2.2. Drug release assays 27
2.2.1. Drug loading 27
2.2.2. Release assays 27
2.3. *In vitro* assays 28
2.3.1. Cell culture 28
2.3.2. Cell viability assay 28
2.3.3. Cellular uptake assays 29
3. Results and Discussion 29
3.1. Development of plasmonic nanolipogels 29
3.1.1. Preparation of plasmonic particles 29
3.1.2. Development of modified nanogels 32
3.2. Drug release assays 40
3.3. *In vitro* assays 43
3.3.1. Cytotoxicity assays 43
3.3.2. Cellular uptake 45
4. Conclusions 46
5. Future perspectives 47
6. References 49

List of Tables

Table 1. CS-CYS:Alg:TPP formulations tested. 25
Table 2. Visual observations of the obtained nanogel's formulations. With aggregates (X) or without aggregates (Ø). 35

List of Figures

Figure 1. Chitosan's structure, functional groups and possible chemical modifications. Carbon 2 is highlighted. Adapted from *Aranaz et al, 2021* [33]. 4
Figure 2. Possible molecular structures of alginate polymer chains. Adapted from *Paques J. et al, 2014* [54]. 5
Figure 3. Scheme of cross-linking of alginate with the formation of "*egg-box*" structures with a divalent cation, Ca^{2+}. Adapted from *Paques J. et al, 2014* [54]. 6
Figure 4. Scheme of the electron charge cloud oscillation of a sphere under an electric field. Adapted from *E. Hutter et al, 2004* [107]. 11
Figure 5. Molecular structure of TEOS. 13
Figure 6. Schematic image of liposome structure with cholesterol. Adapted from *Nsairat et al* [129]. 14
Figure 7. Molecular structures of DPPC and cholesterol. Adapted from *Victoria M. Katata et al, 2022* [136] 15
Figure 8. Structure of mitoxantrone. 17
Figure 9. Molecular structure of glucose and 2DG. Adapted from *Jyostna Bere et al, 2021* [170]. 19
Figure 10. Effects of 2DG uptake on the cell: glycolysis pathway; synthesis of glycoproteins. Adapted from Zhang D. et al [167] 20
Figure 11. Scheme of the proposed nanosystem. 21
Figure 12. Apparatus for AuNRs synthesis. (1) round bottom flask,, (2) utility clamp, (3) AuNRs solution. 22
Figure 13. Photographic register of the (A) AuNRs suspension in water and (B) AuNRs@Si in ethanol. 30
Figure 14. (A) Absorption spectra of AuNRs and AuNRs@Si dissolved in ultrapure water, in 1:10 ratio. (B) TEM image of AuNRs and of (C) AuNRs@Si. 31
Figure 15. Reaction scheme for the conjugation of chitosan with L-cysteine. 32
Figure 16. FTIR spectra of CS (blue) and CS-CYS (black) 33
Figure 17. Raman spectra of chitosan (black), CS-CYS (red), alginate (blue) and the nanogel (green). 34
Figure 18. Photographic register of the nanogels with 0.1% alginate, 0.1% CS-CYS and different concentrations of TPP: 0.025%, 0.05%, 0.2% and 0.4% (from left to right). .. 36
Figure 19. DLS characterization of the different formulations of nanogel. Zeta potential in absolute value (A) and hydrodynamic diameter (B) values. Concentrations assessed: CS-CYS 0.035-0.35 mg/mL; Alginate 0.025-0.4 mg/mL; TPP 0.1%. 37

Figure 20. DLS characterization, zeta potential (A) and hydrodynamic diameter (B) of the nanogel at different pH conditions pH 3-9. 38
Figure 21. Hydrodynamic size characterization of the nanogel upon the increase of the temperature. Measurements were taken under 2ºC intervals, from 25 ºC to 51 ºC. 39
Figure 22. Hydrodynamic size characterization of the nanogel upon heating cycles (50ºC) and cooling cycles (25ºC), at different pH levels (pH 6 and 7.4). 40
Figure 23. Photographic register of the nanogels 20 μM, 80 μM and 10 mM (from left to right) of GSH, at the 144 hours' time point. 41
Figure 24. Characterization of the nanogel, zeta potential (A) and hydrodynamic diameter (B) measurements, during the redox sensitivity assay. $H2O2$ was added to the nanogel after the first mesaurement; GSH was added after 24 hours of incubation with $H2O2$. DLS measurements were performed at different time point, until 144 hours. 1
Figure 25. Storage stability of the nanogel at different temperatures, 37 ºC, 25 ºC and 5 ºC. Zeta potential (A) and hydrodynamic diameter (B) measurements of the nanogel were performed over 30 days. 38
Figure 26. Size and zeta (ζ) potential characterization of AuNRs, AuNRs@Si, AuNRs@Si@Lip, NGs@NPs and NGs. 39
Figure 27. SEM images of empty nanogel (A); scale bar 2 μm. SEM (B) and STEM (C) images of plasmonic nanogel; scale bar 500 nm and 2 μm, respectively. 40
Figure 28. *In vitro* release profiles of MTX from the plasmonic nanogels, over 72h, at pH 7.4 (A) and 6 (B) at different conditions (10 mM GSH and 808 nm laser irradiation). The assays were performed at room temperature and in triplicate. 40
Figure 29. *In vitro* release profiles of CF from the plasmonic nanogels, over 72 h, at pH 7.4 (A) and 6 (B) at different conditions (10 mM GSH and 808 nm laser irradiation). The assays were performed at room temperature and in triplicate. 42
Figure 30. Evaluation of the metabolic activity of L929, determined by the resazurin assay. The cells were treated with different concentrations of the unloaded and loaded system with MTX; 2DG and 2DG+ MTX. The assays were performed in triplicate. 43
Figure 31. Evaluation of the metabolic activity of MDA-MB-231, determined by the resazurin assay. The cells were treated with different concentrations of the unloaded and loaded system with MTX; 2DG and 2DG+ MTX. The assays were performed in triplicate. 44
Figure 32. MDA-MB-231 cellular uptake of 2DG + MTX loaded nanogels after 1 hour and 3 hours of incubation visualized by confocal microscopy. The scale bar corresponds to 50 μm. 45

List of Abbreviations

FCUP	FACULTY OF SCIENCES OF THE UNIVERSITY OF PORTO
UP	UNIVERSITY OF PORTO
2DG	2-DEOXY-D-GLUCOSE
2DG-6P	2-DEOXY-D-GLUCOSE-6-PHOSPHATE
ATP	ADENOSINE TRIPHOSPHATE
AUNRS	GOLD NANORODS
AUNRS@SI	SILICA-COATED GOLD NANORODS
AUNRS@SI@LIP	LIPID AND SILICA-COATED GOLD NANORODS
CF	CARBOXYFLUORESCEIN
CLSM	CONFOCAL LASER SCANNING MICROSCOPY
CS-CYS	CYSTEINE MODIFIED CHITOSAN
CTAB	CETYLTRIMETHYLAMMONIUM BROMIDE
DLS	DYNAMIC LIGHT SCATTERING
DMEM	DULBECCO'S MODIFIED EAGLE MEDIUM
DNA	DEOXYRRIBONUCLEIC ACID
DPPC	DIPALMITOYLPHOPHATIDYLCHOLINE
EDC	1-ETHYL-3-(3-DIMETHYLAMINOPROPYL)CARBODIIMIDE
EPR	ENHANCED PERMEABILITY AND RETENTION
FDA	FOOD AND DRUG ADMINISTRATION
FTIR	FOURIER-TRANSFORM INFRARED SPECTROSCOPY
GSH	GLUTATHIONE
LCST	LOWER CRITICAL SOLUTION TEMPERATURE
LSPR	LONGITUDINAL SURFACE PLASMON RESONANCE
MTX	MITOXANTRONE
PDI	POLIDISPERSITY INDEX
RNA	RIBONUCLEIC ACID
SEM	SCANNING ELECTRONIC MICROSCOPY
SPR	SURFACE PLASMON RESONANCE
STEM	SCANNING TRANSMISSION ELECTRONIC MICROSCOPY
TEM	TRANSMISSION ELECTRONIC MICROSCOPY
TEOS	TETRAETHYL ORTHOSILICATE
TPP	TRIPOLYPHOSPHATE
TSPR	TRANSVERSAL SURFACE PLASMON RESONANCE

1. Introduction

1.1. Cancer

Cancer is one of the deathliest diseases in the world, responsible for at least 1 in 6 deaths worldwide. This disease is characterized by the abnormal rate of division of cells due to mutations in the genes related to growth, cell division and proliferation [1]. In 2022, approximately 20 million new cases were diagnosed, and 10 million deaths were reported [1]. Breast cancer is the most incident cancer among women and the number of new cases is predicted to keep increasing [2]. Traditional cancer therapies, such as surgery, radiotherapy and chemotherapy, have many disadvantages as they do not target the tumor cells, and therefore they cause damage in healthy cells. Besides, drug resistance and drug degradation are also important issues to consider when chemotherapy is used [3]. Nanotechnology is emerging as a solution to improve the outcomes of traditional therapies [4]. Nanoparticles can be used as carriers, encapsulating chemotherapeutic drugs, targeting cancer cells, passively or actively [5]. Their use as nanocarriers has shown to prevent the drug's degradation and improve their half-life in the system [6]. Moreover, nanoparticles can be used as therapeutic agents, for photothermal therapy [7].

1.2. Nanotechnology

In 1959, during the American Physical Society's meeting, *Richard Feynman* introduced the concept of nanotechnology. Since then, several advances concerning this topic have been made, and nowadays, nanotechnology is one the most promising areas to provide solutions to many unsolved problems. However, while reports of nanotechnological devices in medicine, energy and industry, are exponentially increasing, there are still some concerns regarding their environmental impact, the scalability of their synthesis and some ethical issues [8], [9].

1.3. Nanogels

The first nanogel report, described in 1993 by *Akiyoshi*, was a physically self-assembled glucose polysaccharide and cholesterol network, in water [10], and since then, this type of particles have been shown to be useful for various purposes such as drug delivery, biosensing, biocatalysis, imaging, among others [11], [12], [13], [14].

Nanogel defines a chemically or physically three-dimensional cross-linked polymer network at a nanoscale range. It combines the characteristics of hydrogels and nanoparticles and can be classified based on the nature of its polymer composition, that

can be natural, synthetic, or a combination of both [15]. Their size allows for an easier crossing through biological barriers, due to the enhanced permeability and retention (EPR) effect present in solid tumors [16], [17]. Besides, the softness of nanogels also contributes for an increased penetration in tumors [16]. Regarding the surface charge of the particles, in some cases, positively charged nanoparticles showed better intracellular uptake [18]. However, in general, the surface charge seems not to have a significant impact on the EPR effect [16]. Depending on its composition, the nanogel will have different characteristics and properties, such as surface area, charge, swelling ability, biodegradability, biocompatibility, stability, and responsiveness. Physically cross-linked nanogels are formed through polymer non-covalent interactions, such as hydrophobic interactions and electrostatic interactions between opposite charged groups [19]. On the other hand, chemically cross-linked nanogels are usually synthesized by the formation of covalent bonds, like disulfide bonds, between the polymer groups [19]. Nanogels are synthesized through different methods, depending on the desired characteristics and the type of polymers. The synthesis begins with monomers or polymer precursors and it is usually based on crosslinking or sequential polymerization reactions. This cross-linked network provides the nanogel with the ability to swell or shrink, while conserving its structure or dispersing in the medium, in the case of physically cross-linked nanogels.

The swelling of nanogels depends on its structure and composition, and also on external factors that can be physical or chemical, such as light, magnetic field, ionic strength, temperature, pH, redox environment, or the presence of a certain compound or enzyme [20], [21]. This expansion or shrinkage of the network is the main approach when the use of this type of nanomaterials as carriers is considered, as it allows a more predictable behavior of the material and a controlled diffusion of the nanogel's content to the solvent [21].

1.3.1. Chitosan nanogels

Nanogels composed of natural polymers such as polysaccharides are usually more biocompatible and biodegradable. Additionally, they can be easily surface modified and have high water retention ability. Although they have many advantages over synthetic nanogels, they also have less reproducibility and higher variability between syntheses [22].

Chitin is one of the most abundant biopolymers and can be found in the cell wall of fungi, algae and in the exoskeleton of crustaceans. Chitosan is a natural cationic polysaccharide obtained from the deacetylation of chitin and composed of glucosamine and N-acetyl-glucosamine residues (Figure 1) [23]. Besides being a natural sourced,

non-toxic, biocompatible, and biodegradable polymer, chitosan possesses other characteristics, such as antibacterial and antifungal activities and bioadhesion, advantageous for the application in various areas, such as industry, energy, materials and biomedicine.

Chitosan can be used to form nanogels through self-assembly, ionic gelation, microemulsion, radical polymerization, either as a therapeutic agent or carrier [24], [25], [26]. Due to the use of non-harmful reagents and mild conditions, ionic gelation is one of the most used methods to produce chitosan nanogels. The addition of a negative cross-linker, a counter ion, like tripolyphosphate (TPP), to the polymer, in acidic medium, initiates a spontaneous reaction between the opposite charged groups and triggers gel formation, resulting in a gel-like network precipitate [27], [28], [29]. This method, using TPP as a cross-linking agent was first described in 1997 by *Calvo et al* [30], when a suspension of chitosan-polyethylene oxide particles was developed to encapsulate bovine serum albumin. The size of the nanogel can be tuned by altering the concentration of TPP, the pH and the chitosan's acetylation degree [31].

Chitosan has been applied in the production of nanogels due to its tissue-healing properties, and pH-sensitiveness enabling a sol-gel transition[32]. This polymer is insoluble in water but soluble in acidic aqueous medium due to the protonation of its primary amine on C2 (pK_a 6.5) (Figure 1), allowing interactions with the solvent [33]. This protonation of the polymer provides it with the ability to interact and form complexes, nanoparticles or hydrogels/nanogels with negatively charged compounds, such as DNA and proteins [34]. On the other hand, at neutral pH, the polymer charge density is reduced, which leads to lower solubility and consequent aggregation. Besides the free amino groups on its backbone, it has also two hydroxyl groups (C3 and C4) that can be chemically modified, to achieve a polymer with different characteristics or to expand its properties, like improved biodegradability [35], [36], [37]. The thiolation of chitosan is a very commonly used modification that usually occurs by chemically modifying chitosan's primary amine with a free thiol molecule [38], [39], [40], [41], [42], [43]. This modification can improve mucoadhesion, permeation, bioavailability and biodegradability of the nanogel, compared to the non-modified polymer particles. Liu et al.[39], used chitosan-N-acetylcysteine to increase curcumin's penetration and retention time in the precornea and cornea, improving its efficacy through the interaction of the thiol groups with the mucus[44]. Besides, chitosan can be modified to endow nanogels or nanoparticle coatings with responsiveness to different stimulus. Thioglycolic acid modified-chitosan

was used as a gate-keeper to control quercetin diffusion through the pores of mesoporous silica particles [45].

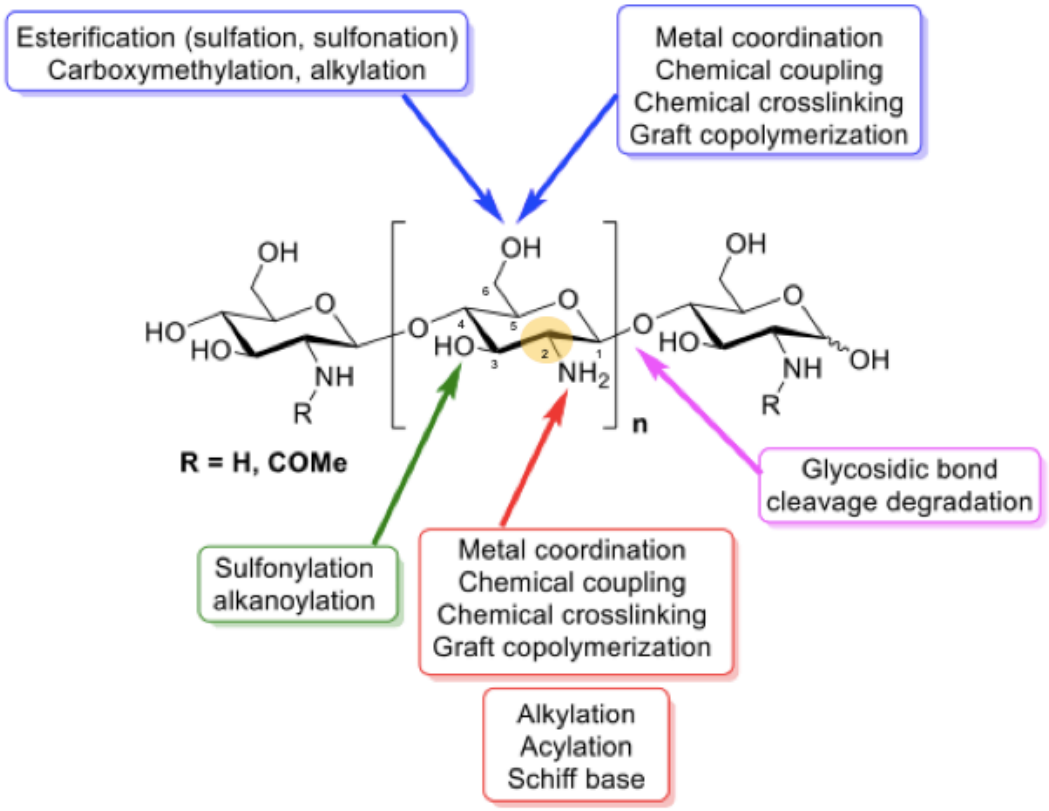


Figure 1. Chitosan's structure, functional groups and possible chemical modifications. Carbon 2 is highlighted. Adapted from *Aranaz et al, 2021* [33].

Chitosan nanogels can be used for several purposes, such as intracellular delivery. A study on the effect of the surface charge of chitosan nanoparticles on cellular uptake was performed by *Yue Z. et al* [46]. Due to their positive charge, chitosan nanoparticles can interact with the negatively charged cell membranes, and increase the cellular uptake, comparing with neutral or negative nanoparticles [46], [47]. There are reports that support that this conclusion can be extended to chitosan nanogels as well [48]. Chitosan nanogels are efficient at protecting drugs from being metabolized or eliminated from the system, increasing their bioavailability. Chitosan nanogels can be used as delivery agents for antitumor drugs, such as doxorubicin, 5-fluorouracil and methotrexate [49], [50], [51]. Their use can also be extended for the delivery of other therapeutic agents, like anti-inflammatory bioactives for the inhibition of inflammation processes [52].

Although chitosan nanogels are very promising, they still have some limitations, like poor solubility at physiological conditions, rapid clearance from the blood circulation and low mechanical strength and stability (as it dissolves at low pH) [53].

1.3.2. Alginate nanogels

Alginate is a natural anionic polysaccharide that can be found in brown algae and in some strains of bacteria and is composed of linear chains of residues of β-D-mannuronate (M) and α-L-guluronate (G) (Figure 2). The polymer chains can be homopolymeric (containing only one of the residues) or interposed with heterosequences (Figure 2). Its composition makes it a versatile polymer, that can be used in several ways for biomedical applications, as it is highly biocompatible, easily functionalized, and able to form hydrogels.

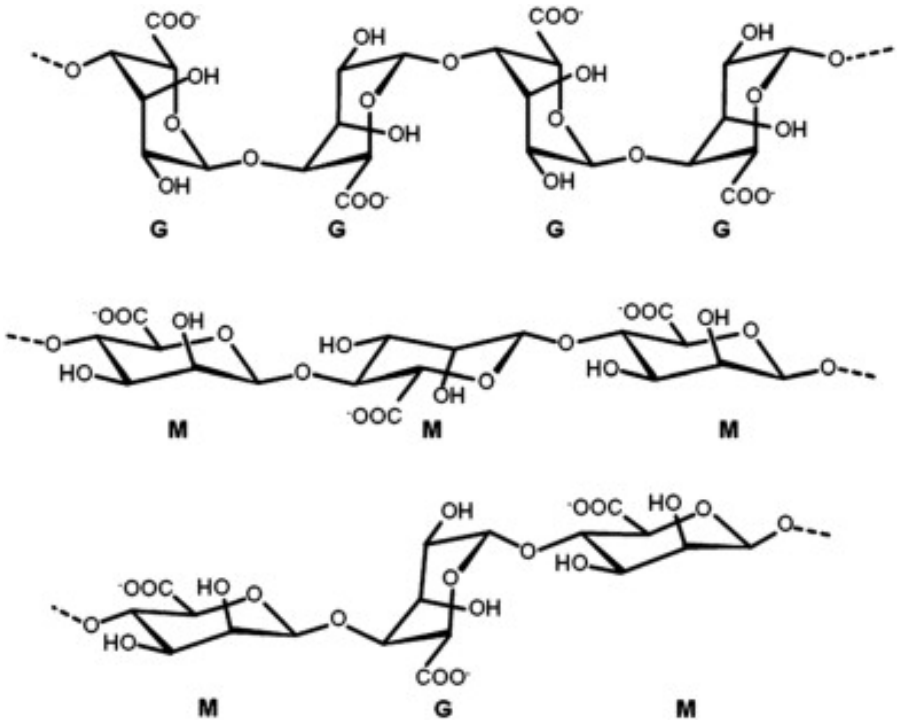


Figure 2. Possible molecular structures of alginate polymer chains. Adapted from *Paques J. et al, 2014* [54].

Alginate polymer chains can be functionalized due to the presence of two hydroxyl and one carboxyl groups (pK_a 3.6), which allows for various chemical reactions, like acetylation, phosphorylation, sulfation, oxidation, or coupling [55]. The decrease of the pH of the alginate solution leads to the protonation of the carboxylic acids of the polymer chains, at a pH close to the pK_a (pK_a 3.6), which increases the viscosity of the solution. Alginate can be used to form hydrogels by cross-linking, by interacting with divalent or trivalent cations like Ca^{2+} or Fe^{3+}, resulting in ionic gels [56]. This method consists of the exchange of sodium ions from G residues with the cations, forming a structure usually called "*egg-box*", with an adjacent chain (Figure 3) [57]. Cross-linking with cations results in a three-dimensional network with very high-water contents. As only the G residues participate in the interactions with the cations, alginate nanogels with a higher G content

and higher molecular weight, are usually more rigid and stable [58]. This technique does not allow to control the process, as it is a very quick reaction. To counteract this, there are some changes that can be made to improve the uniformity and slow the gelation process, such as the use of phosphate buffers, so that the phosphate groups compete with the interaction with the positive ions and slow the cross-linking [59]. Although this is a simple a low-cost method to obtain alginate nanogels, as they are physically linked, their stability is limited, as they can dissolve in the medium, when the calcium cations are released and exchanged with monovalent ions [54]. In drug delivery applications, the loss of structure of the nanogel provides them with a low retention capacity of the content. For nanogels composed only by alginate, an approach based on acidic gelation can also be used [58].

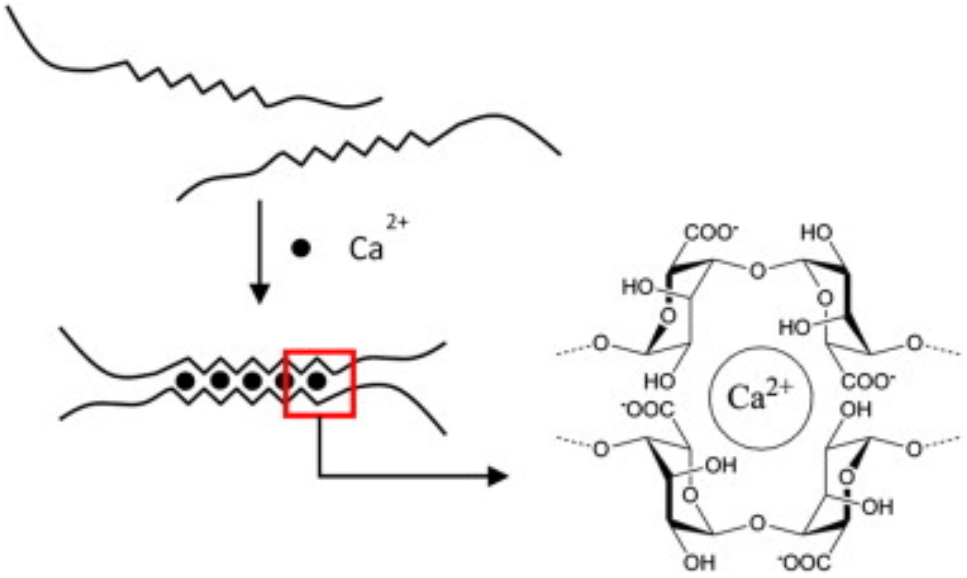


Figure 3. Scheme of cross-linking of alginate with the formation of "*egg-box*" structures with a divalent cation, Ca^{2+}. Adapted from *Paques J. et al, 2014* [54].

Another method to develop alginate nanogels is by chemical bonding between the polymer chains. This is possible because alginate contains functional groups, as mentioned before, hydroxyl and carboxyl groups, that are able to form covalent bonds and be modified. The resulting nanogels have better stability and increased mechanical properties [60]. However, the compounds used as catalysts are usually toxic and can interfere with the encapsulated cargo. Photo-crosslinking is a type of chemical cross-linking that uses radiation, such as ultraviolet radiation, to initiate the polymerization [61]. This method has also some challenges, such as the difficulty to control the kinetics of the polymerization reactions, the unreacted bonds that can react with the active compounds and the use of UV radiation [61].

Alginate nanogels carry some limitations, such as unstable structure, low mechanical strength, and are easily degraded, as they have affinity to various ions [60]. To overcome these limitations and optimize their activity, alginate can also be combined with other polymers or particles to form nanogels with different properties. For example, the addition of magnetic or plasmonic particles to alginate nanogels adds responsiveness to a magnetic field and to near infrared radiation, respectively, allowing its application as a theragnostic agent, through magnetic hyperthermia and imaging, and photothermia [62], [63], [64].

1.3.3. Alginate-chitosan nanogels

Alginate can also be combined with other polymers, like cationic polymers, to form stable nanogels, through electrostatic interactions. Chitosan-alginate nanogels are the most frequent combination, as they are both of natural and abundant sources, versatile, highly compatible, but mostly because they can overcome each other limitations, like solubility and stability issues [65], [66], [67]. To be more specific, this combination allows for the decreasing of the porosity of alginate leading to a better retention of the entrapped molecules [68]. On the other hand, the complexation with alginate provides chitosan with a better mechanical stability [68], [69]. The formation of a polyelectrolyte complex between alginate and chitosan is possible due to the formation of electrostatic interactions between the amino groups of chitosan's backbone and the carboxylic acids of alginate [70]. This combination can be achieved through ionotropic gelation, following a one-step or two-step procedure. The first, being the addition of one of the polymer solutions to the other, dropwise, to allow the formation of interactions [71]. The two-step method consists of firstly preparing an alginate nanogel by ionic cross linking with a bivalent cation, for example, and then adding it to the chitosan solution. To improve the particles polydispersity, size homogeneity and stability, this method can be combined with polyelectrolyte complexion [72]. In this case, adding the chitosan solution, previously linked to a counter ion, like TPP, to an alginate solution, results in chitosan core particles, with better mechanical stability, and lower polydispersity [73]. *Segale et al.* [74] addressed the swelling behavior of the polyelectrolyte complex, comparing it with the alginate nanogel, at different pH levels. When exposed to acidic medium (pH 1.0), the chitosan-alginate nanogels did not show significant differences in the swelling, comparing with alginate nanogels. At this pH, the carboxyl groups of alginate are protonated and the polymer becomes insoluble, blocking the fluid absorption. In the polyelectrolyte complexes, even though the chitosan is positively charged in this condition, the swelling is limited by the alginate structure. On the other hand, at more neutral pH, a higher swelling is observed in alginate nanogels, comparing with chitosan-

alginate nanogels. This can be explained by an exchange of the ions that are keeping the "*egg box*" structure, with the ions present in the buffer medium, causing a loosening of the structure and an increase of the swelling, followed by a disintegration of the network (represented by a decrease of the weight). In contrast, chitosan-alginate nanogels display a lower swelling, and no erosion, probably due to a higher mechanical stability provided by the interactions between the two polymers. Those results suggest that chitosan-alginate nanogels are more stable and can provide a more controlled swelling and consequently, a more controlled release of the cargo, being more advantageous for drug delivery than alginate nanogels.

This polyelectrolyte complexes are being extensively studied [75], [76], for the application in drug delivery, wastewater treatments, agriculture, theranostics, because of their unique and advantageous properties [77], [78], [79], [80].

1.3.3.1. Drug delivery applications

These nanosystems have been used in drug delivery applications, as carriers, to increase the drugs' half-life in the blood, enhance the availability of hydrophobic molecules and target malignant cells. As a result of all its properties, chitosan-alginate nanogels, have been shown to be suitable for delivering molecules, throughout different administration routes, such as oral, ocular, nasal or intravenous [65], [81].

The tumor environment presents some different physicochemical characteristics when comparing to healthy tissues. A slightly acidic pH, around 6–6.5, is usually reported in extracellular tumor environments and therefore, carriers that are chemically stable at pH 7.4 and that suffer alterations at lower pH values, are useful in the delivery to tumors [82]. Glutathione (GSH) is a protein involved in several processes, such as cell proliferation, and that is typically in higher concentrations in cells with high proliferation rates [83]. In physiological conditions, the extracellular concentration of GSH is around 20 μM, comparing with the 80 μM reported in extracellular tumor environments [82]. Besides, GSH's concentrations inside the tumor cells and cells with high proliferation rates, such as fibroblasts, is higher and can reach 10 mM [82]. Thus, using a GSH-sensitive nanomaterial can be an attractive strategy for efficient delivery to tumor cells.

Chitosan-alginate nanogel particles have been reported in previous studies to be excellent carriers for tumor applications, considering its size, surface characteristics, loading capacity, stability, and controlled release abilities. Due to its nanoscale size, they can easily penetrate the cell membrane and passively accumulate in tumor tissues because of the EPR effect. Moreover, chitosan-alginate nanogels can swell in a stimuli-

responsive way and release its content through controlled diffusion from the polymer network.

Chitosan's free amino groups provide it with a pH-responsive behavior which means that in more acid environments, the amines are protonated, causing the gel to swell due to repulsion between the polymer chains, and leading to the release of the encapsulated content. On the other hand, at higher pH levels, as the protons are removed from the polymer, the nanogel particles suffer a decrease in size, due to a reduction of hydrophilicity. Alginate shows an opposite behavior as its negative charge is neutralized at lower pH levels [65]. This contrasting behavior leads to a decrease on the swelling of the polymer network and to the prevention of structural degradation, comparing to the one-polymer nanogel, due to the interaction between chitosan and alginate. This behavior is a key factor for a more controlled release of the drugs in tumors, as the tumor microenvironment is slightly more acidic (around 6–6.5) than healthy tissues. Furthermore, chitosan-alginate nanogels, with a chitosan core, prevent the initial burst release observed in single polymer nanogels [84]. This initial burst release is unwanted as it can lead to toxicity, drug loss and, therefore, decrease the extent of the therapeutic effect [85].

In addition, nanogels with thiol groups can form disulfide bonds and consequently are sensitive to the redox environment, being reduced in high concentrations of GSH. Disulfide bonds present between the thiol groups of the nanogel can be reduced and cleaved, leading to an alteration of the structure of the nanogel and promoting the release of the encapsulated cargo [86], [87]. On the other hand, in environments with low concentrations of GSH, such as the healthy extracellular tissues, the nanogel can maintain its structure, preventing the release of the active agents and decreasing their toxic effects. Therefore, the modification of chitosan-alginate nanogels with thiol groups, like cysteines and cysteamines, may amplify the physicochemical features of the nanogels, conferring GSH-responsivity, which is useful for intratumor delivery.

1.4. Nanoparticles

Particles of a nanometer scale, usually between 1–1000 nm, are referred to as nanoparticles, and often have different properties from the bulk material [88], [89]. Two main approaches are used to obtain nanoparticles with different charges, shapes and sizes, top-down and bottom-up. The first one, consists on reducing the size of a bulk material by different techniques, usually physical (laser ablation, inert gas condensation…), to reach the nanoscale particles [90]. The other approach relies on the

assembly of molecules and atoms, to create nanoparticles with the desired shape and size [91].

Nanoparticles can be classified based on their composition, as organic (proteins, lipids, carbon-based) or inorganic (metallic) [92]. Another way to separate them in classes, is by their dimension, 0D, if all their dimensions are within the nanoscale range, as quantum dots; 1D, when one of their dimensions is bigger than 100 nm, like nanotubes and nanorods; 2D, like nanofilms, or 3D [92].

1.4.1. Plasmonic nanoparticles

Surface plasmon resonance is a phenomenon associated with the displacement of free electrons localized at the surface of a noble metal (gold, silver…) at the nanometer scale. When under specific wavelength radiation (comparable to the size of the particle), the oscillation of the electron cloud of the particle reaches the maximum amplitude, enhancing the electromagnetic field in that area, and induces the absorption and scattering, occurring the surface plasmon resonance (SPR) (Figure 4)[93], [94]. This optical property results in an absorption maximum localized in the visible or near-infrared (NIR) regions that is specific of the material, and depends on the size, shape and aggregation state of the particles, as well as the refractive index on the surface [95], and is the key factor for its use in sensing and other biomedical applications [96], [97], [98]. The strong absorption in the NIR region (750–1350 nm), also known as the biological window, is advantageous as it allows the use of NIR radiation for therapies. The NIR radiation provides better tissue penetration, and little absorption from the cells, avoiding tissue damages, when comparing with visible and ultraviolet radiation [99].

The energy absorbed when the electrons are excited decays through non-radiative relaxation of the electrons, through phonon-phonon relaxation, resulting in conversion of the energy into heat, leading up to the increase of the surrounding temperature [100], [101]. This light conversion capacity is commonly used for photothermal therapy in cancer, to induce cell death by local hyperthermia [102], [103]. The use of plasmonic nanoparticles for photothermal therapy allows for a more localized therapy and therefore decreases the damage caused to healthy tissues during irradiation in traditional phototherapy [104]. Studies revealed that cell death caused by plasmonic nanoparticles' photothermal conversion, is carried through the destabilization of the membrane, leading to degradation of the actin network [105]. Photothermal therapy has many advantages as it is a non-invasive strategy, does not cause drug resistance and is controlled in time and space, being also used in combination with other therapies to achieve a synergistic

effect [106]. However, it has some challenges, such as the low efficacy to treat more internal tumors, due to the light penetration, and it cannot eliminate tumors alone.

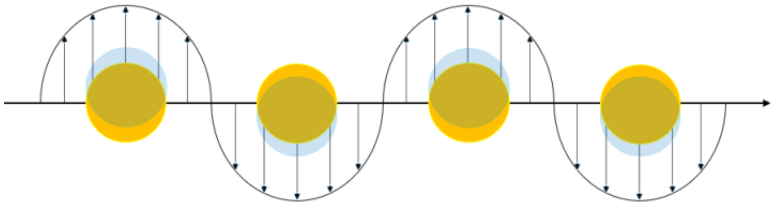


Figure 4. Scheme of the electron charge cloud oscillation of a sphere under an electric field. Adapted from *E. Hutter et al, 2004* [107].

Gold nanorods (AuNRs), have an anisotropic shape which allows for two directions of oscillation of the electrons (transversal and longitudinal), resulting in two absorption bands. The oscillation in the transversal axis of the rod induces an absorption band in the visible region (≈ 510 nm), the transversal surface plasmon resonance (TSPR), while in the longitudinal axis, induces an absorption band in the visible or NIR, the longitudinal surface plasmon resonance (LSPR). This last one is very sensitive to variations in the aspect ratio (length/width) of the nanoparticle, being the shift linearly proportional to it. AuNRs with higher aspect ratios are more sensitive to changes, which is reflected in shifts on the LSPR absorption band [98].

The most well described strategy for AuNRs synthesis is a seed mediated method, that involves the development of seeds through the reduction of $HAuCl_4$ and their growth into rod shaped particles, in a controlled and two-step way [108]. This procedure allows for great control of the size and polydispersity of the particles. A method that has been gaining attention recently is the one-pot synthesis, or seedless method, that does not require the previous preparation of gold seeds. In this case, the addition of a strong reducing agent allows for the reduction of the gold precursor into smaller particles, that will then grow into AuNRs [109]. However, this method did not allow for a control of the shape and size of the particles, neither a control of the LSPR position. Recently, reports such as *Roach et al* [110], have been shown to improve the yield and the quality of the particles by using binary surfactants. In their procedure, sodium oleate is added besides cetyltrimethylammonium bromide (CTAB), to improve the monodispersity and to provide better control of the shape of the particles. Besides controlling the shape of the particles, CTAB also forms a layer at the surface, giving them a positive charge, which will cause repulsion between the particles, and therefore stability against aggregation. Silver ions are essential to regulate the initial growth and the anisotropy, due to their adsorption in the faces of the particles, controlling its growth. A mild reducing agent, usually ascorbic

acid, is used to primarily reduce the gold, in specific pH conditions. Lastly, sodium borohydride, a strong reducing agent, initiates the nucleation, and reduces the gold to the final state, Au^0. The aspect ratio and the LSPR can be controlled by adjusting the concentrations of the reagents, temperature, and pH, so that the final particles possess the desired characteristics [111].

1.4.1.1. Mesoporous silica coating

AuNRs have several advantages and properties that can be used and applied for multiple purposes. However, despite all the advantages, they still have some issues related to their toxicity due to the CTAB capping and low colloidal stability in physiological conditions and under irradiation [112].

Silica's negative charged groups have high affinity for AuNRs' CTAB capping, as it is positively charged, allowing for the deposition of a layer at the surface of the nanoparticles. The addition of the silica layer usually leads to a shift of the LSPR band of the AuNRs, as it changes the refractive index at the surface [113]. Adjustments in the synthesis' parameters allows the control of the surface characteristics of the silica layer, such as its thickness, and the volume of the pores [114].

The addition of a mesoporous silica shell to the AuNRs surface improves their thermal and colloidal stability, preventing their aggregation and deformation in aqueous solutions [115], [116]. The addition of the mesoporous silica layer usually follows the Stöber method. This method involves the hydrolysis of a silica precursor, like tetraethyl orthosilicate (TEOS, ester of orthosilicic acid) (Figure 5), in an alcohol solution, with ammonia as a catalyst, at constant and high temperature [117]. A more recent procedure has been described by *Gorelikov and Matsuura* [118], for a more simple and direct coating of nanoparticles. This last method, uses CTAB as a template for the silica precursor's polymerization, at the surface of the AuNR. The resulting particles present multiple disordered pores, and its thickness can be increased by adding more TEOS to the growth solution.

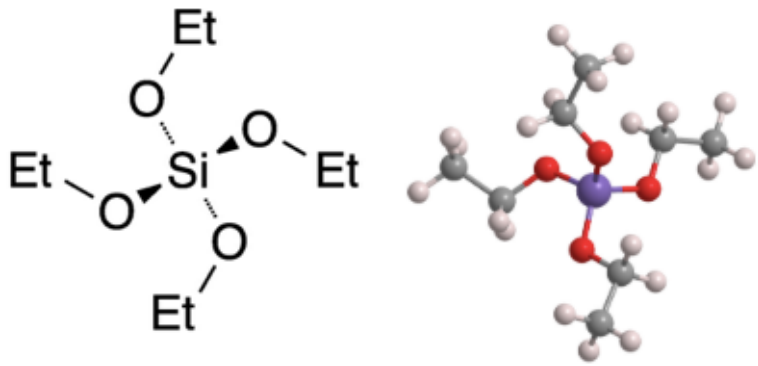


Figure 5. Molecular structure of TEOS.

Another advantage is that mesoporous silica allows for easier surface modification, and for the encapsulation of small therapeutic agents, such as genes or drugs, increasing the encapsulation ability of the particles, making it useful for drug delivery applications [106], [119], [120]. Mesoporous silica nanoparticles have been extensively studied for their application as delivery agents. Their tunable size and thickness, controllable pore volume, and easy surface modification are appealing characteristics for the development of delivery systems [121]. The high number of disordered pores increases the surface area, allowing for the entrapment of a high number of compounds [122].

However, despite all the advantages, mesoporous silica nanoparticles can lead to premature release of molecules physically entrapped, before reaching the target site [123]. This problem can be avoided by functionalizing the surface with molecules that can act as gatekeepers. There are different agents that can be used as gatekeepers, such as polymers and proteins. Depending on the gatekeeper, the release can happen after a stimulus that can be endogenous, such as pH, or exogenous, such as laser irradiation or magnetic field [124], [125], [126], [127]. Polymers can be used as gatekeepers, by interacting covalently or non-covalently with the mesoporous silica. The polymer chains cover the pores and block the release of its content. A stimulus like pH or temperature can induce a change in the polymers conformation, which will cause the unblocking of the pores and consequently, the content will be released [128]. However, this approach apports some limitations, as for it to be efficient, it is important that the polymer chains placement overlaps with the pores. In addition, the size of the polymer is also relevant, as small polymers may not be able to cover the pores and big polymers may not let the content be released properly [123].

1.4.1.2. Liposomes coating

Liposomes are generally spherical, closed lipid bilayers composed mostly of natural or synthetic phospholipids (Figure 6) [129]. Phospholipids comprise a polar hydrophilic

head and two hydrophobic chains and have the predisposition to form membranes by self-assembly in aqueous solutions [130].

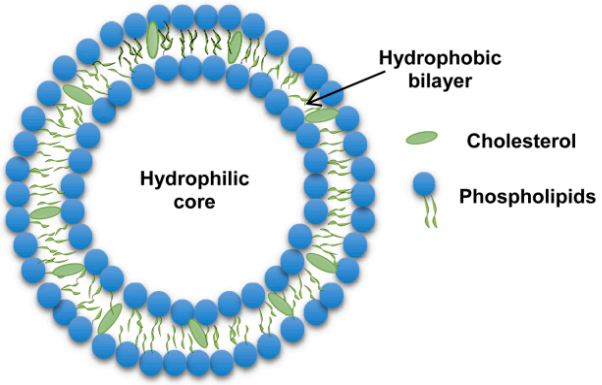


Figure 6. Schematic image of liposome structure with cholesterol. Adapted from *Nsairat et al*, 2022[129].

This unique structure confers the capacity to interact and encapsulate both hydrophilic and hydrophobic molecules, on the aqueous interior or by adsorption at the surface, and on the interior of the hydrophobic membrane, respectively [131]. Liposomes are versatile particles, as their composition can be varied by altering the phospholipid composition, and consequently, changing their fluidity, phase transition temperature and surface charge. The structure of the phospholipids composing the membrane, the charge of the polar head, the degree of unsaturation and length of the fatty acid chains, will determine the membrane's characteristics [132]. Furthermore, they are biocompatible, non-toxic and of simple preparation, as they can form through self-assembly. They can also be modified by adding sterols, proteins and polymers to the membrane [132], [133], [134]. The most common modification is the addition of cholesterol, a hydrophobic molecule that interacts with the phospholipids and increases the stability, reducing the fluidity and permeability [134], [135].

Dipalmitoylphosphatidylcholine (DPPC) is a saturated zwitterionic phospholipid and is composed of two palmitic acids linked to a phosphate group and a choline (Figure 7). As this phospholipid contains saturated chains, it can pack and form layers with a higher phase transition temperature (≈ 41ºC) than unsaturated phospholipids. At temperatures above 41ºC, the layer undergoes phase transition and becomes more fluid and permeable.

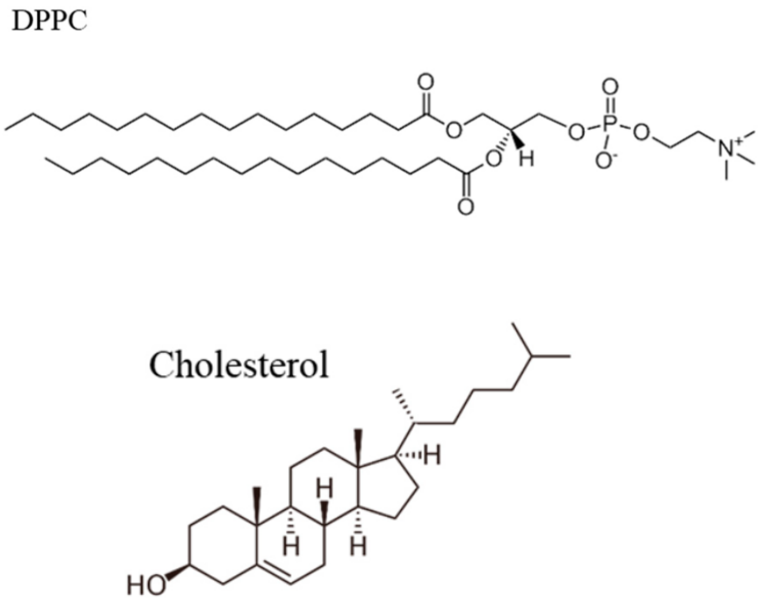


Figure 7. Molecular structures of DPPC and cholesterol. Adapted from *Victoria M. Katata et al, 2022* [136]

Liposomes are widely used as cell membrane models, to study the interaction of the cell membrane with drugs, as they can simulate the lipid composition of natural cell membranes both in physiological and pathological circumstances [137], [138].

These lipid bilayers have also been used as delivery agents, as they can encapsulate lipophilic and hydrophilic compounds [139]. Their biocompatibility, flexibility and response to temperature make them very useful tools for the transport and delivery of active agents, such as cosmetics, therapeutics and vitamins [140]. Furthermore, they can also be used to encapsulate nanoparticles. This combination fills some gaps on both liposomes and nanoparticles. The encapsulation of the nanoparticles in liposomes prevents the fusion between liposomes, increasing their stability. In addition to that, nanoparticles can maintain their characteristics, such as magnetism and fluorescence. On the other hand, liposomes increase the nanoparticles biocompatibility, while offering an easier way to enter the cells [141]. The incorporation of nanoparticles in liposomes depends on the physicochemical characteristics of the particles, but it is usually a simple process. They can be passively loaded during the assembly of the phospholipids, or after the formation of the liposomes [142]. In the latter case, they are added to the surface, through non-covalent interactions, for example. The most common method of preparation is the thin-film hydration, that can be used for the encapsulation of both hydrophilic and non-hydrophilic cargo [142], [143]. This technique requires the drying of a solution of the lipids in a volatile solvent, to obtain a thin film on the wall of the recipient. After that, the film is hydrated with an aqueous solution containing the hydrophilic

nanoparticles. In the case of hydrophobic nanoparticles, they can be added to the lipid solution. The hydration of the lipid film will allow for the formation of the liposomes around the particles.

As for drug delivery applications, liposome-coated nanoparticles are very useful systems and have been widely explored, due to their advantageous characteristics. As already mentioned, mesoporous silica particles have the ability to encapsulate a great amount of cargo, however, they do not usually display a controlled release. Liposomes can be used as carriers of these particles, acting as a gatekeeper [121], [123]. This gatekeeping action prevents the unwanted premature release of the content, providing a controlled liberation when the particles reach the target site [144]. Besides acting as a barrier to the release, liposomes are also temperature-sensitive, which adds a stimuli response to the release [123]. When below the phase transition temperature, the liposome is in a gel state, being less permeable. On the other hand, as the temperature surpasses the phase transition temperature, the lipids undergo a phase transition and the liposome becomes more fluid and permeable, allowing the release of the content inside [144].

1.5. Plasmonic nanolipogels

Plasmonic nanogels consist of the combination of the characteristics of nanogels with the characteristics of plasmonic nanoparticles. This novel material possesses new properties, that can be tuned, depending on the nanoparticle's physicochemical characteristics and the nanogel's composition, and that would not be possible to achieve with the original materials individually [145]. The materials can interact non-covalently, by hydrogen bonds or electrostatic interactions, or they can form covalent bonds, which can result in the alteration of the swelling ability of the nanogels, as well as its porosity and structure [146].

The incorporation of plasmonic nanoparticles, such as AuNRs, in the nanogels' network, confers them with bioimaging capacity, in addition to photothermal ability, making them interesting materials for theranostics, phototherapy and sensing [147]. In addition to that, the incorporation of a silica layer increases the encapsulation capacity of the nanogel [106], [148], adding a new encapsulation site and the possibility of a sequential release. The use of liposomes as gatekeepers allows to prevent the early release of the content inside the pores of the silica [123]. Besides, the lipid layer introduces a new stimuli-responsivity to the system, as the liposomes become more fluid when the temperature is higher than the lipid's phase transition temperature, allowing the release of the cargo [75].

Studies reported that the combination of plasmonic nanoparticles with high photothermal conversion efficiency and temperature-responsive nanogels can trigger the swelling of the nanogels' matrix when the temperature arises the lower critical solution temperature (LCST), and consequently the release of the encapsulated cargo, in drug delivery applications [149], [150], [151], [152].

1.6. Mitoxantrone

Mitoxantrone (1,4-dihydroxy-5,8-bis[2-(2-hydroxyethylamino)ethylamino]antracene-9,10-dione, also known by its commercial name *Novantrone*, is an anthracenedione, a polycyclic aromatic molecule, with antitumor effects. This molecule contains a chromophore composed of three planar rings, and two side chains with ionizable amino groups (pK_a 8.3 – 8.6) (Figure 8) [153]. The absorption spectrum of mitoxantrone presents absorption maxima at 610 nm and 660 nm. Mitoxantrone's antitumor effect is related to the capacity of inhibiting deoxyribonucleic acid's (DNA) replication and ribonucleic acid (RNA) synthesis, by intercalation in the DNA, within its planar rings, supported by electrostatic interactions between its amino groups and the DNA's phosphate groups [154], [155]. Besides that, it also inhibits the enzyme responsible for repairing damaged DNA, topoisomerase II, causing an increase of damaged genetic material in the cell.

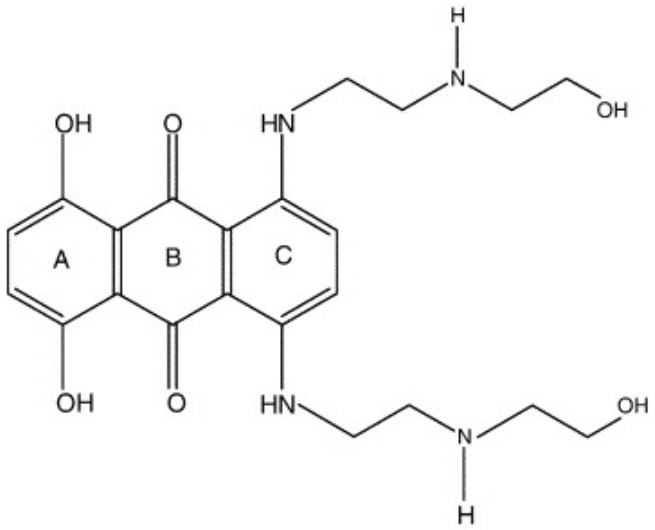


Figure 8. Structure of mitoxantrone.

Mitoxantrone (MTX) was approved for clinical use by Food and Drug Administration (FDA), in treatments of adult acute myeloid leukemia (1987), of symptomatic hormone-refractory prostate cancer (1996), of worsening relapsing-remitting multiple sclerosis, secondary progressive multiple sclerosis (2000), breast cancer as a second line therapy

and others [156], [157], [158]. *In vivo* studies revealed good efficacy against advanced breast cancer, non-Hodgkin's lymphoma, advanced breast cancer, and advanced prostate cancer [157], [159], [160], [161]. Moreover, it was also employed as a palliative treatment in patients with advanced ovarian carcinoma, stabilizing the progression of the disease [162]. MTX's administration combined with other chemotherapeutic agents has been assessed. Combination with corticosteroids as hydrocortisone presented significant pain reduction, comparing with combination with prednisone [159]. The combination with a glycolysis inhibitor, 3-BP, has shown, *in vitro* and *in vivo* to decrease drug resistance and to slow tumor growth [163].

MTX has been shown to be a more tolerable chemotherapeutic agent, having less aggressive side effects, like nausea, than other drugs, as doxorubicin, being used as an alternative [162]. MTX was tested in patients with breast cancer and prostate cancer, and its toxicity and efficiency were compared to doxorubicin, showing slightly less activity, but significantly less cardiotoxicity [164]. The lower cardiotoxicity of MTX can be related to the type of toxicity induced, as MTX creates energy imbalance in the cells, comparing with doxorubicin that interferes with the redox cycle [165].

1.7. 2-Deoxy-d-glucose

Tumors usually have high rates of proliferation with hypoxic areas, which exhibit slower growth and have low concentrations of oxygen [166]. Besides, cancer cells can also present mutations in the mitochondria genetic material, causing a reduction of the oxidative phosphorylation [167]. Thereby, anaerobic glycolysis is a mechanism for energy production that cancer cells depend on to achieve rapid cell growth and proliferation, as it is the only pathway that allows for the production of adenosine triphosphate (ATP) in the lack of oxygen. Moreover, the energy production is also used to produce lactate and acidify the environment, which, consequently, will protonate ionizable molecules, such as basic chemotherapeutic drugs. The protonated drugs are less likely to enter the cells and therefore its treatment efficacy is reduced [168].

In glycolysis, glucose is phosphorylated to glucose-6-phosphate, by a hexokinase, and then it can enter the pentose phosphate pathway (to produce the building blocks for nucleic acid production), by becoming substrate of glucose-6-phosphate dehydrogenase or it can continue the glycolysis pathway and form fructose-6-phosphate. At the end of glycolysis, one glucose molecule originates two pyruvate molecules and two ATP molecules. The pyruvate molecules can follow two directions depending on the presence or absence of oxygen, the citric acid cycle at the mitochondria, or it is converted in lactate, respectively [169].

2-Deoxy-D-arabino-hexose, or 2-deoxy-D-glucose (2DG), $C_6H_{12}O_5$, is a glucose analogue. This compound has a very similar molecular structure to glucose, a hexose, differing only on the carbon 2, where glucose has a hydroxyl and 2DG has a hydrogen (Figure 9) [170].

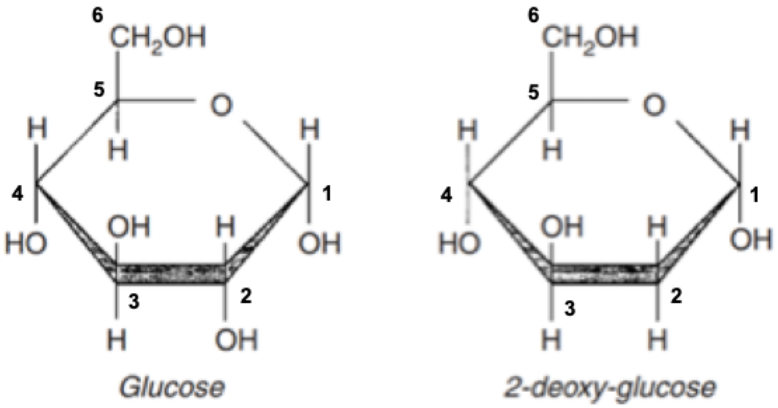


Figure 9. Molecular structure of glucose and 2DG. Adapted from *Jyostna Bere et al, 2021* [170].

As 2DG is very similar to glucose, it can pass through the membrane by the same means as glucose, competing with it, and entering by facilitated diffusion, by transporters. After that, 2DG enters the glycolysis pathway, being phosphorylated to 2-deoxy-D-glucose-6-phosphate (2DG-6-P). 2DG-6-P, due to the lack of the hydroxyl group on the carbon 2, cannot be substrate of the next enzyme of the pathway, the isomerase, and consequently, accumulates and stops the glycolysis. The increase of the concentration of 2DG-6P causes the inhibition of the hexokinase who phosphorylates glucose/2DG to start glycolysis. The arrest of the glycolysis pathway, prevents the production of energy (ATP), leading to energy stress (Figure 10).

On the other hand, 2DG is also very similar to mannose, and can be converted to 2-DG-GDP and interfere with the N-glycosylation of proteins, which will affect the correct folding and synthesis of glycoproteins, leading to stress in the endoplasmic reticulum (Figure 10) [171].

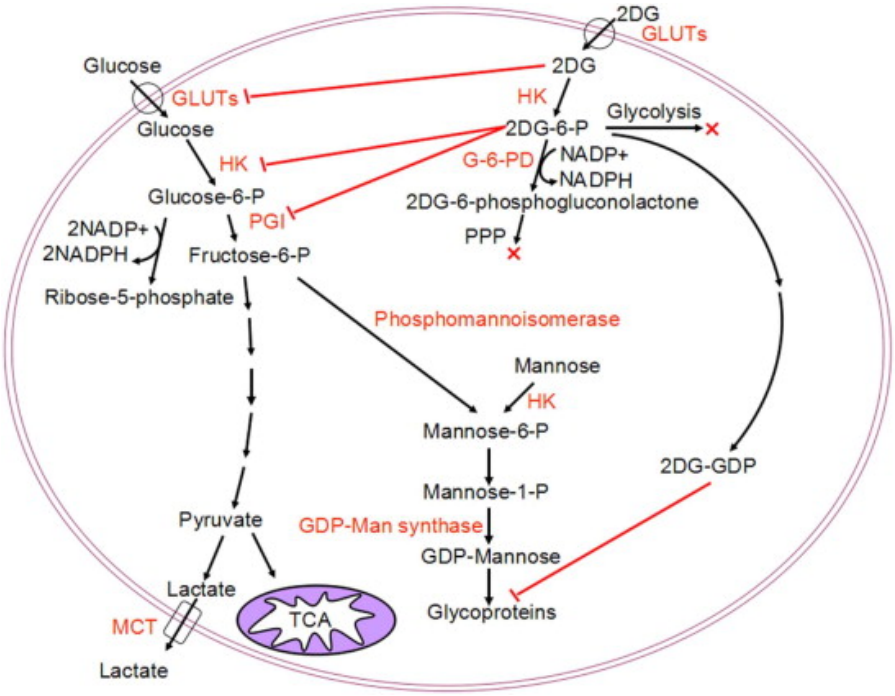


Figure 10. Effects of 2DG uptake on the cell: glycolysis pathway; synthesis of glycoproteins. Adapted from *Zhang D. et al, 2014* [167].

2DG is still not FDA approved, however it has been shown to be efficient against breast, pancreatic and ovarian cancer cells, but also in patients with castrate-resistant prostate cancer [172], [173], [174], [175], [176]. Besides its application in tumors, 2DG has also been tested as treatment for other diseases, as covid-19 [177]. *In vitro* studies, in breast cancer cell lines (human, canine and rat), showed that the reduction of glycolysis output resulted in inhibition of invasion and migration of the tumor cells [178].

The administration of 2DG alone has proven to be insufficiently efficient in causing cell death. So, combination therapies have been explored, using 2DG as an agent to weaken the cells, so that the therapy can have better results, leading to higher tumor growth reduction. The combination of 2DG with mitochondrial enzyme's inhibitors improved results when compared with single therapy [178]. Combining photothermal therapy and a chemotherapeutic agent, doxorubicin, with 2DG, allowed to enhance the photothermal effect as well as the drug bioavailability, by inducing starvation, inhibiting the production of energy, consequently inhibiting the production of heat shock proteins and reducing the cells thermoresistance [179].

1.8. Combination therapy

Monotherapy is the most used approach for the traditional chemotherapy of several cancers. However, it has several limitations, as it can lead to drug resistance and to

damage in proliferating healthy cells, such as fibroblasts, due to low tumor selectivity [180].

The combination of different drugs with different mechanisms can produce a synergistic effect, potentially allowing for reduced dosages and consequently decrease the toxicity to healthy tissues and increase the treatment's efficacy [181], [182]. *Li et al* [183] reported that the co-delivery of doxorubicin and methotrexate, using nanomicelles improved antitumor efficacy.

On the other hand, the combination of different therapies, such as chemotherapy, immunotherapy, phototherapy or starvation therapy can also have some advantages and lead to a synergistic effect [184] . Phototherapy can cause cell death through local hyperthermia, however it cannot alone eradicate tumors. On the other hand, immunotherapy is only efficient in small and primary tumors, as it has no effect in bigger and advanced malignancies. Starvation therapy relies on the obstruction of glycolysis to delay the tumor's proliferation but cannot eliminate it. The combination of different therapies results in an addictive and/or synergistic effect, achieving better results in tumor elimination [185]. *Li et al* [186], developed a delivery system to transport and deliver a chemotherapeutic agent, doxorubicin and a photosensitizer, indocyanine green, and achieved promising results at reducing the tumor size.

Hereby, this work focused on the development, optimization and characterization of a plasmonic nanogel for the application in combined therapy of cancer, as a carrier of two active agents and a photothermal agent (Figure 11). The encapsulation of MTX and 2-DG in the nanogel network and in the plasmonic nanoparticles, respectively, aimed to achieve a sequential and stimuli-controlled release, as well as decrease their cytotoxicity in healthy tissues. The designed system will be tested to verify the stimuli-responsive release, and its cytotoxicity will be assessed in fibroblasts and breast cancer cell lines, to evaluate its potential as an intratumoral delivery agent.

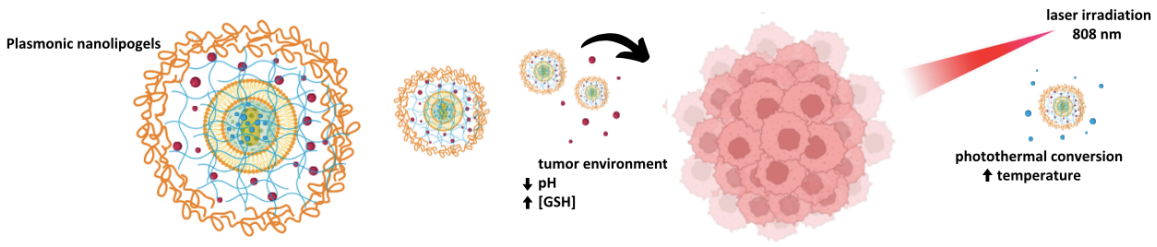


Figure 11. Scheme of the proposed nanosystem.

2. Experimental Section

2.1. Development of the plasmonic nanolipogels

2.1.1. Preparation of plasmonic particles

2.1.1.1. Synthesis of AuNRs

AuNRs were prepared following a seedless method, adapted from *Roach et al* [110]. The apparatus of the synthesis is represented in figure 12. First, in a flask, at 30 ºC with stirring, CTAB (200 mM) and sodium oleate (200 mM) stock solutions in Milli-Q water were added, at final concentrations of 38 mM and 12.5 mM, respectively. The volume was topped up to 5 mL with Milli-Q water. Then, at 5 minutes intervals, 5 mL of $HAuCl_4$ (1 mM), 240 µL of $AgNO_3$ (4 mM), 50 µL of HCl 37%, 75 µL of ascorbic acid (85 mM), were added. To start the reaction, 7.5 µL of freshly prepared $NaBH_4$ in Milli-Q water (10 mM) was injected in the reaction, and the stirring was rapidly stopped. The reaction was kept at 30 ºC for 4 hours. The prepared AuNRs were washed twice with Milli-Q water and centrifuged at 9000 g for 20 minutes.

Stock solutions mentioned above were all prepared by dissolving in Milli-Q water.

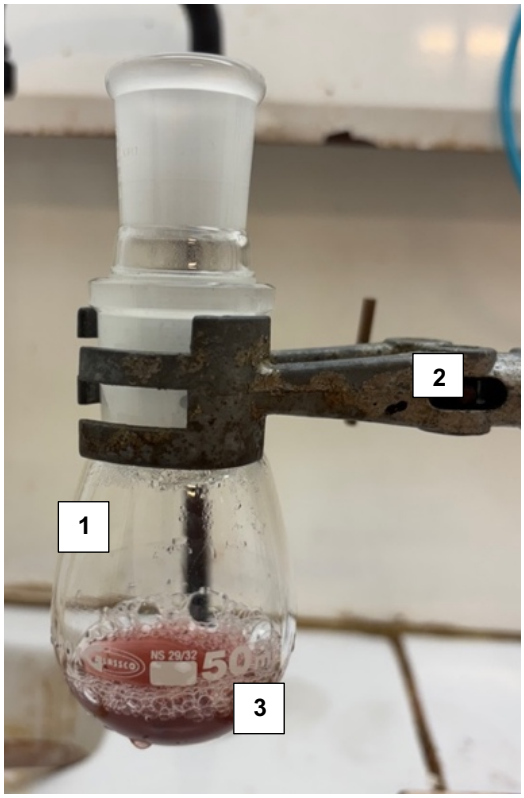


Figure 12. Apparatus for AuNRs synthesis. (1) round bottom flask, (2) utility clamp, (3) AuNRs solution.

2.1.1.2. AuNRs' coating with mesoporous silica

The AuNRs were then coated with mesoporous silica, following a reported method, with some adaptations [118]. The AuNRs were resuspended in 20 mL of CTAB 800 μM in Milli-Q water. To adjust the pH of the reaction, 200 μL of NaOH 0.1 M were added under stirring, at 26 – 30 ºC. Finally, 60 μL of TEOS 20% in methanol, were injected three times in the solution, at 30 minutes intervals. The reaction was kept at 26 – 30 ºC, for 3 days under gentle stirring. To remove the CTAB remaining inside the silica pores, AuNRs@Si were centrifuged 20 min, at 9000 g, and resuspended in 10 mL of ethanol. Under stirring, 100 μL of 1% (v/v) HCl was added. After 1 day under stirring, at 60 ºC, the prepared silica-coated gold nanorods (AuNRs@Si) were washed twice with ethanol and centrifuged for 20 min at 9000 g and stored in 2 mL of ethanol.

2.1.1.3. Addition of lipid bilayer

The coverage of the nanoparticles' surface with a lipid bilayer was optimized by assessing different DPPC:Cholesterol concentrations (0.1 mM, 0.2 mM, 0.3 mM and 0.4 mM), at a 7:3 ratio. Stock solutions of 10 mM DPPC and 10 mM cholesterol were prepared in chloroform. The lipid solutions were evaporated with a stream of ultrapure nitrogen gas, forming a film. Then, 0.1 mg of AuNRs@Si in ethanol were added to the lipid film, sonicated for 20 minutes and evaporated with a stream of ultrapure nitrogen gas. The resulting film was resuspended in 1 mL of phosphate buffer 10 mM, pH 7.4.

2.1.1.4. Characterization of the plasmonic nanoparticles

The nanoparticles were characterized through different techniques to assess their surface charge, size, shape and to confirm modifications, like the addition of the mesoporous silica layer and the lipid bilayer.

UV-Vis-NIR spectrophotometry characterization of the nanoparticles was carried using a Shimadzu UV-3600 Plus UV-Vis-NIR spectrophotometer (Shimadzu Corporation, Kyoto, Japan), with quartz cuvettes with an optical path of 1 cm and 1 mm. All the absorption spectra of AuNRs, AuNRs@Si and lipid and silica-coated gold nanorods (AuNRs@Si@Lip) were obtained between 300 and 1200 nm, at room temperature and using Milli-Q water as baseline. AuNRs and AuNRs@Si spectra were obtained with a dilution of 1:10, and AuNRs@Si@Lip spectra were obtained without any dilution.

The hydrodynamic size and zeta potential of the nanoparticles were obtained in a Dynamic Light Scattering (DLS) equipment Litesizer™ 500 from Anton Paar (Anton Paar GmbH, Graz, Austria), using a semiconductor laser diode of 40 mW and $\lambda = 658$ nm, and controlled temperature of 25 ºC. The measurements were carried in Milli-Q water, with a dilution of 1:10 for AuNRs@Si@Lip and of 1:100 for AuNRs and AuNRs@Si. Zeta

potential measurements were obtained in triplicates with 100 runs, using an Omega cuvette Mat.No. 225288. To assess the hydrodynamic size, a polystyrene disposable cuvette was used, and the samples were filtered with a 0.45 µm cut-off syringe filter. The measurements were obtained in triplicate, with a maximum of 60 runs of 10 seconds each. Hydrodynamic size of AuNRs was obtained setting gold as the material (refractive index of 0.648 and absorption coefficient of 3.2) and water as the solvent. Regarding AuNRs@Si measurements, they were obtained setting Silica (amorphous) as the material (refractive index of 1.46 and absorption coefficient of 0.1), water as the solvent and a measurement angle of 175º (backscattering geometry). As for AuNRs@Si@Lip, the material was set as phospholipids (refractive index of 1.45 and absorption coefficient of 0.001) and the solvent as water.

Transmission Electron Microscopy (TEM) images of the nanoparticles (AuNRs and AuNRs@Si) were captured with a high contrast JEOL JEM-1010, operating at 100kV (CACTI, Vigo, Spain).

2.1.2. Preparation of the plasmonic nanogels

2.1.2.1. Modification of chitosan

To prepare the nanogel, chitosan was previously modified with cysteine. The chemical modification of chitosan with L-cysteine, was based on a reported method with some adjustments [187]. First, 175 mg of L-cysteine was slowly added to a 0.238 M HCl solution, followed by the addition of 222.5 mg of EDC (1-Ethyl-3-(3-dimethylaminopropyl)carbodiimide). To prepare the chitosan solution, 125 mg of chitosan was dissolved in 7.5 mL of 2% acetic acid. Finally, the L-cysteine solution was added to the chitosan solution, and kept under stirring, for 5 hours. The modified polymer was purified by dialysis with a 10 kDa cut off $Slide-A-Lyzer^{TM}$ MINI Dialysis Device ($Thermo\ Scientific^{TM}, 69570$), against Milli-Q water, for 1 day, at room temperature. The purified cysteine-modified chitosan, CS-CYS, was stored at 5 ºC.

2.1.2.2. Preparation of the nanogel formulation

Several formulations and ratios of the nanogel were tested to assess the most appropriate ratio of CS-CYS:Alginate:TPP (Table 1). Concentrations of CS-CYS ranging from 0.035 mg/mL to 0.35 mg/mL were combined with different concentrations of alginate between 0.025 – 0.4 mg/mL, while maintaining TPP's concentration of 0.1 mg/mL. To evaluate and optimize the concentration of TPP, concentrations of CS-CYS and alginate were kept at 0.1 mg/mL and TPP's concentration was varied between 0.025 – 0.4 mg/mL. For the plasmonic nanogel preparation, the solution of AuNRs@Si@Lip was centrifuged 20 minutes at 9000 g, redispersed in 100 µL of 0.1 mg/mL of TPP, and added

dropwise to 900 µL of 0.1 mg/mL of the CS-CYS solution, under stirring. After 10 minutes, 1 mL of Milli-Q water was added. The chitosan nanogel was added dropwise to 2 mL of 0.1 mg/mL of alginate, under stirring, and the pH was adjusted to 7.1–7.5 with NaOH 0.1 M or HCl 0.1 M. The nanogels were centrifuged at 3500 g, 15 minutes, and redispersed in 1 mL of phosphate buffer 10 mM, pH 7.4, and stored at 5 ºC, until further use.

Table 1. CS-CYS:Alg:TPP formulations tested.

[Alginate] mg/mL	[CS-CYS] mg/mL					[TPP] mg/mL
0.025	0.035	0.07	0.1	0.2	0.35	0.1
0.05	0.035	0.07	0.1	0.2	0.35	0.1
0.1	0.035	0.07	0.1	0.2	0.35	0.1
0.2	0.035	0.07	0.1	0.2	0.35	0.1
0.4	0.035	0.07	0.1	0.2	0.35	0.1

[TPP] mg/mL
0.025
0.05
0.1
0.2
0.4

2.1.2.3. Characterization techniques

To optimize the formulation of the nanogel, the zeta potential and the hydrodynamic size were assessed. DLS measurements were carried out as previously described, using a dilution of 1:10.

The nanogel particles were also characterized at different pH levels using DLS, diluting the nanogel sample in buffers with different pH values (acetate buffer 10 mM pH 3, pH 4 and pH 5; phosphate buffer 10 mM pH 6, pH 7.4 and pH 8; bicarbonate buffer 10 mM pH 9), and assessing the hydrodynamic diameter and the zeta potential. The measurements were obtained as mentioned before, and changing the solvent to PBS.

The nanogel's stability was assessed by incubating the nanogel in phosphate buffer 10 mM pH 7.4, at different temperatures, 37 ºC, 25 ºC and 5 ºC. Hydrodynamic diameter and zeta potential measurements were carried out every week, for 30 days, as already described.

Characterization of the nanogel hydrodynamic diameter under heating was also carried using DLS. The assays consisted on the measurement of the hydrodynamic size of the sample, at different pH levels, while increasing its temperature. All the assays were performed starting at 25 ºC and measurements were carried at 2 ºC intervals, until the temperature of the solution reached 50 ºC.

The nanogel was subjected to characterization under heating and cooling cycles, at pH 6 and 7.4. The assays started with the sample at 25 ºC and were based on its rapid heating until 50 ºC and rapid cooling until 25 ºC. Hydrodynamic size measurements were taken when the sample reached 25 ºC or 50 ºC.

The responsivity of the nanogel to an oxidative/reductive environment was evaluated by the exposition to H_2O_2 and different concentrations of GSH, respectively. The assays were conducted by incubating the nanogel particles in phosphate buffer 10 mM pH 7.4, 10% H_2O_2 and leaving it overnight. Different concentrations of GSH (80 mM, 10 mM, 80 µM and 20 µM) were added to the nanogel solution. The changes in the nanogel's hydrodynamic diameter and zeta potential were followed by DLS measurements, performed as described before.

Raman spectroscopy measurements of CS-CYS, non-modified chitosan, nanogel, and alginate were performed at room temperature using a LabRAM HR Evolution confocal microscope system (HORIBS France SAS, Palaiseau, France), equipped with a high-resolution grafting of 1800 grooves mm^{-1}. The excitation line, 532 nm, of an NIR diode laser was focused onto the sample by an ×50 objective with a numerical aperture (NA) value of 0.80 in a backscattering geometry. The spectra were acquired with a measured power of about 1.43 mW on the sample, with a spectral acquisition time of 5 s averaged over 10 accumulations and the range 500−1800 cm^{-1}.

For Fourier-Transform Infrared Spectroscopy (FTIR) measurements, a PerkinElmer Spectrum Two™ IR spectrometer (PerkinElmer Inc., Waltham, MA, USA), with a diamond ATR (Attenuated Total Reflection) single reflection accessory, was used. PerkinElmer Spectrum 10 Software (PerkinElmer Inc., Waltham, MA, USA) was used to draw the spectra. The analysis was performed in the mid-infrared wavenumber range, at a resolution of 4 cm^{-1}, averaging 4 scans.

Scanning Transmission Electron Microscopy (STEM) images of the nanogels and the plasmonic nanogels were obtained with a NanoSEM-FEI Nova 200 equipment, operating at 15kV, coupled to an Electron Dispersive Spectroscopic analyzer (EDS) and Electron Backscatter Diffraction EDAX- Pegasus X4M analyser and detection system (EBSD), at SEMAT/UM (Serviços de Caracterização de Materiais, Guimarães, Portugal). A small portion of the sample was placed onto a TEM 400 mesh copper grid with Formvar/Carbon (ref. S162-4 from Agar Scientific, London, UK), held by tweezers, and the excess solution was dried.

2.2. Drug release assays

2.2.1. Drug loading

2DG and carboxyfluorescein (CF) were encapsulated in the mesopores of AuNRs@Si (1:1 mass ratio), through incubation in 200 µL of acetone, for 24 hours. Afterwards, the nanoparticle solution was added to the lipid film, evaporated with a stream of ultrapure nitrogen gas, and redispersed in ethanol, as mentioned before. The aqueous solution was then centrifuged for 20 minutes at 9000 g, and the supernatant was stored for the calculation of the encapsulation efficiency. Finally, the particles were added to the nanogel as mentioned before. CF's encapsulation efficiency was determined by collecting the fluorescence intensity of the supernatant at 515 nm, at an excitation wavelength of 440 nm and using a standard calibration curve.

On the other hand, MTX was encapsulated in the nanogel's network. The encapsulation efficiency was assessed at different concentrations of MTX, by adding 0.05 mg, 0.1 mg or 0.2 mg of MTX to the 900 µL solution of 0.1 mg/mL CS-CYS. The preparation of the drug loaded nanogel followed the already mentioned technique, with the addition of 0.2 mg of MTX to the CS-CYS solution. Finally, the nanogel was centrifuged, 15 minutes at 6500 rpm, and the supernatant was stored to determine the non-encapsulated MTX and assess the encapsulation efficiency. The nanogel was resuspended in 1 mL of phosphate buffer 10 mM, pH 7.4. MTX's encapsulation efficiency was determined by measuring the absorbance at 670 nm and using a standard calibration curve.

The encapsulation efficiency was calculated using the following equation

$$EE\ \% = \frac{total\ drug - non-encapsulated\ drug}{total\ drug} \times 100\%,$$

2.2.2. Release assays

Nanogels loaded with 0.2 mg of MTX, 0.1 mg 2DG and 0.1 mg of CF were used to perform release assays. 500 µL of nanogel and 100 µL of phosphate buffer (pH 7.4) were transferred to a $Slide-A-Lyzer^{®}\ MINI$ dialysis unit, that was placed in a flask with 1.8 mL of 10 mM phosphate buffer (pH 7.4) (total volume of the assay: 2.4 mL). The influence of the presence of a high concentration of GSH was assessed by adding a 200 mM GSH stock solution to a final concentration of 10 mM. For the assays with laser irradiation at 808 nm (1 W/cm^2), the samples were irradiated for 10 minutes after each aliquot, after the 2 hours' time point. The flasks were kept under stirring in an orbital shaker at room temperature, and aliquots of 200 µL were taken from the outside of the dialysis unit and replaced with fresh buffer at 0.5, 1, 2, 4, 6, 24, 48 and 72 h. The same

assay was performed for the release at pH 6.0 and all the assays were performed in triplicate.

The concentration of drug in each aliquot was determined to quantify the drug release. MTX's release was measured using UV-Vis-NIR spectrophotometry, between 450−900 nm, at room temperature and using 10 mM phosphate buffer pH 7.4 as baseline. CF's release was determined by collecting the fluorescence intensity at 515 nm, at an excitation wavelength of 440 nm.

The concentrations obtained were converted to percentage of release using a standard calibration curve and plotted against time.

2.3. *In vitro* assays

2.3.1. Cell culture

L929 (obtained from European Collection of Authenticated Cell Cultures, ECACC, Salisbury, UK, CVCL_0462) and MDA-MB-231 (obtained from ECACC, Salisbury, UK, CVCL_0062) cell lines were cultured at 37ºC in a 5% CO2 atmosphere (HERA cell 150 incubator, Heraeus, Hanau, Germany) in Dulbecco's Modified Eagle Medium (DMEM) supplemented with 10% Fetal Bovine Serum (FBS) 1% Penicillin-Streptomycin (Pen-Strep). For every 2 to 3 days cell medium replaced by fresh supplemented DMEM. Cells were subcultured at 80 to 90% confluence by chemical detachment with trypsin-EDTA followed by centrifugation at 300 g for 5 min (Multifuge X1R, Thermo Fisher Scientific, USA) and re-suspension in fresh medium. Cell counting was performed in a Neubauer chamber (Improved Neubauer Bright-line, Boeco; Germany) after addition of 90% (v/v) Trypan Blue solution (0.4% (w/v) in PBS) to exclude non-viable cells.

2.3.2. Cell viability assay

To assess the cytotoxicity of the loaded and unloaded nanoformulations, a resazurin assay was performed. The resazurin assay is a simple and rapid colorimetric assay based on the metabolization of the non-fluorescent molecule resazurin into a fluorescent molecule, resorufin, by mammalian cells and bacteria [188]. The fluorescence intensity obtained is directly proportional to the number of metabolically viable cells. L929 and MDA-MB-231 cells were seeded in 96-well tissue culture plates at a density of 2.5×10^4 cells *per* well and incubated for 24 hours at 37 ºC, 5% CO_2.The nanogels were prepared for a concentration of 0.1 mg/mL of AuNRs, 0.05 mg/mL of MTX and 0.1 mg/mL of 2DG. After that, nanogels were diluted to a final concentration of 20.8 µg/mL of AuNRs in DMEM and incubated with the cells for 24 hours, at 37 ºC, 5% CO_2. Then, the medium was replaced by fresh medium containing 10% (v/v) of resazurin (final concentration of

0.01 mg/mL). After 3 hours of incubation at 37 ºC, 5% CO_2, the fluorescence of resorufin ($\lambda_{ex} = 560\ nm;\ \lambda_{em} = 590\ nm$) was measured using a plate reader (Biotek Instruments, Winooski, VT, USA). A positive control was included using untreated cells.

2.3.3. Cellular uptake assays

The internalization of the loaded nanogel with 2DG and MTX in MDA-MB-231 cells was evaluated using Confocal Laser Scanning Microscopy (CLSM). Confocal microscopy assays were carried out at the Confocal and Fluorescence Lifetime Laboratory at Centro de Materiais da Universidade do Porto (CEMUP), Portugal.

Firstly, MDA-MB-231 cells were seeded at a density of 2.5×10^4 cells *per* well in 8 well-µ-slides (Ibitreat, Ibidi GmbH, Munich, Germany) and incubated for 24h, at 37 ºC, 5% CO_2. Afterwards, the cells were incubated with 200 µL of the loaded nanogel (1.3 µg/mL AuNRs; 0.65 µg/mL MTX), for 1 hour and 3 hours. After the incubation time, the cells were rinsed three times with PBS and were fixed with a formalin solution for 30 minutes, at room temperature, and stained with Hoechst 33342® (8 µM in PBS) for 10 minutes. The images were acquired on a Leica Stellaris 8 Confocal Microscope (Leica Microsystems, Wetzlar, Germany) using a $\lambda_{ex}/\lambda_{em}$ of 405/ 420-480 nm (Hoechst 33342) and $\lambda_{ex}/\lambda_{em}$ of 610/650–690 nm (MTX). The images were acquired with a resolution of 1024 × 1024 using a 63×/1.4 oil immersion objective.

3. Results and Discussion

3.1. Development of plasmonic nanolipogels

3.1.1. Preparation of plasmonic particles

The AuNRs were synthesized by a seedless method, described by *Roach et al* [110]. In this method, the gold salt solution is added to a solution of CTAB and sodium oleate, changing the color of the solution to dark yellow, due to the complexation of $[AuCl_4]^-$ and $[CTA]^+$. The reduction of Au^{3+} by sodium oleate causes a change of the color of the solution back to a transparent solution. After that, silver nitrate is added to contribute to the anisotropic growth of the particles, through its reduction on the surface of the particles by ascorbic acid, a mild reducing agent. The synthesis requires a strong reducing agent, sodium borohydride, to reduce the gold to Au^0 and start the nucleation of the particles. After 4 hours reacting, the solution of AuNRs presents a dark red color (Figure 13A), indicative of a LSPR band located at around 800 nm. The obtained suspensions were characterized through UV-Vis-NIR spectrophotometry, DLS and TEM.

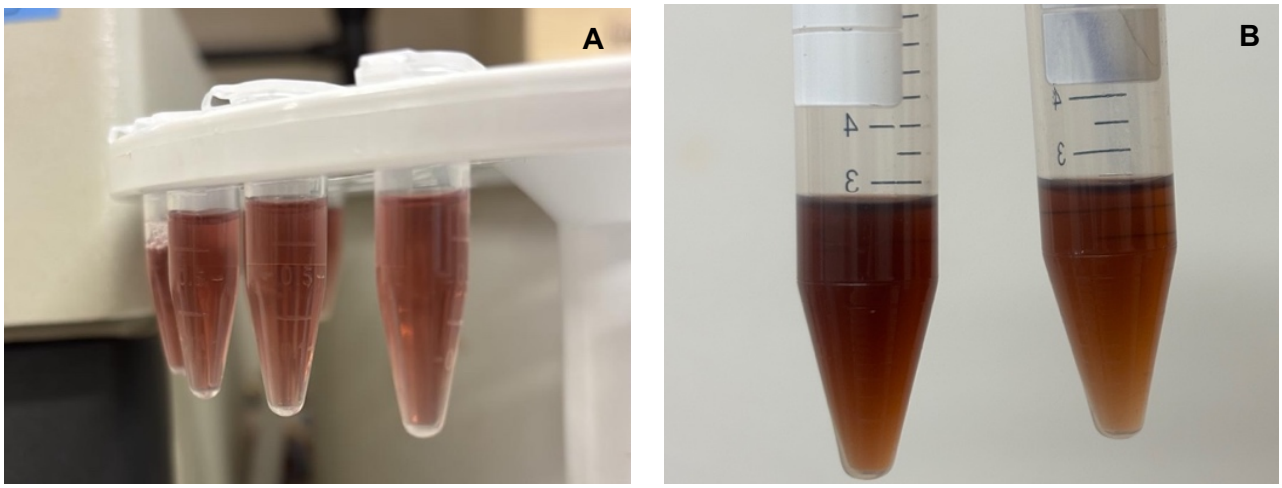


Figure 13. Photographic register of the (A) AuNRs suspension in water and (B) AuNRs@Si in ethanol.

The absorption spectrum of AuNRs (Figure 14A) displays an LSPR band maximum in the NIR region, that varies between 800–862 nm, which is ideal for biomedical applications, and a TSPR band maximum of 509–511 nm [189]. The evidence of the two absorption bands indicates the presence of anisotropic (rod shaped) nanoparticles in the suspension. With DLS measurements, the hydrodynamic diameter and the zeta potential of the AuNRs was assessed. The hydrodynamic diameter corresponds to the diameter of a spherical particle with the same diffusion coefficient as the nanoparticles of the measured sample. The AuNRs' sample had two populations with different hydrodynamic diameters, one around 42 nm ± 22 nm (polydispersity index <0.3), correspondent to the AuNRs and a smaller one with 6 nm ± 0.1 nm, that may be associated with the presence of gold spheres or CTAB micelles. The zeta potential (the charge at the surface of the particles) of the nanoparticles, + 64 mV ± 8 mV is in line with published works [190], [191], and is associated with the CTAB molecules present at the surface of thegold.

The addition of the mesoporous silica layer is based on the use of the CTAB coating as a template for the polymerization of TEOS on the surface of gold nanoparticles (Figure 13B). AuNRs@Si's absorption spectrum (Figure 14A) presented a shift of the LSPR band of ≈9 nm ± 4 nm to ≈ 848 nm, that can be associated with a change of the refractive index on the surface of the AuNRs [190], [192]. The addition of the mesoporous silica layer may have exposed the AuNRs to the solvent, water, which has a smaller refractive index than CTAB molecules, therefore causing a blue shift in the LSPR band [192]. The hydrodynamic diameter of the AuNRs@Si was around 148 nm ± 25 nm (polydispersity index <0.3), which represents an increase comparing with the non-coated AuNRs' hydrodynamic diameter, suggesting a successful coating. Besides, a negative

zeta potential of -24 mV ± 3 mV was obtained, and can be associated with the presence of Si-OH bonds, indicating the formation of a silica layer.

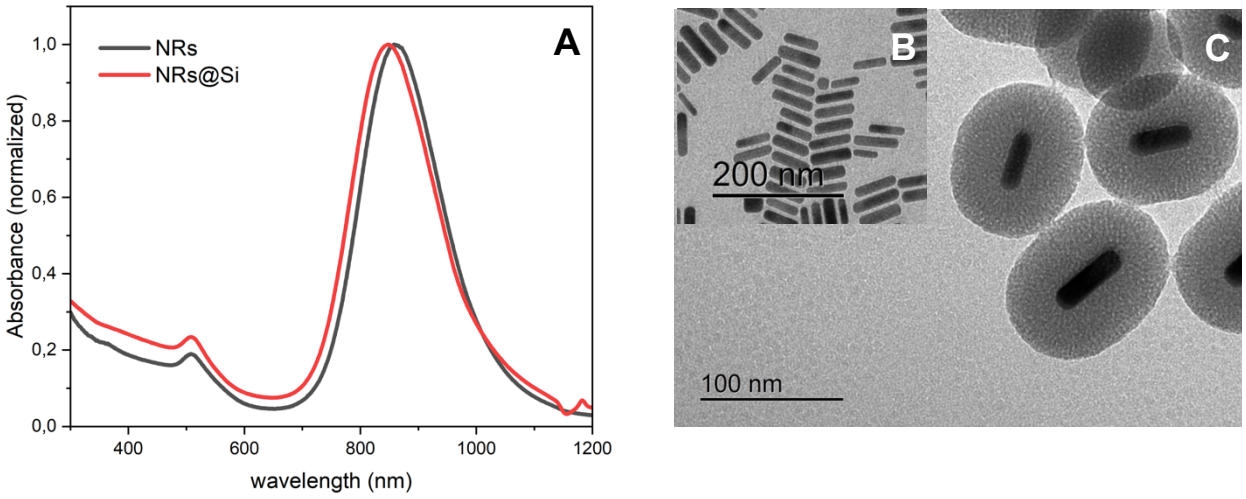


Figure 14. (A) Absorption spectra of AuNRs and AuNRs@Si dissolved in ultrapure water, in 1:10 ratio. (B) TEM image of AuNRs and of (C) AuNRs@Si.

The TEM images show well dispersed rod-shaped nanoparticles (Figure 14B) with an average size of 61 nm ± 6 nm of length and 17 nm ± 2 nm of width, corresponding to an aspect ratio of ≈ 3.6 ± 0.5, which is in line with other published works [193]. TEM images of AuNRs@Si (Figure 14C) confirmed the addition of a silica layer and the presence of random mesopores. The images show mesoporous particles containing a single AuNR inside and without AuNRs. In addition, the thickness of the silica was ≈ 37.8 nm ± 0.6 nm and the average size of the particles increased to 112.6 nm ± 6 nm of length and 87.9 nm ± 1.8 nm of width. Besides, the aspect ratio of the nanoparticles decreased to ≈1.3, which is similar to results published in other works [194].

Different lipid concentrations were tested to optimize the particles' coverage with a lipid layer. All the concentrations (0.1 mM, 0.2 mM, 0.3 mM and 0.4 mM) were assessed for a DPPC:cholesterol ratio of 7:3. The lipid bilayer was added through the preparation of a thin lipid film and its resuspension in the particle solution, promoting the formation of a lipid layer around the dispersed nanoparticles. DLS measurements were carried out to obtain the zeta potential and the hydrodynamic diameter of the particles. The particles with higher lipid concentrations presented a less negative zeta potential compared with the lower concentrations. The zeta potential shows a decrease of the surface charge of

the particles from -24 ± 3 mV to -19 ± 1 mV with the addition of the lower concentration of lipids, and -11 ± 0.1 mV with the higher lipid concentration. This less negative surface charge of the particles suggests their coverage with the lipid layer, as DPPC is a zwitterionic phospholipid and may neutralize the surface charge. The hydrodynamic diameter of the particles increased from 148 ± 25 nm to 167 ± 3 nm with the addition of the lipid bilayer. The change of the hydrodynamic diameter is more pronounced when adding higher lipid concentrations, reaching 256 ± 10 nm at the higher concentration tested, suggesting some aggregation of the AuNRs@Si@Lip or an increase of size due to the addition of a new layer. The concentration 0.4 mM of lipids was chosen as the one that indicated a better coverage of the particles, without destabilizing the nanoparticles.

3.1.2. Development of modified nanogels

Cysteine was covalently bonded to chitosan by firstly activating the carboxyl group with a coupling agent, EDC, to promote its nucleophilic attack to the free amines of the glucosamine residues (Figure 15). The reaction was performed under acidic pH 4.5-5 to keep the chitosan soluble, with the amines protonated.

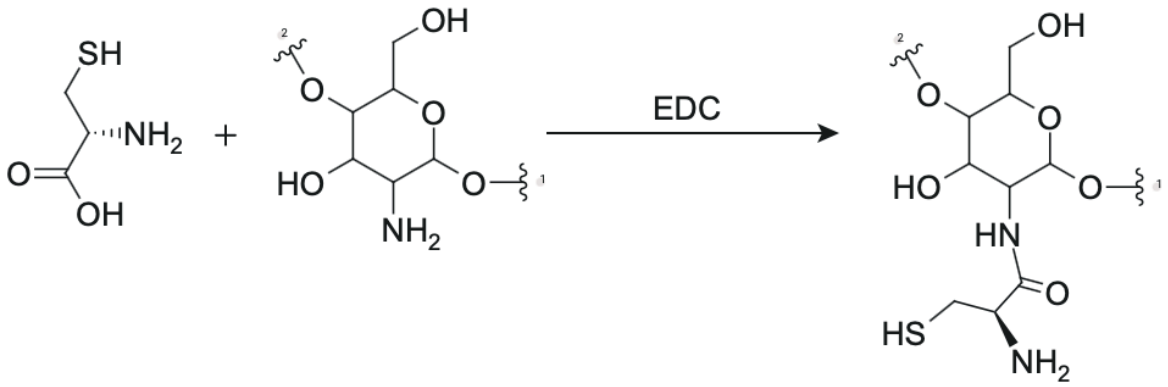


Figure 15. Reaction scheme for the conjugation of chitosan with L-cysteine.

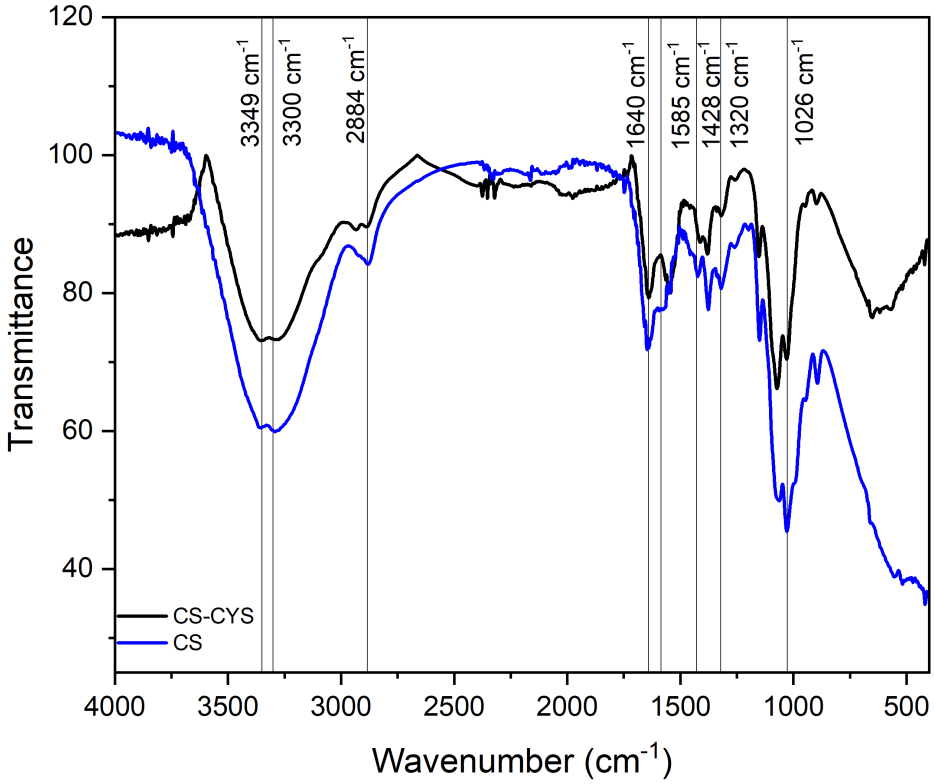


Figure 16. FTIR spectra of CS (blue) and CS-CYS (black).

The modification of chitosan with L-cysteine was evaluated with FTIR spectroscopy (Figure 16). The FTIR spectrum of chitosan showed a broad absorption band with 2 peaks at 3300-3400 cm^{-1}, corresponding to the stretching vibrations of the free primary amine and hydroxyl groups [195], [196]. A peak at 2884 cm^{-1} was also observed, attributed to –OH stretching. The amide I band, due to the C=O stretching of secondary amides, appeared at 1640 cm^{-1}, while the amide II band, related to the N–H bending of N-acetylated residues, was detected at 1585 cm^{-1} [195], [197]. Additional peaks around 1428 cm^{-1} - 1320 cm^{-1} corresponded to N–H stretching of amide and ether bonds, and amide III bands. The peak at 1026 cm^{-1} can be assigned to C–O stretching vibrations of secondary hydroxyl groups (–CH–OH, typical of cyclic alcohols) and primary hydroxyl groups ($–CH_2–OH$, typical of primary alcohols).

Chitosan was conjugated with cysteine forming an amide bond between the free primary amines of chitosan and the carboxyl groups of cysteine. The CS-CYS's FTIR spectrum (Figure 16) shows an attenuation of the 2 peaks at 3400-3300 cm^{-1} observed before the modification. This attenuation suggests that a modification of chitosan may have occurred, like the formation of an amide bond, weakening the free amine's signal.

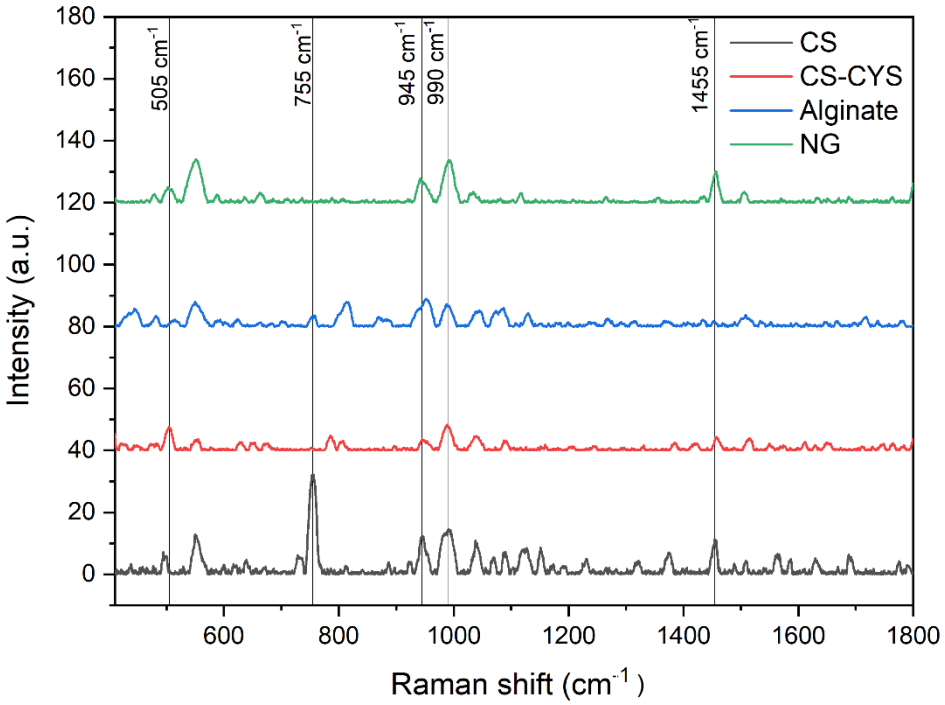


Figure 17. Raman spectra of chitosan (black), CS-CYS (red), alginate (blue) and the nanogel (green).

Raman spectroscopy of the polymers and the nanogel was performed to confirm the modification with cysteine and the composition of the nanogel and the obtained spectra are represented in figure 17.

The Raman spectrum of chitosan presents peaks around 1455 cm^{-1} and 945 cm^{-1} that can be attributed to the stretching vibration of the rings of the backbone (–CH–CH_2–OH) [198]. The stretching vibrations of the free primary amine is associated with the peak at 755 cm^{-1}[196]. Alginate's spectrum also presents peaks around 940-1000 cm^{-1}, characteristics of the vibration of the rings of the constituent monomers.

In the CS-CYS spectrum, a peak at 505 cm^{-1} can be associated to the stretching of C-S, which suggests that the modification of chitosan with the aminoacid was successful [199]. Besides, the peak of the free primary amine at 755 cm^{-1}, present in the spectrum of the non-modified polymer, is not observed in the CS-CYS spectrum, which may indicate that a modification occurred in the amine, corroborant of the conjugation of chitosan and cysteine.

The nanogel spectrum presents the peaks that are characteristic of chitosan and alginate and also the peak at 505 cm^{-1}, that may suggest the presence of a modification of the chitosan, confirming the theoretical constitution of the nanogel.

The nanogels were prepared by combining ionic gelation and polyelectrolyte complexation. Firstly, a CS-CYS nanogel was prepared by ionic gelation. The addition of a counter ion, TPP, to a CS-CYS solution creates a network via electrostatic interactions with the positively charged groups of the chitosan polymer chains. Then, the CS-CYS nanogel is added dropwise to an alginate solution to allow the surrounding of the droplet by an alginate layer, forming nanoparticles with a chitosan core. Different concentrations of CS-CYS, alginate and TPP were assessed to optimize the nanogel's formulation. In general, the solutions were turbid and well dissolved, except for some formulations which contained some aggregates, which suggests some instability of the particles (Table 2 and figure 18).

Table 2. Visual observations of the obtained nanogel's formulations. With aggregates (X) or without aggregates (Ø).

[Alginate] mg/mL	[CS-CYS] mg/mL					[TPP] mg/mL
-	0.035	0.07	0.1	0.2	0.35	0.1
0.025	Ø	X	X	X	Ø	0.1
0.05	X	X	Ø	X	X	0.1
0.1	X	X	Ø	Ø	X	0.1
0.2	X	X	Ø	Ø	Ø	0.1
0.4	X	Ø	Ø	X	X	0.1

[TPP] mg/mL
-
0.025 Ø
0.05 Ø
0.1 Ø
0.2 X
0.4 X

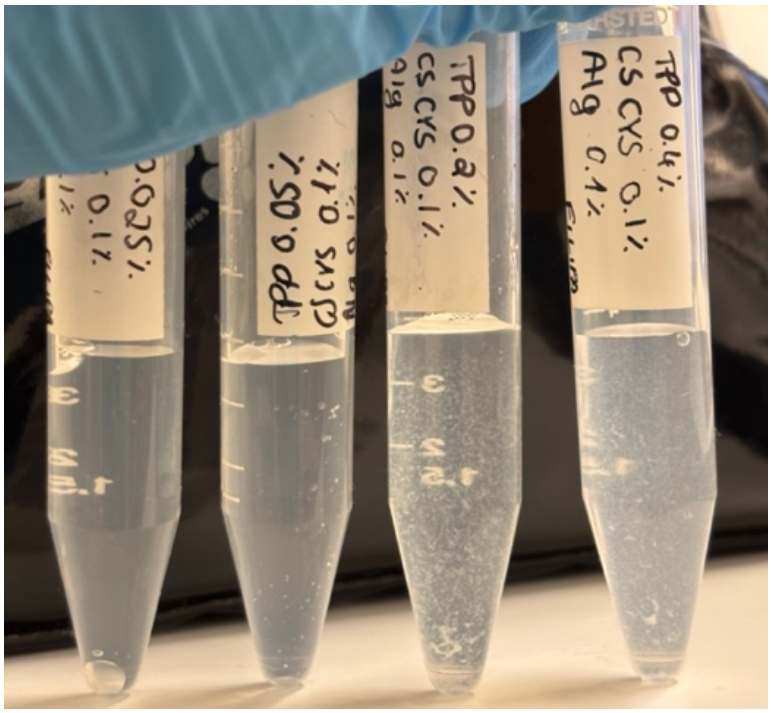


Figure 18. Photographic register of the nanogels with 0.1% alginate, 0.1% CS-CYS and different concentrations of TPP: 0.025%, 0.05%, 0.2% and 0.4% (from left to right).

DLS measurements of the nanogel were performed to characterize and optimize the formulation. When maintaining alginate's concentration and increasing chitosan-cysteine's, the zeta potential of the particles (Figure 19A) increased (in absolute value) until 0.1% of chitosan and then it started decreasing at higher concentrations. This suggests that the same concentration of alginate cannot cover higher concentrations of CS-CYS. At 0.1% of CS-CYS, the particles were more negatively charged, and consequently, had better colloidal stability, which can explain the absence of aggregates in solution. However, when using concentrations of alginate ≥ 0.2%, a zeta potential of < -25 mV was obtained for every concentration of CS-CYS used, suggesting that full coverage of the CS-CYS layer was reached. The variation of the concentration of TPP, the counter-ion, did not cause a very significant change in the zeta potential of the particles, varying from -33 mV (0.025% TPP) to -20 mV (0.4% TPP). The increase of TPP's concentration, also increases the degree of chitosan's crosslinking, decreasing the content of free amines [200]. This may reduce the electrostatic interactions between chitosan and alginate, leading to a decrease of the thickness of the alginate layer and consequently a decrease in the zeta potential of the nanogel.

Besides that, the hydrodynamic size (Figure 19B) was also an important parameter for choosing the nanogel formulation, as smaller particles can easily cross biological barriers like cell membranes. In general, with the increase of the concentration of CS-CYS for a

fixed concentration of alginate, an increase in size and polydispersity was observed, starting at ≈ 208 nm (0.05% alginate + 0.035% CS-CYS) and reaching ≈ 535 nm (0.025% alginate + 0.4% CS-CYS). At lower concentrations of CS-CYS (<0.07%), the hydrodynamic size increases with the concentration of alginate, reaching 294 nm, at the highest concentration. The solution of particles obtained with 0.4% of alginate and 0.4% of CS-CYS was more viscous, and therefore, could not be filtered and measured. When varying the TPP's concentration, the hydrodynamic size decreased from 388 nm (0.025% TPP) to 250 nm (0.1% TPP) and then increasing to 314 nm at the highest concentration (0.4% TPP).

Nanogels developed with 0.1% CS-CYS, 0.1% alginate and 0.1% TPP comprised a smaller hydrodynamic size and a more negative zeta potential, suggesting more colloidal stability and better physicochemical features.

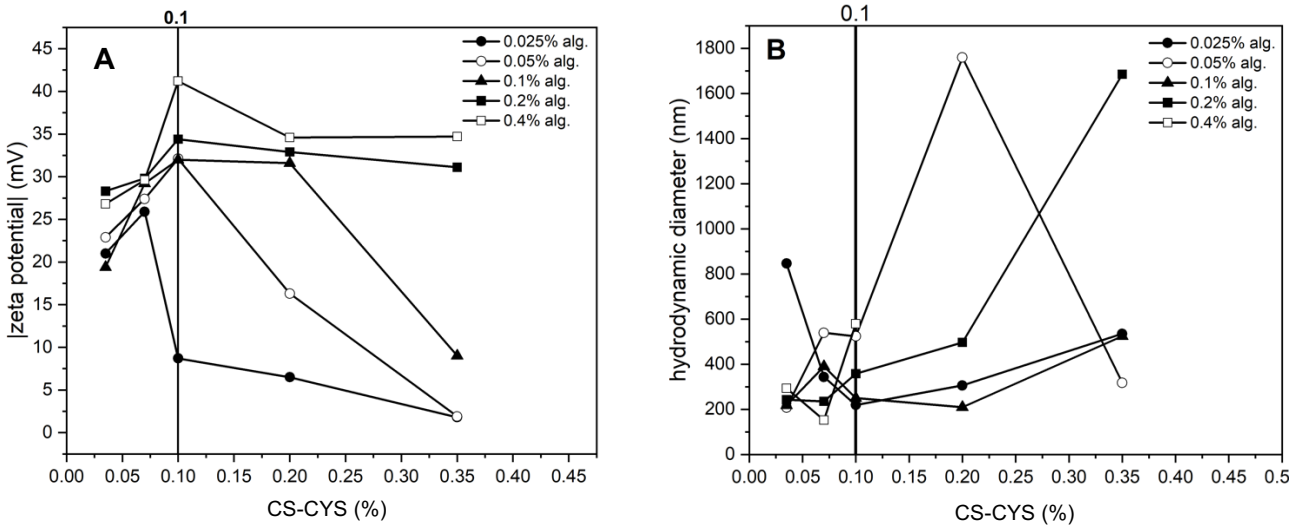


Figure 19. DLS characterization of the different formulations of nanogel. Zeta potential in absolute value (A) and hydrodynamic diameter (B) values. Concentrations assessed: CS-CYS 0.035-0.35 mg/mL; Alginate 0.025-0.4 mg/mL; TPP 0.1%.

The selected nanogel formulation displayed a negative zeta potential of -32 ± 1.4 mV, when measured diluted in Milli-Q water, and a hydrodynamic size of 250 ± 8 nm (polydispersity index ≈0.3), which is in line with the literature reports [197].

The nanogel particles were characterized at different pH levels from pH 3 to pH 9, using DLS to assess changes in the hydrodynamic diameter and zeta potential (Figure 20). When diluted in 10 mM phosphate buffer pH 7.4, the particles presented a zeta potential of ≈ -26 ± 0.6 mV, which is in line with other reports for chitosan/alginate nanogels [197]. This surface charge indicates stability of the nanogel in physiological conditions of cells [197]. Besides, the nanogel also presented a hydrodynamic size of 322 ± 6 nm and better

polydispersity (≈0.1). The increase in the hydrodynamic diameter, comparing with the results obtained in Milli-Q water, can reflect a swelling of the nanogels particles in buffer solution. The most negatively charged nanoparticles, with zeta potential of -28 ± 0.8 mV, were obtained when using a pH 9 buffer solution. The zeta potential of the particles becomes less negative with the decrease of the pH level, reaching ≈ -5 ± 0.4 mV at pH 3. At higher pH values, the outer layer, composed of alginate, is not protonated (pK_a 3.6), and acquire a negative charge and, as the pH level decreases, the concentration of H^+ in the medium rises. The increase of H^+ in the medium leads to the protonation of the carboxyl groups of the alginate layer and the surface charge of the nanoparticles is almost neutralized.

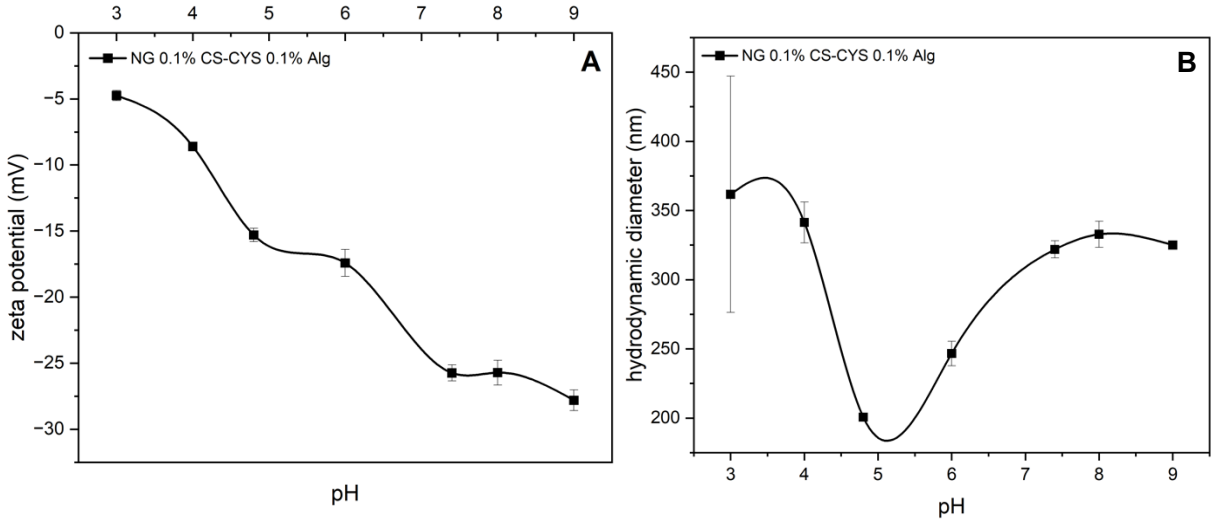


Figure 20. DLS characterization, zeta potential (A) and hydrodynamic diameter (B) of the nanogel at different pH conditions pH 3-9.

On the other hand, the hydrodynamic diameter displays a different behavior. At pH 9, the hydrodynamic diameter of the particles is ≈ 325 ± 2 nm (polydispersity index (pdi) = 0.2) and it decreases until pH 4.8, reaching ≈ 201 ± 2 nm. As the pH decreases, the free primary amines of the chitosan's chains (pK_a 6.5), start becoming protonated and the electrostatic interactions between chitosan and alginate are enhanced, leading to a contraction of the nanogel's network and a decrease in size. From pH 4.8 to pH 3, an increase in the hydrodynamic diameter of the nanogel is observed, reaching ≈ 362 ± 85 nm. The decrease of pH, results in the protonation of a significant number of carboxyl groups of the alginate's chains and of the free primary amines of chitosan, leading to a neutralization of alginate and a weakening of the electrostatic interactions

between the two polymers. This weakening of the interactions leads to a loosening of the polymers network and consequently to an increase in the hydrodynamic diameter.

As the nanogel will be used as a vehicle to transport and deliver plasmonic nanoparticles for combined chemophototherapy, the nanogel's hydrodynamic diameter was followed under heating at different pH levels (Figure 21). In this assay, the temperature of the sample was increased, and the hydrodynamic diameter was measured in 2º C intervals, until 50º C.

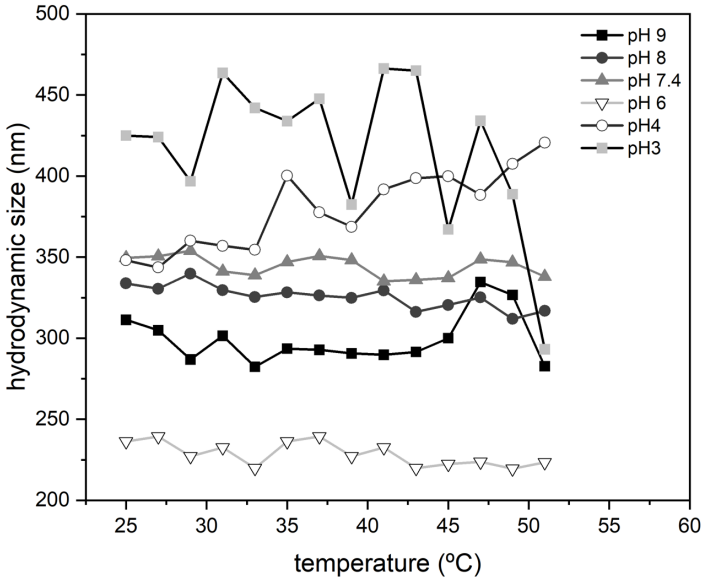


Figure 21. Hydrodynamic size characterization of the nanogel upon the increase of the temperature. Measurements were taken under 2ºC intervals, from 25 ºC to 51 ºC.

Between pHs 6 and 8, the hydrodynamic diameter varied in maximum 28 nm, which is not a significant variation, and suggests stability of the particles in those conditions. At pH 9, 4 and 3, a higher variation was observed and can reflect some degradation of the alginate layer and a swelling of the polymer's network, leading to an increase in the apparent size (figure 21). This assay indicates that the nanogel is stable and doesn't degrade under slow heating at physiological and pathological pH conditions.

The nanogel was also subjected to characterization under heating and cooling cycles, at pH 7.4 and 6 (Figure 22A and 22B, respectively). The assays started with the sample at 25 ºC and were based on its rapid heating until 50 ºC and rapid cooling until 25 ºC. Hydrodynamic size measurements were taken when the sample reached 25 ºC or 50 ºC. The results are represented in figure 22 and show a rapid variation of the hydrodynamic diameter when the nanogel is subjected to rapid heating and cooling. At pH 7.4 (Figure 22A), the nanogel's hydrodynamic diameter suffered a maximum variation of

123 nm, while at pH 6 (Figure 22B), the maximum variation was 56 nm. The results suggest that the nanogel's network has better resistance to temperature-induced stress, at pH 6, indicating stronger electrostatic interactions between the two polymers, stabilizing the particles.

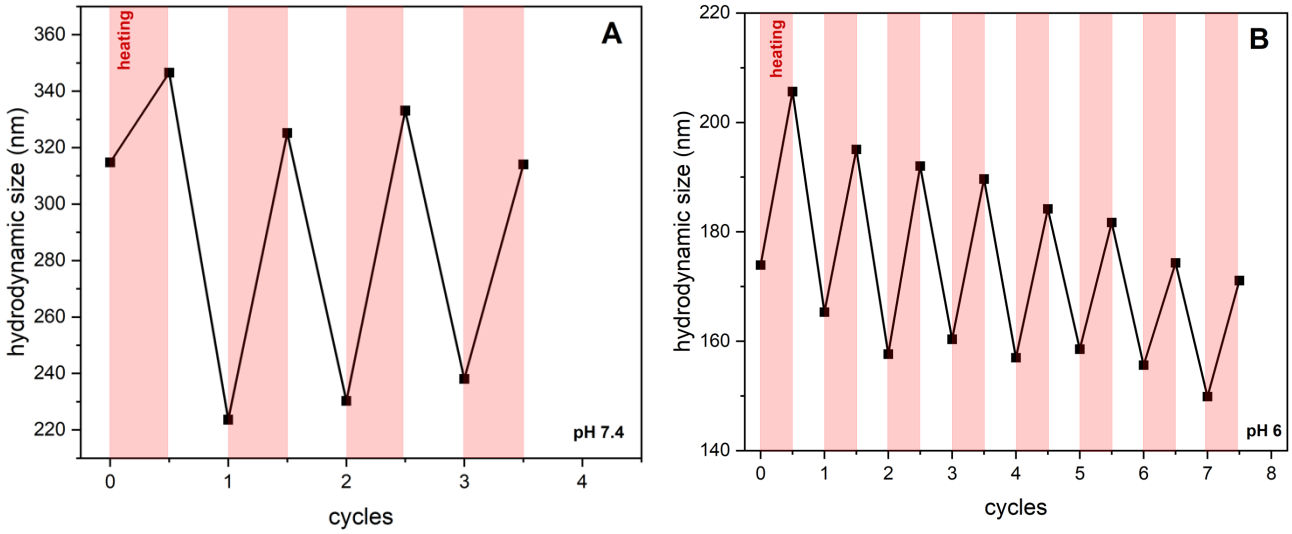


Figure 22. Hydrodynamic size characterization of the nanogel upon heating cycles (50ºC) and cooling cycles (25ºC), at different pH levels, pH 7.4 (A) and pH 6 (B).

Comparing the results obtained under slow heating (Figure 21) and rapid heating (Figure 22), at pH 7.4 and 6, it can be inferred that the particles displayed different behaviors. When under rapid heating, the particles suffered a significant change in the hydrodynamic diameter (>55 nm), while under slow heating, the variation was not significant (<30 nm). This indicates that when the nanogel is slowly heated, it has time to distribute the energy evenly and minimize the internal stress caused by the increase of the temperature. On the other hand, when increasing the temperature rapidly, the nanogel's outer layers may be heated faster than the inner layers, causing stress and expansion of the structure.

The nanogel is composed of cysteine modified chitosan. Cysteine's thiol groups can interact with each other and originate disulfide bonds that are formed under oxidative conditions and broken under reductive conditions. To evaluate the nanogel's responsivity to an oxidative/reductive environment, it was exposed to H_2O_2 and different concentrations of GSH (20 μM, 80 μM, 10 mM and 80 mM), respectively. The concentrations of GSH were chosen according to reported values to simulate the conditions of the extracellular physiological environment (20 μM), the extracellular tumor

environment (80 μM) and the intracellular tumor environment (10 mM) (Figure 23). The changes in the nanogel's hydrodynamic diameter and zeta potential were followed by DLS measurements.

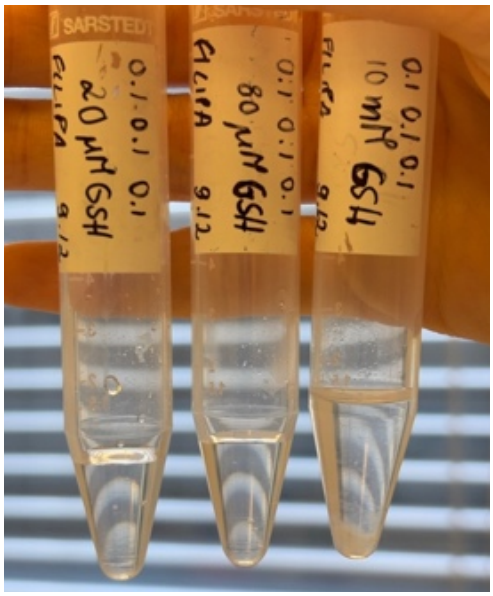


Figure 23. Photographic register of the nanogels 20 μM, 80 μM and 10 mM (from left to right) of GSH, at the 144 hours' time point.

The results obtained from DLS measurements are displayed in figure 24.

At the beginning of the assay the nanogel exhibited a zeta potential of -32 ± 1.9 mV and a particle size of 271 ± 16 nm. The particles were then incubated in phosphate buffer 10 mM pH 7.4, 10% H_2O_2, to promote the formation of disulfide bonds between cysteine residues. After the addition of H_2O_2, the zeta potential of the nanogels increased to -24 ± 3 mV and the hydrodynamic size slightly decreased to 240 ± 9 nm. This variation may suggest that disulfide bonds were formed, causing the contraction of the nanogel's network and a decrease of the hydrodynamic size.

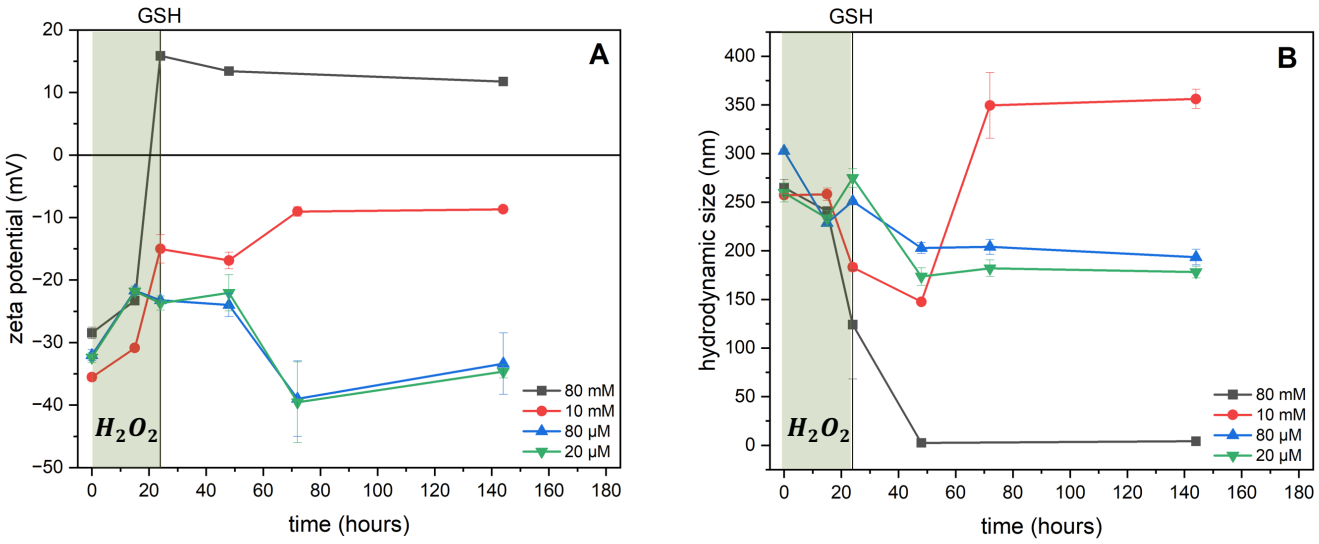


Figure 24. Characterization of the nanogel, zeta potential (A) and hydrodynamic diameter (B) measurements, during the redox sensitivity assay. H_2O_2 was added to the nanogel after the first mesaurement; GSH was added after 24 hours of incubation with H_2O_2. DLS measurements were performed at different time point, until 144 hours.

After incubation with H_2O_2 overnight, different concentrations of GSH were added to reduce the disulfide bonds and the samples were characterized at different time points to follow the nanogel's behavior. The lower concentrations of GSH, 20 μM and 80 μM, caused an initial small increase of the zeta potential, to -22 ± 1 mV, and a small increase of the hydrodynamic diameter, to 275 ± 10 nm and 250 ± 1 nm, respectively. These changes may reflect a loosening of the nanogel's network due to the breaking of some of the disulfide bonds, but without compromising the structure and stability of the particles. On the other hand, with the addition of 10 mM of GSH, the nanogel's surface charge shifted to -15 ± 2 mV and the hydrodynamic diameter to 183 ± 4 nm. When increasing the concentration of GSH even more, to 80 mM, a positive zeta potential of +16 ± 0.1 mV and a hydrodynamic size of 124 ± 56 nm was observed. Visually, in the samples with higher concentrations of GSH, a turbid deposit was formed (Figure 23). In these cases, the concentration of GSH led to a significant decrease of the size and increase of the surface charge, suggesting some disintegration of the structure of the particles, through total or partial detachment of the alginate layer.

After 72 hours of incubation in GSH, the samples suffered some changes and stabilized. In the case of the lower concentrations of GSH, 20 μM and 80 μM, the nanogel's zeta potential decreased to -39 ± 6 mV, and the hydrodynamic diameter decreased to 182 ± 9 nm and 204 ± 8 nm, respectively. However, when incubated with 10 mM of GSH, the zeta potential of the nanogels increased, almost reaching neutrality, -9 ± 0.8 mV, and the hydrodynamic diameter increased, reaching 349 ± 34 nm. The results may suggest a thinning of the alginate layer and a swelling of the chitosan layer, due to the loosening of

the network, after the exposure to the buffer and due to the disruption of the disulfide bonds. Finally, the sample incubated with 80 mM of GSH, presented a positive zeta potential of +13 ± 0.4 mV and a hydrodynamic size of 2.5 ± 0.5 nm, which points to a total degradation of the nanogel. These results may reflect the nanogel's behavior inside the healthy and tumor cells, showing some degradation in diseased cells and maintaining its integrity in physiological environments.

The nanogel's stability was assessed by incubating the nanogel in phosphate buffer 10 mM pH 7.4, at different temperatures, 37 ºC, 25 ºC and 5 ºC and characterizing it every week, for 30 days (Figure 25). The zeta potential of the nanogel presented a higher shift when stored at 25 ºC, increasing 15 mV in 30 days, which may suggest some degradation of the alginate layer, resulting in a slight neutralization of the surface charge. As for the hydrodynamic diameter, when stored at 5 ºC, the variation was more prominent, decreasing 89 nm, maybe due to the contraction of the network, to less aggregation of the particles or to some disintegration of the structure.

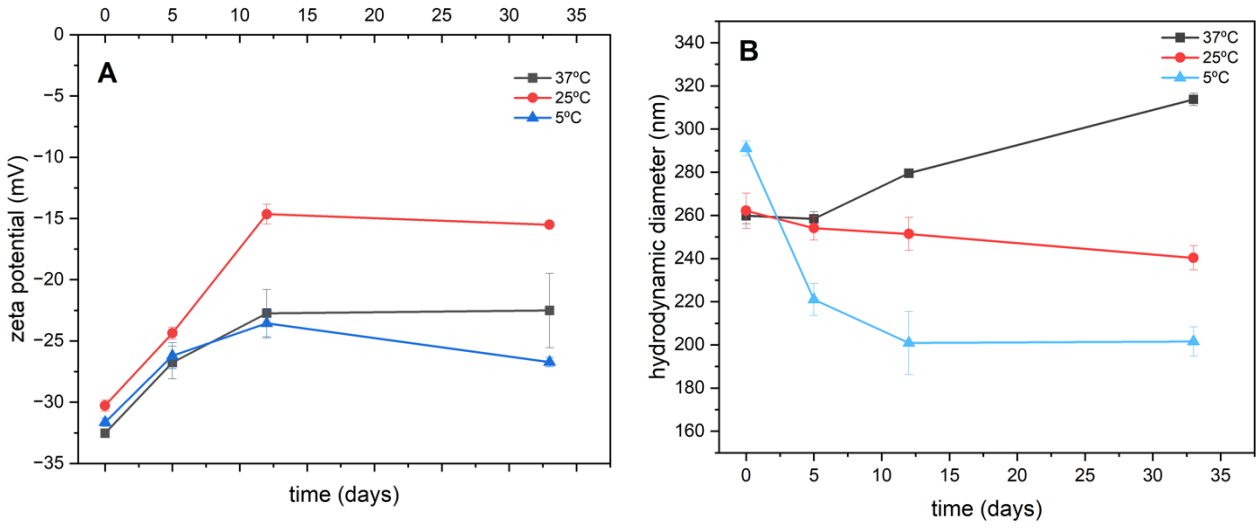


Figure 25. Storage stability of the nanogel at different temperatures, 37 ºC, 25 ºC and 5 ºC. Zeta potential (A) and hydrodynamic diameter (B) measurements of the nanogel were performed over 30 days.

After the characterization of the nanogel, the plasmonic nanoparticles were encapsulated in the nanogel's network, through a procedure reported in previous works [75]. The empty nanogel particles displayed very good polydispersity (< 0.1), a negative zeta potential of ≈ -26 ± 0.6 mV with a hydrodynamic size of 322 ± 6 nm (Figure 26). Plasmonic nanogels displayed a similar zeta potential of -27 ± 2 mV and a hydrodynamic size of 288 ± 25 nm (Figure 26). The smaller hydrodynamic size may indicate a contraction of the nanogel's network due to interactions with the plasmonic nanoparticles or the formation of a gel layer around the nanoparticles.

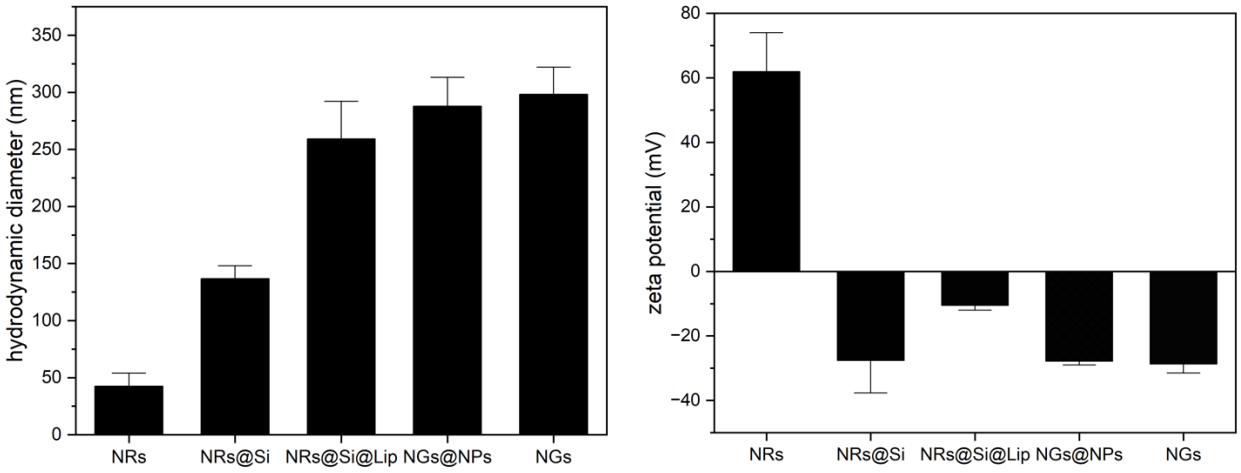


Figure 26. Size and zeta (ζ) potential characterization of AuNRs, AuNRs@Si, AuNRs@Si@Lip, NGs@NPs and NGs.

SEM images of the empty nanogels revealed particles with no defined morphology (Figure 27A). On the other hand, the images of the plasmonic nanogels displayed regular and round particles with an apparent smooth surface, and an average size of 107 ± 6 nm (Figure 27B). The size of the particles is significantly smaller than the one obtained by DLS measurements. Electron microscopy is performed using a dried sample and in vacuum, while the hydrodynamic size is performed with the particles in solution. A higher hydrodynamic size can be explained by the swelling of chitosan and alginate in aqueous solution. In the center of the rounded particles, in both SEM and STEM images of the plasmonic nanogels (Figure 27B and 27C), it can be observed a rod shape figure, which suggests that the encapsulation of AuNR@Si@Lip was successful and that the plasmonic nanoparticles are coated with the nanogel.

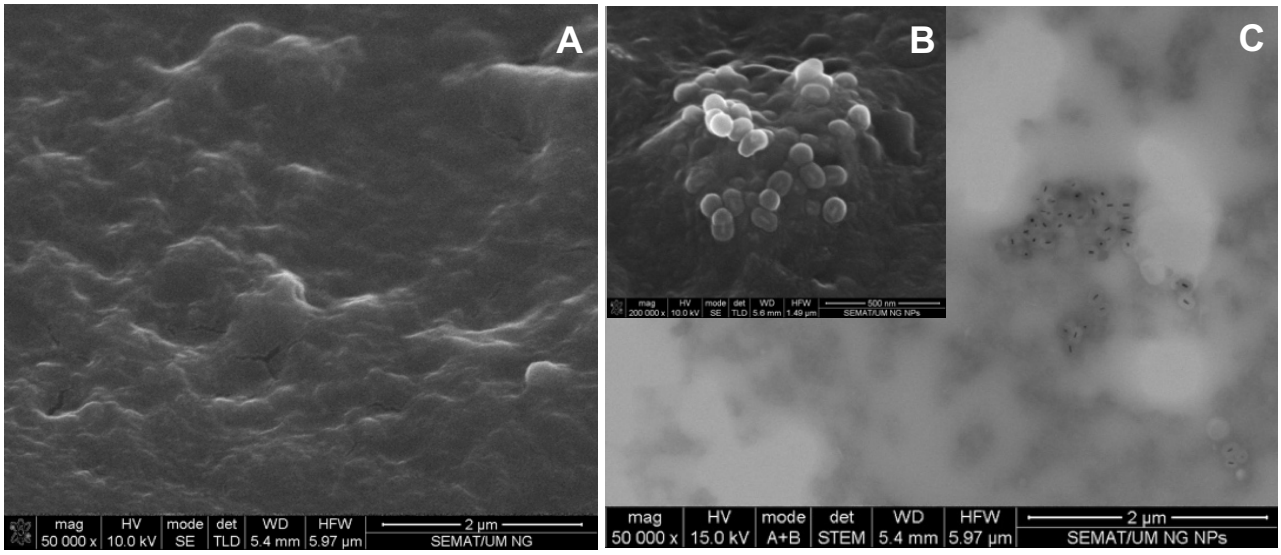


Figure 27. SEM images of empty nanogel (A); scale bar 2 µm. SEM (B) and STEM (C) images of plasmonic nanogel; scale bar 500 nm and 2 µm, respectively.

3.2. Drug release assays

The release profile of MTX from the nanogel's network, and the release profile of CF from the mesopores of the silica layer were assessed under different conditions. The absence and the presence of 10 mM of GSH, different pH levels (6 and 7.4) and laser irradiation were the conditions used to evaluate the release profiles of the different agents. 2DG doesn't absorb in the UV-Vis-NIR window and doesn't emit fluorescence, making it difficult to detect and quantify. To simulate the release profile of 2DG, CF was used as a model compound. The obtained results were used to compare with the release profile of MTX and assess if the release is sequential and controlled by different stimuli.

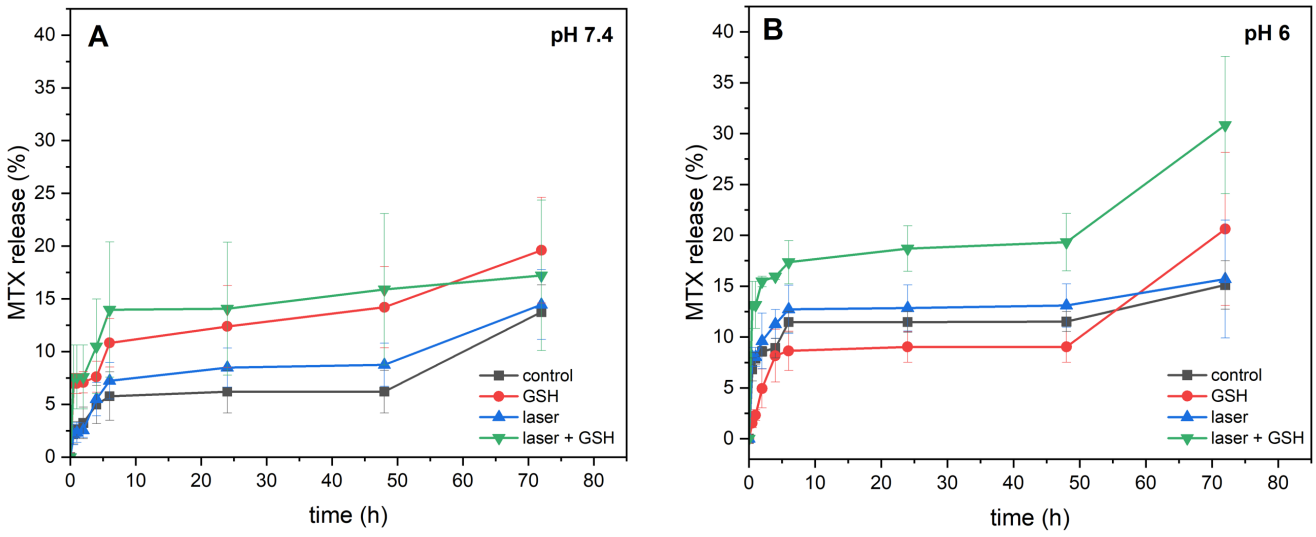


Figure 28. *In vitro* release profiles of MTX from the plasmonic nanogels, over 72h, at pH 7.4 (A) and 6 (B) at different conditions (10 mM GSH and 808 nm laser irradiation). The assays were performed at room temperature and in triplicate.

MTX is a molecule composed of three planar rings and two carbonated chains with hydroxyl groups and secondary amines. Mitoxantrone was encapsulated in the chitosan-cysteine layer of the nanogel and the encapsulation efficiency was evaluated for different concentrations of MTX, 0.05, 0.1 and 0.2 mg/mL. The loading efficiency decreased with MTX's concentration being 98%, 70% and 67% respectively. For the release assays, the nanogels were loaded with 0.2 mg/mL of MTX.

The results of the release assay of MTX are displayed in figure 28. Overall, the nanogels displayed an initial burst release that slows after 6 hours of assay, similarly to previous reports envolving chitosan/alginate nanogels [75]. This initial release can be associated with the presence of drug molecules adsorbed in the interface of CS-CYS and alginate' layers. In general, a higher release was observed at pH 6, reaching a maximum release of 31% of the initial content after 72 hours of release, while at pH 7.4, the maximum release was around 20%. At pH 6, chitosan's free amines are more protonated and can cause the swelling of the particles and promote the release of the content. Besides, MTX is more protonated at pH 6, increasing its affinity for the aqueous environment and creating more repulsion with chitosan's amines. Moreover, DLS measurements of the nanogels indicate that at pH 6, the nanogel has a smaller hydrodynamic diameter than at pH 7.4 (previously mentioned in Figure 20B), which will increase the repulsion between MTX and chitosan and promote MTX's release. The results suggest that the laser irradiation slightly enhances the drug release from the nanogel's network. When subjected to rapid heating the nanogel suffers an increase in size, possibly due to the expansion of the network, which may promote the release of mitoxantrone. Besides, the presence of GSH in the medium, which can degrade disulfide bonds that might be present between the cysteines of the nanogel, also increased the release of the drug. DLS measurements of the nanogels subjected to the same concentration of GSH, allowed to observe a reduction of the zeta potential of the particles (previously mentioned in Figure 24A), which suggest a desintegration of its structure. Besides, the increase of the hydrodynamic size (previously mentioned in Figure 24B) suggests a swelling of the chitosan layer, when exposed to the aqueous acidic medium. The DLS results indicate that in those conditions, in the presence of 10 mM of GSH and pH 6, the nanogel degrades which leads to a higher release of the cargo (Figure 28B).

These results clearly suggest that the drug's release from the nanogel's network can be triggered by different stimuli, endogenous and exogenous, such as acidic pH and high concentrations of GSH, and also by laser irradiation.

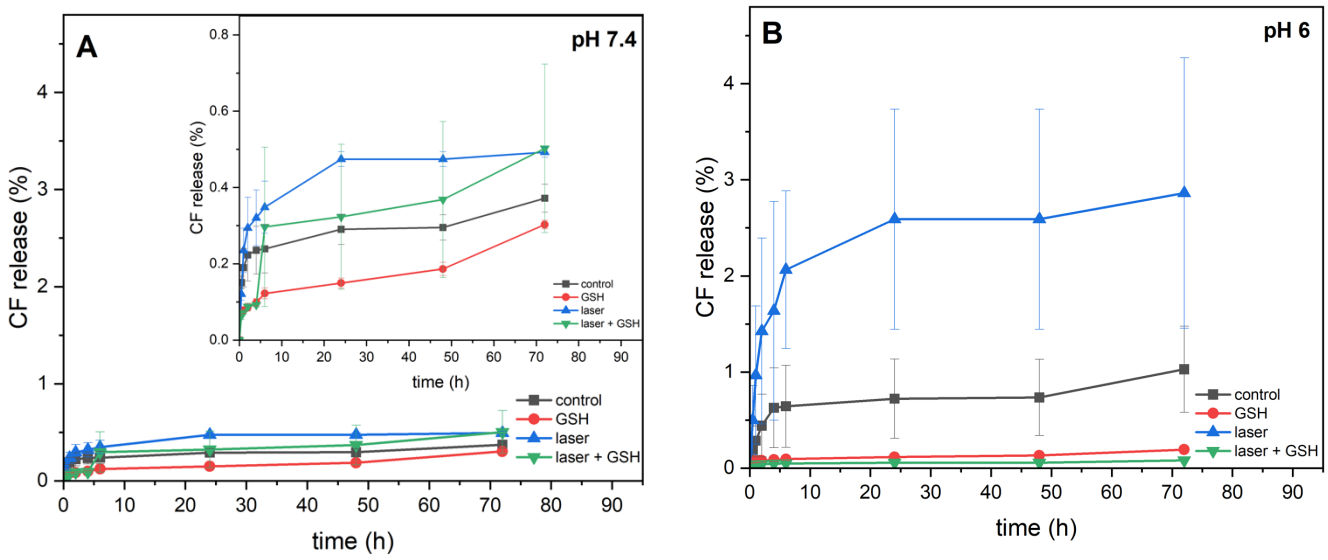


Figure 29. *In vitro* release profiles of CF from the plasmonic nanogels, over 72 h, at pH 7.4 (A) and 6 (B) at different conditions (10 mM GSH and 808 nm laser irradiation). The assays were performed at room temperature and in triplicate.

Furthermore, the release of drugs from the mesopores of the silica layer of the plasmonic nanoparticles was also evaluated to infer if a sequential release could be achieved. CF was encapsulated inside the pores, by incubation overnight in acetone. CF is a molecule composed of four planar rings and has one hydroxyl and two carboxyl groups. The release profile of CF from the silica layer was obtained by measuring the released content by fluorescence spectroscopy. The encapsulation efficiency of CF in the plasmonic particles was around 46% ± 11%, lower than the MTX's, which can be due to the large size of the molecule, and the encapsulation being into small pores.

The results of the release assay are represented in figure 29. According to the figure, the nanogel doesn't exhibit a initial burst release. This indicates that the lipid bilayer and the nanogel are acting as a barrier to the release of the content inside the mesopores of the silica layer coating the AuNRs, preventing the initial burst release, unwanted leaking, and possible toxic effects in healthy tissues. In general, the total CF released was very low, reaching a maximum release of 3% of the initial content, at pH 6, upon NIR irradiation, after 72 hours of assay. Furthermore, it can be inferred that at pH 7.4, there was no release of CF from the plasmonic particles. The release profile of CF indicates that the lipid bilayer and the nanogel act as a gatekeeper, preventing the leakage and the initial burst of the cargo. Besides, it suggests that the release can be triggered by NIR irradiation, as it causes a local increase of the temperature due to photothermal conversion of the AuNRs, inducing a phase transition of the lipid gate, achieving a slow and stimulli-controlled release.

The CF's release profile is a model release to simulate the 2DG's release profile, as it couldn't be quantified. This way, it can be inferred that 2DG will probably have a higher release under slightly acidic pH and upon NIR laser irradiation.

The results of the release assays present two different release profiles, suggesting that the nanosystem is capable of achieving a sequential release of the cargo, with a rapid release from the drug encapsulated in the nanogels network, enhanced by acidic pH and the presence of GSH; and a slower release from the cargo entraped in the plasmonic particles, triggered by NIR laser irradiation. Therefore the developed system shows great potential for controlled intratumoral delivery.

3.3. *In vitro* assays

3.3.1. Cytotoxicity assays

The cytotoxic effects of the developed nanosystem were assessed by performing a resazurin assay in a normal cell line L929 (fibroblastic cell line), which was selected according to the guidelines of ISO 10993-5 for biocompatibility evaluation, and a tumor cell line MDA-MB-231 (highly aggressive triple negative breast cancer cell line).The resazurin assay is a simple and rapid method to evaluate the metabolic activity of the cells and therefore infer about their viability. Resazurin is internalized by the cells and metabolized by enzymes, resulting in a pink, fluorescent molecule that can be quantified.

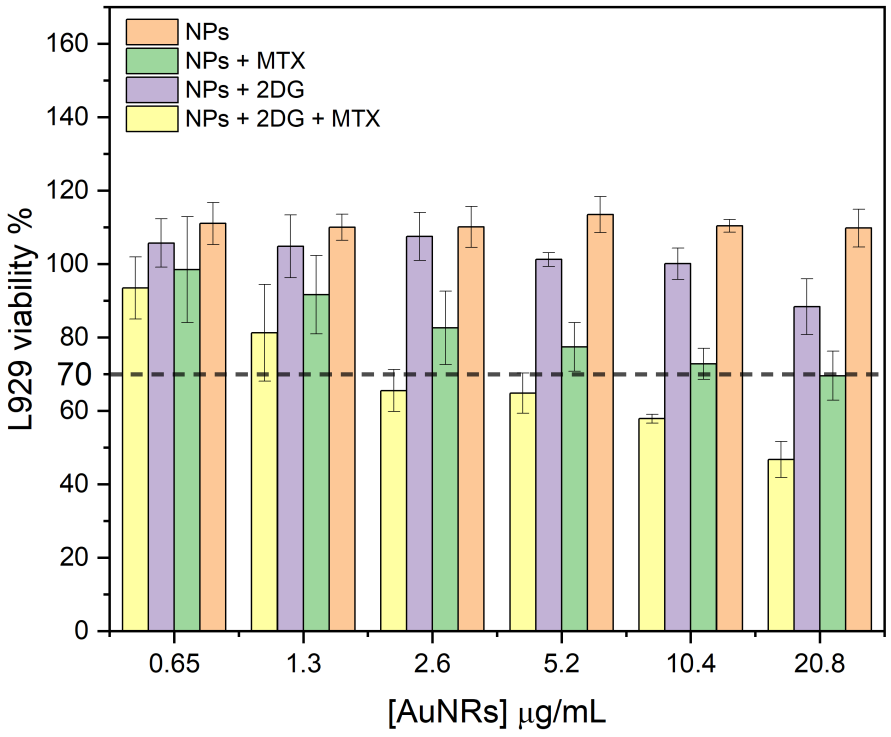


Figure 30. Evaluation of the metabolic activity of L929, determined by the resazurin assay. The cells were treated with different concentrations of the unloaded and loaded system with MTX; 2DG and 2DG+ MTX. The assays were performed in triplicate.

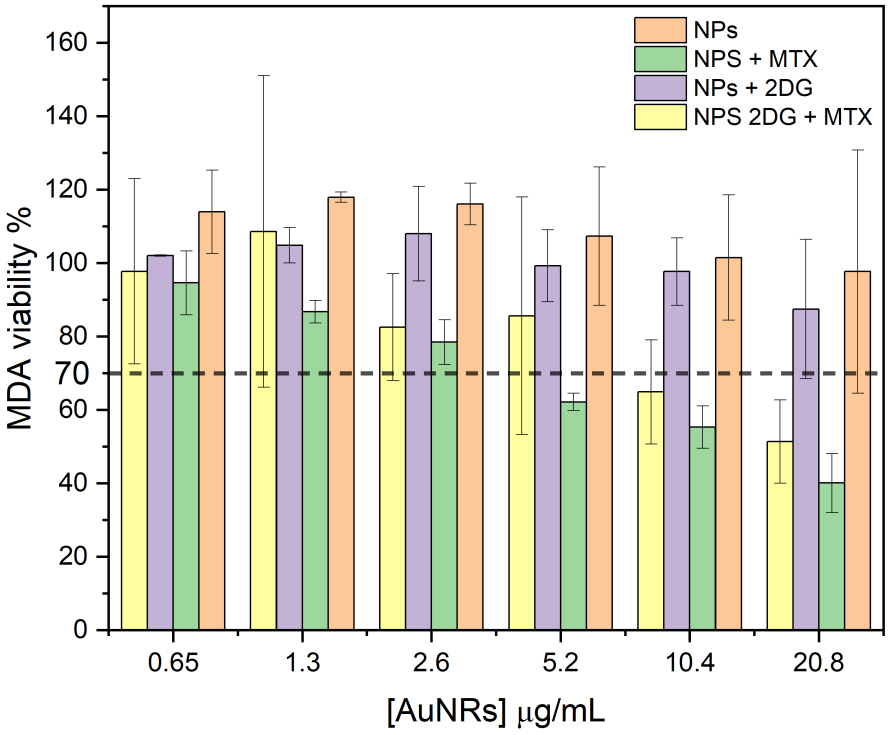


Figure 31. Evaluation of the metabolic activity of MDA-MB-231, determined by the resazurin assay. The cells were treated with different concentrations of the unloaded and loaded system with MTX; 2DG and 2DG+ MTX. The assays were performed in triplicate.

In this assay, cells were incubated with the unloaded and loaded system at concentrations between 0.65–20.8 μg/mL of AuNRs. The viability is expressed in percentage and is represented in figure 30, for L929, and in figure 31 for MDA-MB-231. The results show that the unloaded system did not cause any cytotoxic effect, even at the highest concentration tested, 20.8 μg/mL, being close to 100% in both cell lines. In addition, the nanogel loaded with 2DG didn't present significant cytotoxic effects, in L929 and MDA-MB-231, reaching 88% ± 8% and 87% ± 19% of cell viability, respectively. This reduced toxicity of the system containing 2DG indicates that the drug release might be low, as no laser irradiation is being applied or it doesn't cause any cytotoxic effect alone. By the analysis of CF's release profile (Figure 29), discussed in the previous section, it can be inferred that the release of 2DG is probably very low, not being enough to have a significant effect on the cells. On the other hand, the loaded system (with only MTX and with both drugs – MTX + 2DG) led to a dose-dependent decrease of the cell viability. In these cases, at 1.3 μg/mL and lower, there were no significant toxic effects, as the cell viability was higher than 70% in L929 cells (according to ISO 10993-5). This suggests that those concentrations can be used for complementary studies, such as cellular uptake and a future evaluation of the effect of laser irradiation in the cell viability. The highest toxicity in L929 was observed when the cells were incubated with the system loaded with both active agents, causing a decrease of around 50% of the cell viability

(Figure 30). On the other hand, in MDA-MB-231 cells, the system loaded with MTX was more cytotoxic to the cells than the combination of the drugs, resulting in a cellular viability of 40%, in the highest concentration used (Figure 31).

The *in vitro* results, indicate that the developed unloaded nanosystem did not cause cytotoxic effects, in the concentrations evaluated, in both L929 and MDA-MB-231 cell lines, and that any toxicity observed can be attributed to the encapsulated drugs.

3.3.2. Cellular uptake

The cellular uptake of the developed nanosystem was observed in MDA-MB-231 cells, using confocal microscopy. As MTX has fluorescence properties, it was used as a probe to identify the localization of the system and evaluate its uptake. The internalization was observed at two different time points, 1 hour and 3 hours from the moment the nanogel was added to the cells. A negative control, with untreated MDA-MB-231 cells was used. The nucleus of the cells was stained with Hoechst 33342® .

The images (Figure 32) show a time-dependent cellular uptake. It is noticeable that after 3 hours of incubation, a significant amount of fluorescence can be observed inside the cells, comparing with the control. This indicates that the fluorescence found is attributed to the emission of MTX, which demonstrated that the nanosystem was efficiently delivered to breast cancer cells. Furthermore, the images indicate that, after 1 hour of incubation, the nanogel could also be internalized and deliver a significant amount of MTX to these cells, highlighting the potential of this nanosystem for drug delivery in cancer therapeutics.

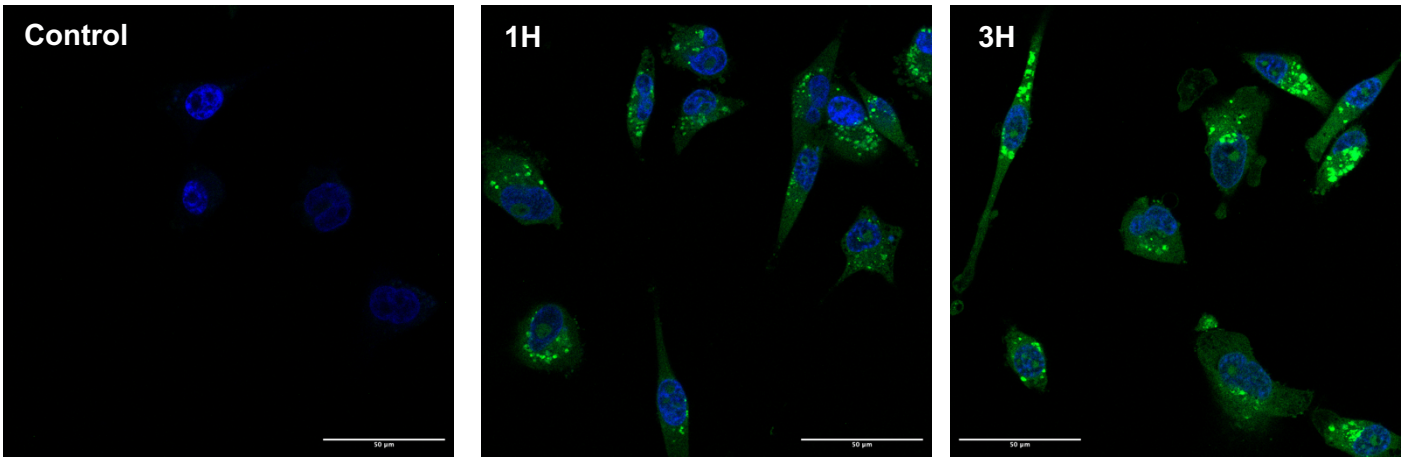


Figure 32. MDA-MB-231 cellular uptake of 2DG + MTX loaded nanogels after 1 hour and 3 hours of incubation visualized by confocal microscopy. The scale bar corresponds to 50 µm.

4. Conclusions

In this work, a novel plasmonic nanogel was developed, optimized, characterized and explored as a potential intracellular drug delivery system for combined cancer chemo/phototherapy.

Considering the general characteristics of the intracellular tumor environments, such as slightly acidic pH and high concentrations of GSH, a pH and GSH-sensitive nanogel formulation was developed, through the modification of chitosan with cysteine, and the gelation with alginate. This modification led to the formation of a network held by electrostatic interactions and disulfide bonds, which are sensitive to pH and GSH levels. The nanogel's responsivity to those stimuli was assessed and confirmed with DLS measurements.

Plasmonic nanoparticles were developed by covering AuNRs with a mesoporous silica layer and then with a lipid membrane. The plasmonic nanoparticles allowed to add an additional stimuli response to the nanosystem, to achieve a sequential release and to proportionate a combined therapy, as they can be used as photothermal agents.

The plasmonic nanogels were evaluated for the release of MTX and 2DG, and the release profiles (of MTX and CF) showed that a sequential and stimuli-controlled release could be achieved. The presence of GSH and the acidic pH promoted the release of the nanogel's content. Laser irradiation, which leads to photothermal conversion of the AuNRs, increased the release of the encapsulated cargo.

The developed system's cytotoxicity as assessed in L929 and MDA-MB-231 cell lines and presented no significant cytotoxic effects, when unloaded. The loaded system caused the decrease of the cell viability at higher concentrations in a dose-dependent manner. A more pronounced effect was observed with the combination of both drugs in L929, leading to a reduction of around 50% of the viability. On the other hand, the system loaded with MTX, presented more cytotoxicity in MDA-MB-231, leading to a cell viability of 40%. The cellular uptake was also evaluated, in MDA-MB-231 cell lines, and the results indicate that the particles are effectively internalized after 1 hour of incubation.

The plasmonic nanogels developed in this work, due to their physicochemical properties and *in vitro* behavior, hold great potential for biomedical applications in combined chemo-phototherapy of cancer.

5. Future perspectives

Considering the initially proposed work plan, reflected in the title of the thesis, the combination of photothermal therapy (PTT) with photodynamic therapy (PDT) and chemotherapy could be assessed by incorporating a photosensitizer, such as a porphyrin, and/or by evaluating the intrinsic photodynamic capacity of the particles themselves.

The use of materials like metal-organic frameworks (MOFs) could be an innovative strategy to enhance the encapsulation efficiency, as an alternative to the mesoporous silica layer. On the other hand, the MOFs could be tested as photodynamic agents.

Another important aspect to be evaluated is the effect of different phospholipid formulations in the lipid bilayer, to understand their influence on encapsulation efficiency, phase transition behavior, release profiles and interaction with the other components of the system.

Despite the promising results obtained, it would be interesting to use a different polymer in the nanogel formulation, such as a synthetic polymer and determine whether the physicochemical properties of the nanogel and/or its drug encapsulation efficiency could be improved. On the other hand, other modifications, with other functional groups, can be performed in the nanogel's polymers, besides the conjugation with a thiol-bearing molecule, to improve the mechanical properties or the stimuli-response of the nanogel.

Gold nanorods presented positive results as photothermal agents, however, their synthesis is hardly scalable, limiting their commercialization. So, exploring alternatives to replace the gold nanoparticles, such as silver nanoprisms, could facilitate the scalability and commercialization of the system.

The use of alternating layers of chitosan and alginate could also be tested to evaluate their impact on particle internalization and encapsulation efficiency. The use of multiple layers of the polymers can also be assessed to improve the release profiles of the encapsulated cargo, to prevent the initial unwanted burst release.

The release profiles of the different drugs showed that a sequential and stimuli-controlled release could be achieved. The release profile of 2DG can be obtained through HPLC or mass spectrometry, to verify and confirm its laser-triggered release. On the other hand, the encapsulation of other therapeutic molecules can also be evaluated, to assess the possibility of the application of the system in treatments for different pathologies.

Regarding laser irradiation, its effect on cell death can be tested in 2D cell models, to evaluate the effect of the combination of photothermia and chemotherapy, and the combination of the action of 2DG and mitoxantrone, in tumor cell death. To better mimic the tumor microenvironment, the effect of laser irradiation can also be evaluated in 3D models, as they can reproduce the cellular heterogeneity of the tumors. These experiments can be complemented by computational simulations to predict local temperature distribution and its biological effects, thus confirming effective cell death induction.

Other *in vitro* studies can be performed to assess the hemocompatibility of the system, investigate the cellular metabolism following particle internalization, and evaluate the potential carcinogenicity of the nanosystem. Understanding the interactions between particles and cells, particularly at the cell membrane level, is also crucial to understand the internalization mechanism, for example. Evaluating particle stability in biological fluids and their release profiles in the presence of enzymes is important to understand the release at physiological conditions.

To determine the best administration route of the developed system, *in vivo* studies assessing local and intravenous administration can be conducted, including the evaluation of particle retention, biodistribution, half-life in circulation, and elimination pathways.

Finally, it would be of interest to explore the potential use of this system for treating other pathologies via oral administration, by assessing its absorption in the stomach and intestine.

6. References

[1] F. Bray *et al.*, 'Global cancer statistics 2022: GLOBOCAN estimates of incidence and mortality worldwide for 36 cancers in 185 countries', *CA Cancer J Clin*, vol. 74, no. 3, pp. 229–263, May 2024, doi: 10.3322/CAAC.21834.

[2] M. Futamura and K. Yoshida, 'Current status of AYA-generation breast cancer: trends worldwide and in Japan', *Int J Clin Oncol*, vol. 27, no. 1, pp. 16–24, Jan. 2022, doi: 10.1007/S10147-021-02087-4/FIGURES/3.

[3] R. Kaur, A. Bhardwaj, and S. Gupta, 'Cancer treatment therapies: traditional to modern approaches to combat cancers', *Molecular Biology Reports 2023 50:11*, vol. 50, no. 11, pp. 9663–9676, Oct. 2023, doi: 10.1007/S11033-023-08809-3.

[4] S. Gao, X. Yang, J. Xu, N. Qiu, and G. Zhai, 'Nanotechnology for Boosting Cancer Immunotherapy and Remodeling Tumor Microenvironment: The Horizons in Cancer Treatment', *ACS Nano*, vol. 15, no. 8, pp. 12567–12603, Aug. 2021, doi: 10.1021/ACSNANO.1C02103/ASSET/IMAGES/LARGE/NN1C02103_0009.JPEG.

[5] M. Chehelgerdi *et al.*, 'Progressing nanotechnology to improve targeted cancer treatment: overcoming hurdles in its clinical implementation', *Mol Cancer*, vol. 22, no. 1, pp. 1–103, Dec. 2023, doi: 10.1186/S12943-023-01865-0/TABLES/15.

[6] J. A. Kemp and Y. J. Kwon, 'Cancer nanotechnology: current status and perspectives', *Nano Convergence 2021 8:1*, vol. 8, no. 1, pp. 1–38, Nov. 2021, doi: 10.1186/S40580-021-00282-7.

[7] L. Cheng, C. Wang, L. Feng, K. Yang, and Z. Liu, 'Functional nanomaterials for phototherapies of cancer', Nov. 12, 2014, *American Chemical Society*. doi: 10.1021/cr400532z.

[8] V. Molahalli, A. Shetty, A. Sharma, K. Bijapur, G. Soman, and G. Hegde, 'Risks and ethics of nanotechnology: an overview',

Nanoparticles and Plant-Microbe Interactions: An Environmental Perspective, pp. 35–68, Jan. 2023, doi: 10.1016/B978-0-323-90619-7.00014-X.

[9] X. Ma *et al.*, 'Nanotechnology in healthcare, and its safety and environmental risks', *Journal of Nanobiotechnology 2024 22:1*, vol. 22, no. 1, pp. 1–81, Nov. 2024, doi: 10.1186/S12951-024-02901-X.

[10] K. Akiyoshi, S. Deguchi, N. Moriguchi, S. Yamaguchi, and J. Sunamoto', 'Self-Aggregates of Hydrophobized Polysaccharides in Water. Formation and Characteristics of Nanoparticles', 1993.

[11] M. Ghomi *et al.*, 'A multifunctional bioresponsive and fluorescent active nanogel composite for breast cancer therapy and bioimaging', *Adv Compos Hybrid Mater*, vol. 6, no. 1, pp. 1–18, Feb. 2023, doi: 10.1007/S42114-022-00613-0/FIGURES/10.

[12] S. Zhang, J. Hao, F. Ding, and X. Ren, 'Nanocatalyst doped bacterial cellulose-based thermosensitive nanogel with biocatalytic function for antibacterial application', *Int J Biol Macromol*, vol. 195, pp. 294–301, Jan. 2022, doi: 10.1016/J.IJBIOMAC.2021.12.020.

[13] A. I. Robby, S. Jiang, E. J. Jin, and S. Y. Park, 'Coenzyme-A-Responsive Nanogel-Coated Electrochemical Sensor for Osteoarthritis-Detection-Based Genetic Models', *Gels*, vol. 10, no. 7, p. 451, Jul. 2024, doi: 10.3390/GELS10070451/S1.

[14] S. K. Lee *et al.*, 'Method for the Rapid Detection of SARS-CoV-2-Neutralizing Antibodies Using a Nanogel-Based Surface Plasmon Resonance Biosensor', *ACS Appl Polym Mater*, vol. 5, no. 3, pp. 2195–2202, Mar. 2023, doi: 10.1021/ACSAPM.2C02187/SUPPL_FILE/AP2C02187_SI_001.PDF.

[15] N. Morimoto, T. Endo, M. Ohtomi, Y. Iwasaki, and K. Akiyoshi, 'Hybrid nanogels with physical and chemical cross-linking structures as nanocarriers', *Macromol Biosci*, vol. 5, no. 8, pp. 710–716, Aug. 2005, doi: 10.1002/mabi.200500051.

[16] M. Ikeda-Imafuku, L. L. W. Wang, D. Rodrigues, S. Shaha, Z. Zhao, and S. Mitragotri, 'Strategies to improve the EPR effect: A mechanistic perspective and clinical translation', *Journal of Controlled Release*, vol. 345, pp. 512–536, May 2022, doi: 10.1016/J.JCONREL.2022.03.043.

[17] V. R. Shinde, N. Revi, S. Murugappan, S. P. Singh, and A. K. Rengan, 'Enhanced permeability and retention effect: A key facilitator for solid tumor targeting by nanoparticles', *Photodiagnosis Photodyn Ther*, vol. 39, p. 102915, Sep. 2022, doi: 10.1016/J.PDPDT.2022.102915.

[18] H. X. Wang *et al.*, 'Surface charge critically affects tumor penetration and therapeutic efficacy of cancer nanomedicines', *Nano Today*, vol. 11, no. 2, pp. 133–144, Apr. 2016, doi: 10.1016/J.NANTOD.2016.04.008.

[19] H. Zhang, Y. Zhai, J. Wang, and G. Zhai, 'New progress and prospects: The application of nanogel in drug delivery', Mar. 01, 2016, *Elsevier Ltd*. doi: 10.1016/j.msec.2015.11.041.

[20] I. González De Torre, L. Quintanilla, G. Pinedo-Martín, M. Alonso, and J. C. Rodríguez-Cabello, 'Nanogel formation from dilute solutions of clickable elastin-like recombinamers and its dependence on temperature: Two fractal gelation modes', *ACS Appl Mater Interfaces*, vol. 6, no. 16, pp. 14509–14515, Aug. 2014, doi: 10.1021/am503651y.

[21] A. V Kabanov, S. V Vinogradov, A. V Kabanov, and S. V Vinogradov, 'Nanogels as Pharmaceutical Carriers: Finite Networks of Infinite Capabilities', *Angewandte Chemie International Edition*, vol. 48, no. 30, pp. 5418–5429, Jul. 2009, doi: 10.1002/ANIE.200900441.

[22] B. N. H. M. Neerooa *et al.*, 'Development of Polymer-Assisted Nanoparticles and Nanogels for Cancer Therapy: An Update', *Gels 2021, Vol. 7, Page 60*, vol. 7, no. 2, p. 60, May 2021, doi: 10.3390/GELS7020060.

[23] S. (Gabriel) Kou, L. M. Peters, and M. R. Mucalo, 'Chitosan: A review of sources and preparation methods', *Int J Biol Macromol*, vol. 169, pp. 85–94, Feb. 2021, doi: 10.1016/J.IJBIOMAC.2020.12.005.

[24] H. Wang, J. Qian, and F. Ding, 'Recent advances in engineered chitosan-based nanogels for biomedical applications', 2017, *Royal Society of Chemistry*. doi: 10.1039/c7tb01624g.

[25] A. Mustafa, M. A. Indiran, K. Ramalingam, E. Perumal, R. Shanmugham, and M. I. Karobari, 'Anticancer potential of thiocolchicoside and lauric acid loaded chitosan nanogel against oral cancer cell lines: a comprehensive study', *Scientific Reports 2024 14:1*, vol. 14, no. 1, pp. 1–18, Apr. 2024, doi: 10.1038/s41598-024-60046-1.

[26] S. Manivong *et al.*, 'Chitosan-Based Nanogels: Synthesis and Toxicity Profile for Drug Delivery to Articular Joints', *Nanomaterials*, vol. 12, no. 8, p. 1337, Apr. 2022, doi: 10.3390/NANO12081337/S1.

[27] S. Sreekumar, F. M. Goycoolea, B. M. Moerschbacher, and G. R. Rivera-Rodriguez, 'Parameters influencing the size of chitosan-TPP nano- and microparticles', *Sci Rep*, vol. 8, no. 1, Dec. 2018, doi: 10.1038/s41598-018-23064-4.

[28] F. G. de Carvalho *et al.*, 'Synthesis and characterization of TPP/chitosan nanoparticles: Colloidal mechanism of reaction and antifungal effect on C. albicans biofilm formation', *Materials Science and Engineering C*, vol. 104, Nov. 2019, doi: 10.1016/j.msec.2019.109885.

[29] T. Jiang, Y. Wang, Z. Yu, and L. Du, 'Synthesis, characterization of chitosan/tripolyphosphate nanoparticles loaded with 4-chloro-2-methylphenoxyacetate sodium salt and its herbicidal activity against Bidens pilosa L.', *Scientific Reports 2024 14:1*, vol. 14, no. 1, pp. 1–12, Aug. 2024, doi: 10.1038/s41598-024-69438-9.

[30] P. Calvo *et al.*, 'Novel Hydrophilic Chitosan-Polyethylene Oxide Nanoparticles as Protein Carriers'.

[31] Y. Huang and Y. Lapitsky, 'On the kinetics of chitosan/tripolyphosphate micro- and nanogel aggregation and their effects on particle polydispersity', *J Colloid Interface Sci*, vol. 486, pp. 27–37, Jan. 2017, doi: 10.1016/J.JCIS.2016.09.050.

[32] S. Karimifard *et al.*, 'PH-Responsive Chitosan-Adorned Niosome Nanocarriers for Co-Delivery of Drugs for Breast Cancer Therapy', *ACS Appl Nano Mater*, vol. 5, no. 7, pp. 8811–8825, Jul. 2022, doi: 10.1021/ACSANM.2C00861/ASSET/IMAGES/LARGE/AN2C00861_0010.JPEG.

[33] I. Aranaz *et al.*, 'Chitosan: An overview of its properties and applications', Oct. 01, 2021, *MDPI*. doi: 10.3390/polym13193256.

[34] K. Morikawa, Y. Masubuchi, Y. Shchipunov, and A. Zinchenko, 'DNA-Chitosan Hydrogels: Formation, Properties, and Functionalization with Catalytic Nanoparticles', *ACS Appl Bio Mater*, vol. 4, no. 2, pp. 1823–1832, Feb. 2021, doi: 10.1021/ACSABM.0C01533/ASSET/IMAGES/LARGE/MT0C01533_0007.JPEG.

[35] M. Swiontek Brzezinska *et al.*, 'Biodegradability Study of Modified Chitosan Films with Cinnamic Acid and Ellagic Acid in Soil', *Polymers (Basel)*, vol. 16, no. 5, p. 574, Mar. 2024, doi: 10.3390/POLYM16050574.

[36] X. Yan *et al.*, 'Modified Chitosan for Highly Efficient Non-Invasive Transdermal Delivery of Catalase to Repair and Prevent Skin Photodamages', *Adv Funct Mater*, vol. 34, no. 49, p. 2409416, Dec. 2024, doi: 10.1002/ADFM.202409416.

[37] M. E. S. Ahmed, M. I. Mohamed, H. Y. Ahmed, M. M. Elaasser, and N. G. Kandile, 'Fabrication and characterization of unique sustain modified chitosan nanoparticles for biomedical applications', *Scientific Reports 2024 14:1*, vol. 14, no. 1, pp. 1–18, Jun. 2024, doi: 10.1038/s41598-024-64017-4.

[38] S. G. Nanaki *et al.*, 'L-Cysteine Modified Chitosan Nanoparticles and Carbon-Based Nanostructures for the Intranasal Delivery of

Galantamine', *Polymers (Basel)*, vol. 14, no. 19, Oct. 2022, doi: 10.3390/polym14194004.

[39] D. Liu *et al.*, 'Potential advantages of a novel chitosan-N-acetylcysteine surface modified nanostructured lipid carrier on the performance of ophthalmic delivery of curcumin', *Sci Rep*, vol. 6, Jun. 2016, doi: 10.1038/srep28796.

[40] G. Lombardo *et al.*, 'Novel chitosan-based hydrogels as promising wound dressing materials with advanced properties', *Int J Biol Macromol*, vol. 279, Nov. 2024, doi: 10.1016/j.ijbiomac.2024.135423.

[41] B. Le-Vinh, C. Steinbring, N. M. Nguyen Le, B. Matuszczak, and A. Bernkop-Schnürch, 'S-Protected Thiolated Chitosan versus Thiolated Chitosan as Cell Adhesive Biomaterials for Tissue Engineering', *ACS Appl Mater Interfaces*, vol. 15, no. 34, pp. 40304–40316, Aug. 2023, doi: 10.1021/acsami.3c09337.

[42] D. George, P. U. Maheswari, and K. M. M. S. Begum, 'Cysteine conjugated chitosan based green nanohybrid hydrogel embedded with zinc oxide nanoparticles towards enhanced therapeutic potential of naringenin', *React Funct Polym*, vol. 148, Mar. 2020, doi: 10.1016/j.reactfunctpolym.2020.104480.

[43] Q. Min, R. Tan, Y. Zhang, C. Wang, Y. Wan, and J. Li, 'Multi-Crosslinked Strong and Elastic Bioglass/Chitosan-Cysteine Hydrogels with Controlled Quercetin Delivery for Bone Tissue Engineering', *Pharmaceutics*, vol. 2022, p. 2048, 2022, doi: 10.3390/pharmaceutics.

[44] D. Liu *et al.*, 'Potential advantages of a novel chitosan-N-acetylcysteine surface modified nanostructured lipid carrier on the performance of ophthalmic delivery of curcumin', *Scientific Reports 2016 6:1*, vol. 6, no. 1, pp. 1–14, Jun. 2016, doi: 10.1038/srep28796.

[45] R. Kumari, S. S. Narvi, and P. K. Dutta, 'Thiol modified chitosan-silica nanohybrid for antibacterial, antioxidant and drug delivery

application', *Journal of the Indian Chemical Society*, vol. 98, no. 8, p. 100108, Aug. 2021, doi: 10.1016/J.JICS.2021.100108.

[46] Z. G. Yue *et al.*, 'Surface charge affects cellular uptake and intracellular trafficking of chitosan-based nanoparticles', *Biomacromolecules*, vol. 12, no. 7, pp. 2440–2446, Jul. 2011, doi: 10.1021/BM101482R/SUPPL_FILE/BM101482R_SI_001.PDF.

[47] M. S. P. Boyles *et al.*, 'Chitosan functionalisation of gold nanoparticles encourages particle uptake and induces cytotoxicity and pro-inflammatory conditions in phagocytic cells, as well as enhancing particle interactions with serum components', *J Nanobiotechnology*, vol. 13, no. 1, pp. 1–20, Nov. 2015, doi: 10.1186/S12951-015-0146-9/FIGURES/2.

[48] P. Pereira *et al.*, 'SiRNA inhibition of endocytic pathways to characterize the cellular uptake mechanisms of folate-functionalized glycol chitosan nanogels', *Mol Pharm*, vol. 12, no. 6, pp. 1970–1979, Jun. 2015, doi: 10.1021/MP500785T/SUPPL_FILE/MP500785T_SI_001.PDF.

[49] M. A. Barkat *et al.*, 'Formulation development of methotrexate lipid-based nanogel for treatment of skin cancer', *Colloids Surf A Physicochem Eng Asp*, vol. 688, p. 133571, May 2024, doi: 10.1016/J.COLSURFA.2024.133571.

[50] M. M. Abo-ser, E. S. A. Toson, A. A. El-Bindary, G. Schlatter, and K. R. Shoueir, 'Smart chitosan nanogel for targeted doxorubicin delivery, ensuring precise release, and minimizing side effects in Ehrlich ascites carcinoma-bearing mice', *Int J Biol Macromol*, vol. 267, p. 131390, May 2024, doi: 10.1016/J.IJBIOMAC.2024.131390.

[51] M. M. Ahmed, M. S. M. Ameen, M. Abazari, S. M. Badeleh, K. Rostamizadeh, and S. S. Mohammed, 'Chitosan-decorated and tripolyphosphate-crosslinked pH-sensitive niosomal nanogels for Controlled release of fluoropyrimidine 5-fluorouracil', *Biomedicine & Pharmacotherapy*, vol. 164, p. 114943, Aug. 2023, doi: 10.1016/J.BIOPHA.2023.114943.

[52] T. Li *et al.*, 'Intra-articular injection of anti-inflammatory peptide-loaded glycol chitosan/fucoidan nanogels to inhibit inflammation and attenuate osteoarthritis progression', *Int J Biol Macromol*, vol. 170, pp. 469–478, Feb. 2021, doi: 10.1016/J.IJBIOMAC.2020.12.158.

[53] H. Wang, J. Qian, and F. Ding, 'Recent advances in engineered chitosan-based nanogels for biomedical applications', *J Mater Chem B*, vol. 5, no. 34, pp. 6986–7007, Aug. 2017, doi: 10.1039/C7TB01624G.

[54] J. P. Paques, E. Van Der Linden, C. J. M. Van Rijn, and L. M. C. Sagis, 'Preparation methods of alginate nanoparticles', *Adv Colloid Interface Sci*, vol. 209, pp. 163–171, Jul. 2014, doi: 10.1016/J.CIS.2014.03.009.

[55] S. N. Pawar, 'Chemical Modification of Alginate', *Seaweed Polysaccharides: Isolation, Biological and Biomedical Applications*, pp. 111–155, Jan. 2017, doi: 10.1016/B978-0-12-809816-5.00008-6.

[56] J. Sun and H. Tan, 'Alginate-Based Biomaterials for Regenerative Medicine Applications', *Materials 2013, Vol. 6, Pages 1285-1309*, vol. 6, no. 4, pp. 1285–1309, Mar. 2013, doi: 10.3390/MA6041285.

[57] G. T. Grant, E. R. Morris, D. A. Rees, P. J. C. Smith, and D. Thom, 'Biological interactions between polysaccharides and divalent cations: The egg-box model', *FEBS Lett*, vol. 32, no. 1, pp. 195–198, May 1973, doi: 10.1016/0014-5793(73)80770-7.

[58] A. Shilpa, S. S. Agrawal, and A. R. Ray, 'Controlled Delivery of Drugs from Alginate Matrix', *Journal of Macromolecular Science, Part C: Polymer Reviews*, vol. 43, no. 2, pp. 187–221, May 2003, doi: 10.1081/MC-120020160.

[59] K. Y. Lee and D. J. Mooney, 'Alginate: Properties and biomedical applications', *Prog Polym Sci*, vol. 37, no. 1, pp. 106–126, Jan. 2012, doi: 10.1016/J.PROGPOLYMSCI.2011.06.003.

[60] J. Tan *et al.*, 'Development of alginate-based hydrogels: Crosslinking strategies and biomedical applications', *Int J Biol Macromol*, vol. 239, p. 124275, Jun. 2023, doi: 10.1016/J.IJBIOMAC.2023.124275.

[61] J. R. Choi, K. W. Yong, J. Y. Choi, and A. C. Cowie, 'Recent advances in photo-crosslinkable hydrogels for biomedical applications', *Biotechniques*, vol. 66, no. 1, pp. 40–53, Jan. 2019, doi: 10.2144/BTN-2018-0083/ASSET/D81BFD99-6F37-423C-98FB-12096D753084/ASSETS/GRAPHIC/IBTN_A_12360580_F0003.JPG.

[62] M. Ghaffarlou *et al.*, 'Photothermal and radiotherapy with alginate-coated gold nanoparticles for breast cancer treatment', *Scientific Reports 2024 14:1*, vol. 14, no. 1, pp. 1–12, Jun. 2024, doi: 10.1038/s41598-024-60396-w.

[63] R. Eivazzadeh-Keihan *et al.*, 'Fabrication of a magnetic alginate-silk fibroin hydrogel, containing halloysite nanotubes as a novel nanocomposite for biological and hyperthermia applications', *Scientific Reports 2022 12:1*, vol. 12, no. 1, pp. 1–13, Sep. 2022, doi: 10.1038/s41598-022-19511-y.

[64] F. Radinekiyan *et al.*, 'A magnetic cross-linked alginate-biobased nanocomposite with anticancer and hyperthermia activities', *Carbohydrate Polymer Technologies and Applications*, vol. 7, p. 100481, Jun. 2024, doi: 10.1016/J.CARPTA.2024.100481.

[65] A. G. Niculescu and A. M. Grumezescu, 'Applications of Chitosan-Alginate-Based Nanoparticles—An Up-to-Date Review', *Nanomaterials 2022, Vol. 12, Page 186*, vol. 12, no. 2, p. 186, Jan. 2022, doi: 10.3390/NANO12020186.

[66] S. Asadi *et al.*, 'Aerosol assisted synthesis of a pH responsive curcumin anticancer drug nanocarrier using chitosan and alginate natural polymers', *Scientific Reports 2023 13:1*, vol. 13, no. 1, pp. 1–10, Nov. 2023, doi: 10.1038/s41598-023-46904-4.

[67] P. Patra, T. K. Upadhyay, N. Alshammari, M. Saeed, and K. K. Kesari, 'Alginate-Chitosan Biodegradable and Biocompatible Based Hydrogel for Breast Cancer Immunotherapy and Diagnosis: A Comprehensive Review', *ACS Appl Bio Mater*, vol. 7, no. 6, p. 3515, Jun. 2024, doi: 10.1021/ACSABM.3C00984.

[68] Y. Luo and Q. Wang, 'Recent development of chitosan-based polyelectrolyte complexes with natural polysaccharides for drug delivery', *Int J Biol Macromol*, vol. 64, pp. 353–367, Mar. 2014, doi: 10.1016/J.IJBIOMAC.2013.12.017.

[69] T. W. Wong, L. W. Chan, S. Bin Kho, and P. W. Sia Heng, 'Design of controlled-release solid dosage forms of alginate and chitosan using microwave', *Journal of Controlled Release*, vol. 84, no. 3, pp. 99–114, Dec. 2002, doi: 10.1016/S0168-3659(02)00237-7.

[70] J. H. Hamman, 'Chitosan Based Polyelectrolyte Complexes as Potential Carrier Materials in Drug Delivery Systems', *Marine Drugs 2010, Vol. 8, Pages 1305-1322*, vol. 8, no. 4, pp. 1305–1322, Apr. 2010, doi: 10.3390/MD8041305.

[71] H. V. Sæther, H. K. Holme, G. Maurstad, O. Smidsrød, and B. T. Stokke, 'Polyelectrolyte complex formation using alginate and chitosan', *Carbohydr Polym*, vol. 74, no. 4, pp. 813–821, Nov. 2008, doi: 10.1016/J.CARBPOL.2008.04.048.

[72] '(PDF) Ionotropic gelation and polyelectrolyte complexation: The novel techniques to design hydrogel particulate sustained, modulated drug delivery system: A review'. Accessed: Jan. 14, 2025. [Online]. Available: https://www.researchgate.net/publication/265991547_Ionotropic_gelation_and_polyelectrolyte_complexation_The_novel_techniques_to_design_hydrogel_particulate_sustained_modulated_drug_delivery_system_A_review#fullTextFileContent

[73] M. Gierszewska, J. Ostrowska-Czubenko, and E. Chrzanowska, 'pH-responsive chitosan/alginate polyelectrolyte complex

membranes reinforced by tripolyphosphate', *Eur Polym J*, vol. 101, pp. 282–290, Apr. 2018, doi: 10.1016/J.EURPOLYMJ.2018.02.031.

[74] L. Segale, L. Giovannelli, P. Mannina, and F. Pattarino, 'Calcium Alginate and Calcium Alginate-Chitosan Beads Containing Celecoxib Solubilized in a Self-Emulsifying Phase', *Scientifica (Cairo)*, vol. 2016, 2016, doi: 10.1155/2016/5062706.

[75] F. Costa-e-Sá, M. Comís-Tuche, C. Spuch, E. M. S. Castanheira, and S. R. S. Veloso, 'Sequential release of drugs from dual-delivery plasmonic nanogels containing lipid-gated mesoporous silica-coated gold nanorods', *J Drug Deliv Sci Technol*, vol. 96, p. 105723, Jun. 2024, doi: 10.1016/J.JDDST.2024.105723.

[76] S. R. S. Veloso *et al.*, 'Chitosan/Alginate Nanogels Containing Multicore Magnetic Nanoparticles for Delivery of Doxorubicin', *Pharmaceutics*, vol. 15, no. 9, p. 2194, Sep. 2023, doi: 10.3390/PHARMACEUTICS15092194/S1.

[77] D. Yadav, J. Dutta, M. Shabani, and J. Dutta dutta, 'A systematic review on recent development of chitosan/alginate-based polyelectrolyte complexes for wastewater treatment', *International Journal of Environmental Science and Technology 2023 21:3*, vol. 21, no. 3, pp. 3381–3406, Oct. 2023, doi: 10.1007/S13762-023-05244-6.

[78] S. Li *et al.*, 'Application of chitosan/alginate nanoparticle in oral drug delivery systems: prospects and challenges', *Drug Deliv*, vol. 29, no. 1, pp. 1142–1149, Dec. 2022, doi: 10.1080/10717544.2022.2058646.

[79] P. Patra, T. K. Upadhyay, N. Alshammari, M. Saeed, and K. K. Kesari, 'Alginate-Chitosan Biodegradable and Biocompatible Based Hydrogel for Breast Cancer Immunotherapy and Diagnosis: A Comprehensive Review', *ACS Appl Bio Mater*, vol. 7, no. 6, pp. 3515–3534, Jun. 2024, doi: 10.1021/ACSABM.3C00984/ASSET/IMAGES/LARGE/MT3C00984_0003.JPEG.

[80] N. Wathoni, Y. Herdiana, C. Suhandi, A. F. A. Mohammed, A. El-Rayyes, and A. C. Narsa, 'Chitosan/Alginate-Based Nanoparticles for Antibacterial Agents Delivery', *Int J Nanomedicine*, vol. 19, pp. 5021–5044, 2024, doi: 10.2147/IJN.S469572.

[81] M. Hesan, A. Gholipour-Kanani, M. Lotfi, and M. Shafiee, 'The synthesis and characterization of core-shell nanogels based on alginate and chitosan for the controlled delivery of mupirocin', *Biochem Eng J*, vol. 190, p. 108742, Jan. 2023, doi: 10.1016/J.BEJ.2022.108742.

[82] L. Kong, F. Campbell, and A. Kros, 'DePEGylation strategies to increase cancer nanomedicine efficacy', *Nanoscale Horiz*, vol. 4, no. 2, pp. 378–387, Feb. 2019, doi: 10.1039/C8NH00417J.

[83] Z. Z. Huang *et al.*, 'Mechanism and significance of increased glutathione level in human hepatocellular carcinoma and liver regeneration', *The FASEB Journal*, vol. 15, no. 1, pp. 19–21, Jan. 2001, doi: 10.1096/FJ.00-0445FJE.

[84] M. Jin, S. Li, Y. Wu, D. Li, and Y. Han, 'Construction of Chitosan/Alginate Nano-Drug Delivery System for Improving Dextran Sodium Sulfate-Induced Colitis in Mice', *Nanomaterials 2021, Vol. 11, Page 1884*, vol. 11, no. 8, p. 1884, Jul. 2021, doi: 10.3390/NANO11081884.

[85] J. Yoo and Y. Y. Won, 'Phenomenology of the Initial Burst Release of Drugs from PLGA Microparticles', *ACS Biomater Sci Eng*, vol. 6, no. 11, pp. 6053–6062, Nov. 2020, doi: 10.1021/ACSBIOMATERIALS.0C01228.

[86] J. Chen *et al.*, 'Poly(N-isopropylacrylamide) derived nanogels demonstrated thermosensitive self-assembly and GSH-triggered drug release for efficient tumor Therapy', *Polym Chem*, vol. 10, no. 29, pp. 4031–4041, Jul. 2019, doi: 10.1039/C9PY00537D.

[87] E. Pérez, A. M. Fernández-Olleros, R. Olmo, J. M. Teijón, and M. D. Blanco, 'pH and glutathion-responsive hydrogel for localized delivery

of paclitaxel', *Colloids Surf B Biointerfaces*, vol. 116, pp. 247–256, Apr. 2014, doi: 10.1016/J.COLSURFB.2014.01.004.

[88] K. McNamara and S. A. M. Tofail, 'Nanoparticles in biomedical applications', *Adv Phys X*, vol. 2, no. 1, pp. 54–88, 2017, doi: 10.1080/23746149.2016.1254570.

[89] C. Lang, E. G. Mission, A. A. H. Ahmad Fuaad, and M. Shaalan, 'Nanoparticle tools to improve and advance precision practices in the Agrifoods Sector towards sustainability - A review', *J Clean Prod*, vol. 293, p. 126063, Apr. 2021, doi: 10.1016/J.JCLEPRO.2021.126063.

[90] N. G. Semaltianos and G. Karczewski, 'Laser Synthesis of Magnetic Nanoparticles in Liquids and Application in the Fabrication of Polymer-Nanoparticle Composites', *ACS Appl Nano Mater*, vol. 4, no. 7, pp. 6407–6440, Jul. 2021, doi: 10.1021/ACSANM.1C00715/ASSET/IMAGES/LARGE/AN1C00715_0018.JPEG.

[91] A. C. Marques *et al.*, 'Bottom-up microwave-assisted seed-mediated synthesis of gold nanoparticles onto nanocellulose to boost stability and high performance for SERS applications', *Appl Surf Sci*, vol. 561, p. 150060, Sep. 2021, doi: 10.1016/J.APSUSC.2021.150060.

[92] N. Joudeh and D. Linke, 'Nanoparticle classification, physicochemical properties, characterization, and applications: a comprehensive review for biologists', *Journal of Nanobiotechnology 2022 20:1*, vol. 20, no. 1, pp. 1–29, Jun. 2022, doi: 10.1186/S12951-022-01477-8.

[93] M. Aftab, M. S. Mansha, T. Iqbal, and M. Farooq, 'Surface Plasmon Excitation: Theory, Configurations, and Applications', *Plasmonics*, vol. 19, no. 4, pp. 1701–1719, Aug. 2024, doi: 10.1007/S11468-023-02095-2/FIGURES/16.

[94] Y. Chen and H. Ming, 'Photonic Sensors Review Review of Surface Plasmon Resonance and Localized Surface Plasmon Resonance Sensor ', *Photonic Sensors*, vol. 2, no. 1, pp. 37–49, 2012, doi: 10.1007/s13320-011-0051-2.

[95] S. Unser, I. Bruzas, J. He, and L. Sagle, 'Localized Surface Plasmon Resonance Biosensing: Current Challenges and Approaches', *Sensors 2015, Vol. 15, Pages 15684-15716*, vol. 15, no. 7, pp. 15684–15716, Jul. 2015, doi: 10.3390/S150715684.

[96] F. Diehl, S. Hageneder, S. Fossati, S. K. Auer, J. Dostalek, and U. Jonas, 'Plasmonic nanomaterials with responsive polymer hydrogels for sensing and actuation', *This journal is Cite this: Chem. Soc. Rev*, vol. 3926, p. 3926, 2022, doi: 10.1039/d1cs01083b.

[97] G. Liu, M. Lu, X. Huang, T. Li, and D. Xu, 'Application of Gold-Nanoparticle Colorimetric Sensing to Rapid Food Safety Screening', doi: 10.3390/s18124166.

[98] X. Huang, S. Neretina, and M. A. El-Sayed, 'Gold Nanorods: From Synthesis and Properties to Biological and Biomedical Applications', *Advanced Materials*, vol. 21, no. 48, pp. 4880–4910, Dec. 2009, doi: 10.1002/ADMA.200802789.

[99] J. Li *et al.*, 'Near infrared photothermal conversion materials: mechanism, preparation, and photothermal cancer therapy applications', *J Mater Chem B*, vol. 9, no. 38, pp. 7909–7926, Oct. 2021, doi: 10.1039/D1TB01310F.

[100] P. K. Jain, X. Huang, I. H. El-Sayed, and M. A. El-Sayed, 'Noble metals on the nanoscale: Optical and photothermal properties and some applications in imaging, sensing, biology, and medicine', *Acc Chem Res*, vol. 41, no. 12, pp. 1578–1586, Dec. 2008, doi: 10.1021/AR7002804/ASSET/IMAGES/LARGE/AR-2007-002804_0005.JPEG.

[101] J. Li *et al.*, 'Near infrared photothermal conversion materials: mechanism, preparation, and photothermal cancer therapy applications', *J Mater Chem B*, vol. 9, no. 38, pp. 7909–7926, Oct. 2021, doi: 10.1039/D1TB01310F.

[102] M. L. Taylor, R. E. Wilson, K. D. Amrhein, and X. Huang, 'Gold Nanorod-Assisted Photothermal Therapy and Improvement

Strategies', *Bioengineering 2022, Vol. 9, Page 200*, vol. 9, no. 5, p. 200, May 2022, doi: 10.3390/BIOENGINEERING9050200.

[103] Y. Zhang *et al.*, 'Recent advances and clinical challenges of phototherapeutic nanoparticles in cancer monotherapy or combination therapy', *Coord Chem Rev*, vol. 518, p. 216069, Nov. 2024, doi: 10.1016/J.CCR.2024.216069.

[104] M. L. Taylor, R. E. Wilson, K. D. Amrhein, and X. Huang, 'Gold Nanorod-Assisted Photothermal Therapy and Improvement Strategies', *Bioengineering 2022, Vol. 9, Page 200*, vol. 9, no. 5, p. 200, May 2022, doi: 10.3390/BIOENGINEERING9050200.

[105] L. Tong, Y. Zhao, T. B. Huff, M. N. Hansen, A. Wei, and J. X. Cheng, 'Gold Nanorods Mediate Tumor Cell Death by Compromising Membrane Integrity', *Advanced Materials*, vol. 19, no. 20, pp. 3136–3141, Oct. 2007, doi: 10.1002/ADMA.200701974.

[106] A. S. Monem, N. Elbialy, and N. Mohamed, 'Mesoporous silica coated gold nanorods loaded doxorubicin for combined chemo–photothermal therapy', *Int J Pharm*, vol. 470, no. 1–2, pp. 1–7, Aug. 2014, doi: 10.1016/J.IJPHARM.2014.04.067.

[107] E. Hutter and J. H. Fendler, 'Exploitation of Localized Surface Plasmon Resonance', *Advanced Materials*, vol. 16, no. 19, pp. 1685–1706, Oct. 2004, doi: 10.1002/ADMA.200400271.

[108] M. Q. He, Y. Ai, W. Hu, L. Guan, M. Ding, and Q. Liang, 'Recent Advances of Seed-Mediated Growth of Metal Nanoparticles: from Growth to Applications', *Advanced Materials*, vol. 35, no. 46, p. 2211915, Nov. 2023, doi: 10.1002/ADMA.202211915.

[109] J. Lai *et al.*, 'One-pot synthesis of gold nanorods using binary surfactant systems with improved monodispersity, dimensional tunability and plasmon resonance scattering properties', *Nanotechnology*, vol. 25, no. 12, Mar. 2014, doi: 10.1088/0957-4484/25/12/125601.

[110] L. Roach, S. Ye, S. C. T. Moorcroft, K. Critchley, P. L. Coletta, and S. D. Evans, 'Morphological control of seedlessly-synthesized gold

nanorods using binary surfactants', *Nanotechnology*, vol. 29, no. 13, p. 135601, Feb. 2018, doi: 10.1088/1361-6528/AAA99D.

[111] L. Roach, P. L. Coletta, K. Critchley, and S. D. Evans, 'Controlling the Optical Properties of Gold Nanorods in One-Pot Syntheses', *Journal of Physical Chemistry C*, vol. 126, no. 6, pp. 3235–3243, Feb. 2022, doi: 10.1021/acs.jpcc.1c10447.

[112] R. Zou *et al.*, 'Thermal stability of gold nanorods in an aqueous solution', *Colloids Surf A Physicochem Eng Asp*, vol. 372, no. 1–3, pp. 177–181, Dec. 2010, doi: 10.1016/J.COLSURFA.2010.10.012.

[113] C. Wu and Q. H. Xu, 'Stable and functionable mesoporous silica-coated gold nanorods as sensitive localized surface plasmon resonance (LSPR) nanosensors', *Langmuir*, vol. 25, no. 16, pp. 9441–9446, Aug. 2009, doi: 10.1021/LA900646N/SUPPL_FILE/LA900646N_SI_001.PDF.

[114] Z. Zhao *et al.*, 'Thickness control of mesoporous silica coated on gold nanorod', *Journal of Nanoparticle Research*, vol. 23, no. 8, pp. 1–12, Aug. 2021, doi: 10.1007/S11051-021-05317-Y/FIGURES/10.

[115] Y.-S. Chen *et al.*, 'Enhanced thermal stability of silica-coated gold nanorods for photoacoustic imaging and image-guided therapy', *Optics Express, Vol. 18, Issue 9, pp. 8867-8878*, vol. 18, no. 9, pp. 8867–8878, Apr. 2010, doi: 10.1364/OE.18.008867.

[116] E. Gergely-Fülöp, D. Zámbó, and A. Deák, 'Thermal stability of mesoporous silica-coated gold nanorods with different aspect ratios', *Mater Chem Phys*, vol. 148, no. 3, pp. 909–913, Dec. 2014, doi: 10.1016/J.MATCHEMPHYS.2014.08.069.

[117] W. Stöber, A. Fink, and E. Bohn, 'Controlled growth of monodisperse silica spheres in the micron size range', *J Colloid Interface Sci*, vol. 26, no. 1, pp. 62–69, Jan. 1968, doi: 10.1016/0021-9797(68)90272-5.

[118] I. Gorelikov and N. Matsuura, 'Single-step coating of mesoporous silica on cetyltrimethyl ammonium bromide-capped nanoparticles', *Nano Lett*, vol. 8, no. 1, pp. 369–373, Jan. 2008, doi:

10.1021/NL0727415/SUPPL_FILE/NL0727415SI20071023_024724.PDF.

[119] B. Xu, S. Li, R. Shi, and H. Liu, 'Multifunctional mesoporous silica nanoparticles for biomedical applications', *Signal Transduction and Targeted Therapy 2023 8:1*, vol. 8, no. 1, pp. 1–28, Nov. 2023, doi: 10.1038/s41392-023-01654-7.

[120] M. J. Kim, D. H. Jung, C. Y. Lee, S. Hong, J. H. Heo, and J. H. Lee, 'Structurally Engineered Silica Shells on Gold Nanorods for Biomedical Applications', *Small Struct*, vol. 4, no. 9, p. 2300047, Sep. 2023, doi: 10.1002/SSTR.202300047.

[121] S. S. Park and C. S. Ha, 'Hollow Mesoporous Functional Hybrid Materials: Fascinating Platforms for Advanced Applications', *Adv Funct Mater*, vol. 28, no. 27, p. 1703814, Jul. 2018, doi: 10.1002/ADFM.201703814.

[122] B. Dumontel, V. Conejo-Rodríguez, M. Vallet-Regí, and M. Manzano, 'Natural Biopolymers as Smart Coating Materials of Mesoporous Silica Nanoparticles for Drug Delivery', *Pharmaceutics 2023, Vol. 15, Page 447*, vol. 15, no. 2, p. 447, Jan. 2023, doi: 10.3390/PHARMACEUTICS15020447.

[123] J. Wen, K. Yang, F. Liu, H. Li, Y. Xu, and S. Sun, 'Diverse gatekeepers for mesoporous silica nanoparticle based drug delivery systems', *Chem Soc Rev*, vol. 46, no. 19, pp. 6024–6045, Oct. 2017, doi: 10.1039/C7CS00219J.

[124] J. Yang *et al.*, 'Spatially confined fabrication of core-shell gold nanocages@Mesoporous silica for near-infrared controlled photothermal drug release', *Chemistry of Materials*, vol. 25, no. 15, pp. 3030–3037, Aug. 2013, doi: 10.1021/CM401115B/SUPPL_FILE/CM401115B_SI_001.PDF.

[125] Q. Lei *et al.*, 'Multifunctional Mesoporous Silica Nanoparticles with Thermal-Responsive Gatekeeper for NIR Light-Triggered Chemo/Photothermal-Therapy', *Small*, vol. 12, no. 31, pp. 4286–4298, Aug. 2016, doi: 10.1002/SMLL.201601137.

[126] L. Palanikumar, E. S. Choi, J. Y. Cheon, S. H. Joo, and J. H. Ryu, 'Noncovalent Polymer-Gatekeeper in Mesoporous Silica Nanoparticles as a Targeted Drug Delivery Platform', *Adv Funct Mater*, vol. 25, no. 6, pp. 957–965, Feb. 2015, doi: 10.1002/ADFM.201402755.

[127] Y. Wang *et al.*, 'Redox-responsive mesoporous silica as carriers for controlled drug delivery: A comparative study based on silica and PEG gatekeepers', *European Journal of Pharmaceutical Sciences*, vol. 72, pp. 12–20, May 2015, doi: 10.1016/J.EJPS.2015.02.008.

[128] G. Y. Tseng *et al.*, 'Control of Molecular Transport Through Stimuli-Responsive Ordered Mesoporous Materials', *Advanced Materials*, vol. 15, no. 15, pp. 1262–1266, Aug. 2003, doi: 10.1002/ADMA.200305165.

[129] H. Nsairat, D. Khater, U. Sayed, F. Odeh, A. Al Bawab, and W. Alshaer, 'Liposomes: structure, composition, types, and clinical applications', May 01, 2022, *Elsevier Ltd*. doi: 10.1016/j.heliyon.2022.e09394.

[130] S. Karaz and E. Senses, 'Liposomes Under Shear: Structure, Dynamics, and Drug Delivery Applications', *Adv Nanobiomed Res*, vol. 3, no. 4, p. 2200101, Apr. 2023, doi: 10.1002/ANBR.202200101.

[131] G. Bozzuto and A. Molinari, 'Liposomes as nanomedical devices', Feb. 02, 2015, *Dove Medical Press Ltd.* doi: 10.2147/IJN.S68861.

[132] A. I. Fernandes, A. F. Jozala, Y. Cao, X. Dong, and X. Chen, 'Polymer-Modified Liposomes for Drug Delivery: From Fundamentals to Applications', *Pharmaceutics 2022, Vol. 14, Page 778*, vol. 14, no. 4, p. 778, Apr. 2022, doi: 10.3390/PHARMACEUTICS14040778.

[133] K. Wang *et al.*, 'Protein liposomes-mediated targeted acetylcholinesterase gene delivery for effective liver cancer therapy', *J Nanobiotechnology*, vol. 19, no. 1, pp. 1–15, Dec. 2021, doi: 10.1186/S12951-021-00777-9/FIGURES/9.

[134] F. T. Doole, T. Kumarage, R. Ashkar, and M. F. Brown, 'Cholesterol Stiffening of Lipid Membranes', *The Journal of Membrane Biology 2022 255:4*, vol. 255, no. 4, pp. 385–405, Oct. 2022, doi: 10.1007/S00232-022-00263-9.

[135] X. Qiao, X. Wang, and X. Huang, 'Cholesterol-mediated functionalization of liposomes for artificial cell design', *Trends Chem*, vol. 6, no. 10, pp. 596–611, Oct. 2024, doi: 10.1016/J.TRECHM.2024.08.003/ASSET/C34F11F6-A506-49F0-851C-3C57DAA6990E/MAIN.ASSETS/GR6.SML.

[136] V. M. Katata, M. D. Maximino, C. Y. Silva, and P. Alessio, 'The Role of Cholesterol in the Interaction of the Lipid Monolayer with the Endocrine Disruptor Bisphenol-A', *Membranes (Basel)*, vol. 12, no. 8, p. 729, Aug. 2022, doi: 10.3390/MEMBRANES12080729/S1.

[137] H. Seo and H. Lee, 'Recent developments in microfluidic synthesis of artificial cell-like polymersomes and liposomes for functional bioreactors', *Biomicrofluidics*, vol. 15, no. 2, Mar. 2021, doi: 10.1063/5.0048441/134253.

[138] S. Andrade, M. J. Ramalho, J. A. Loureiro, and M. C. Pereira, 'Liposomes as biomembrane models: Biophysical techniques for drug-membrane interaction studies', *J Mol Liq*, vol. 334, p. 116141, Jul. 2021, doi: 10.1016/J.MOLLIQ.2021.116141.

[139] T. M. Allen and P. R. Cullis, 'Liposomal drug delivery systems: From concept to clinical applications', *Adv Drug Deliv Rev*, vol. 65, no. 1, pp. 36–48, Jan. 2013, doi: 10.1016/J.ADDR.2012.09.037.

[140] M. Dymek and E. Sikora, 'Liposomes as biocompatible and smart delivery systems – the current state', *Adv Colloid Interface Sci*, vol. 309, p. 102757, Nov. 2022, doi: 10.1016/J.CIS.2022.102757.

[141] F. Yanar, D. Carugo, and X. Zhang, 'Hybrid Nanoplatforms Comprising Organic Nanocompartments Encapsulating Inorganic Nanoparticles for Enhanced Drug Delivery and Bioimaging Applications', *Molecules 2023, Vol. 28, Page 5694*, vol. 28, no. 15, p. 5694, Jul. 2023, doi: 10.3390/MOLECULES28155694.

[142] V. De Leo, A. M. Maurelli, L. Giotta, and L. Catucci, 'Liposomes containing nanoparticles: preparation and applications', *Colloids Surf B Biointerfaces*, vol. 218, p. 112737, Oct. 2022, doi: 10.1016/J.COLSURFB.2022.112737.

[143] S. H. Park, S. G. Oh, J. Y. Mun, and S. S. Han, 'Loading of gold nanoparticles inside the DPPC bilayers of liposome and their effects on membrane fluidities', *Colloids Surf B Biointerfaces*, vol. 48, no. 2, pp. 112–118, Mar. 2006, doi: 10.1016/J.COLSURFB.2006.01.006.

[144] Z. Cai, Y. Zhang, Z. He, L. P. Jiang, and J. J. Zhu, 'NIR-Triggered Chemo-Photothermal Therapy by Thermosensitive Gold Nanostar@Mesoporous Silica@Liposome-Composited Drug Delivery Systems', *ACS Appl Bio Mater*, vol. 3, no. 8, pp. 5322–5330, Aug. 2020, doi: 10.1021/ACSABM.0C00651/ASSET/IMAGES/LARGE/MT0C00651_0007.JPEG.

[145] F. Han, A. H. Soeriyadi, S. R. C. Vivekchand, and J. J. Gooding, 'Simple Method for Tuning the Optical Properties of Thermoresponsive Plasmonic Nanogels', *ACS Macro Lett*, vol. 5, no. 5, pp. 626–630, May 2016, doi: 10.1021/ACSMACROLETT.6B00222/ASSET/IMAGES/LARGE/MZ-2016-002226_0005.JPEG.

[146] M. Molina, M. Asadian-Birjand, J. Balach, J. Bergueiro, E. Miceli, and M. Calderón, 'Stimuli-responsive nanogel composites and their application in nanomedicine', *Chem Soc Rev*, vol. 44, no. 17, pp. 6161–6186, Aug. 2015, doi: 10.1039/C5CS00199D.

[147] L. Tian *et al.*, 'Plasmonic Nanogels for Unclonable Optical Tagging', *ACS Appl Mater Interfaces*, vol. 8, no. 6, pp. 4031–4041, Feb. 2016, doi: 10.1021/ACSAMI.5B11399/ASSET/IMAGES/LARGE/AM-2015-113996_0001.JPEG.

[148] A. R. Girija and S. Balasubramanian, 'Theragnostic potentials of core/shell mesoporous silica nanostructures', 2019, *Ivyspring International Publisher*. doi: 10.7150/ntno.27877.

[149] X. Lian, J. Jin, J. Tian, and H. Zhao, 'Thermoresponsive nanohydrogels cross-linked by gold nanoparticles', *ACS Appl Mater Interfaces*, vol. 2, no. 8, pp. 2261–2268, Aug. 2010, doi: 10.1021/AM1003156/SUPPL_FILE/AM1003156_SI_001.PDF.

[150] Z. Zhu, D. Qi, Z. Z. Yang, Y. Wang, P. Müller-Buschbaum, and Q. Zhong, 'Nanogels Containing Gold Nanoparticles on Cotton Fabrics for Comfort Control via Localized Surface Plasmon Resonance', *ACS Appl Nano Mater*, vol. 7, no. 1, pp. 1222–1232, Jan. 2024, doi: 10.1021/ACSANM.3C05211/ASSET/IMAGES/LARGE/AN3C05211_0011.JPEG.

[151] J. Bergueiro, E. A. Glitscher, and M. Calderón, 'A hybrid thermoresponsive plasmonic nanogel designed for NIR-mediated chemotherapy', *Biomaterials Advances*, vol. 137, p. 212842, Jun. 2022, doi: 10.1016/J.BIOADV.2022.212842.

[152] N. Guarrotxena and I. Quijada-Garrido, 'Optical and Swelling Stimuli-Response of Functional Hybrid Nanogels: Feasible Route to Achieve Tunable Smart Core@Shell Plasmonic@Polymer Nanomaterials', *Chemistry of Materials*, vol. 28, no. 5, pp. 1402–1412, Mar. 2016, doi: 10.1021/ACS.CHEMMATER.5B04517/ASSET/IMAGES/LARGE/CM-2015-04517X_0009.JPEG.

[153] M. Enache, A. M. Toader, and M. I. Enache, 'Mitoxantrone-Surfactant Interactions: A Physicochemical Overview', *Molecules*, vol. 21, no. 10, Oct. 2016, doi: 10.3390/MOLECULES21101356.

[154] D. S. Alberts, Y. M. Peng, G. T. Bowden, W. S. Dalton, and C. Mackel, 'Pharmacology of mitoxantrone: mode of action and pharmacokinetics', *Invest New Drugs*, vol. 3, pp. 101–107, 1985.

[155] F. E. Durr, R. E. Wallace, and R. V. Citarella, 'Molecular and biochemical pharmacology of mitoxantrone', *Cancer Treat Rev*, vol. 10, no. SUPPL. B, pp. 3–8, Dec. 1983, doi: 10.1016/0305-7372(83)90016-6.

[156] E. J. Fox, 'Mechanism of action of mitoxantrone', *Neurology*, vol. 63, no. 12 SUPPL. 6, Dec. 2004, doi: 10.1212/WNL.63.12_SUPPL_6.S15.

[157] L. Deng, C. Zhang, S. Ying, B. Cai, and F. Zhou, 'Effect of Dose Ratio on Mitoxantrone and Daunorubicin in Acute Myeloid Leukemia: A Systematic Review and Meta-analysis of Randomized Controlled Trials', *Clin Lymphoma Myeloma Leuk*, vol. 21, no. 1, pp. e10–e20, Jan. 2021, doi: 10.1016/J.CLML.2020.08.001.

[158] L. J. Scott and D. P. Figgitt, 'Mitoxantrone: A review of its use in multiple sclerosis', *CNS Drugs*, vol. 18, no. 6, pp. 379–396, Aug. 2004, doi: 10.2165/00023210-200418060-00010/FIGURES/3.

[159] J. Zhao, B. J. Guercio, and D. Sahasrabudhe, 'Current Trends in Chemotherapy in the Treatment of Metastatic Prostate Cancer', *Cancers 2023, Vol. 15, Page 3969*, vol. 15, no. 15, p. 3969, Aug. 2023, doi: 10.3390/CANCERS15153969.

[160] I. E. Smith, R. Stuart-Harris, N. Pavlidis, and T. Bozek, 'Mitoxantrone (novantrone∗) as single agent and in combination chemotherapy in the treatment of advanced breast cancer', *Cancer Treat Rev*, vol. 10, no. SUPPL. B, pp. 37–40, Dec. 1983, doi: 10.1016/0305-7372(83)90020-8.

[161] R. A. Gams, J. W. Keller, H. M. Golomb, J. Steinberg, and G. Dukart, 'Mitoxantrone in malignant lymphomas', *Cancer Treat Rev*, vol. 10, no. SUPPL. B, pp. 69–72, Dec. 1983, doi: 10.1016/0305-7372(83)90026-9.

[162] D. Faulds, J. A. Balfour, P. Chrisp, and H. D. Langtry, 'Mitoxantrone', *Drugs 1991 41:3*, vol. 41, no. 3, pp. 400–449, Nov. 2012, doi: 10.2165/00003495-199141030-00007.

[163] A. Nakano *et al.*, 'Glycolysis Inhibition Inactivates ABC Transporters to Restore Drug Sensitivity in Malignant Cells', *PLoS One*, vol. 6, no. 11, p. e27222, Nov. 2011, doi: 10.1371/JOURNAL.PONE.0027222.

[164] I. C. Henderson *et al.*, 'Randomized clinical trial comparing mitoxantrone with doxorubicin in previously treated patients with metastatic breast cancer.', *Journal of Clinical Oncology*, vol. 7, no. 5, pp. 560–571, 1989, doi: 10.1200/JCO.1989.7.5.560.

[165] R. M. Damiani, D. J. Moura, C. M. Viau, R. A. Caceres, J. A. P. Henriques, and J. Saffi, 'Pathways of cardiac toxicity: comparison between chemotherapeutic drugs doxorubicin and mitoxantrone', *Archives of Toxicology 2016 90:9*, vol. 90, no. 9, pp. 2063–2076, Jun. 2016, doi: 10.1007/S00204-016-1759-Y.

[166] M. Akram, 'Mini-review on glycolysis and cancer', *Journal of Cancer Education*, vol. 28, no. 3, pp. 454–457, Sep. 2013, doi: 10.1007/S13187-013-0486-9/METRICS.

[167] D. Zhang, J. Li, F. Wang, J. Hu, S. Wang, and Y. Sun, '2-Deoxy-D-glucose targeting of glucose metabolism in cancer cells as a potential therapy', *Cancer Lett*, vol. 355, no. 2, pp. 176–183, Dec. 2014, doi: 10.1016/J.CANLET.2014.09.003.

[168] J. W. Wojtkowiak, D. Verduzco, K. J. Schramm, and R. J. Gillies, 'Drug resistance and cellular adaptation to tumor acidic pH microenvironment', *Mol Pharm*, vol. 8, no. 6, pp. 2032–2038, Dec. 2011, doi: 10.1021/MP200292C/SUPPL_FILE/MP200292C_SI_001.PDF.

[169] N. S. Chandel, 'Glycolysis', *Cold Spring Harb Perspect Biol*, vol. 13, no. 5, p. a040535, May 2021, doi: 10.1101/CSHPERSPECT.A040535.

[170] Jyostna Bere, N. Dharani Jonnalagadda, L. Kappari, J. Karangula, N. Boggula, and V. Kappari, '2-DEOXY-D-GLUCOSE: AN UPDATE REVIEW', *Journal For Innovative Development in Pharmaceutical and Technical Science (JIDPTS)*, vol. 4, no. 5, 2021, Accessed: Mar. 24, 2025. [Online]. Available: www.jidps.com

[171] B. Pajak *et al.*, '2-Deoxy-d-Glucose and Its Analogs: From Diagnostic to Therapeutic Agents', *International Journal of Molecular Sciences 2020, Vol. 21, Page 234*, vol. 21, no. 1, p. 234, Dec. 2019, doi: 10.3390/IJMS21010234.

[172] J. Zhu, Y. Zheng, H. Zhang, and H. Sun, 'Targeting cancer cell metabolism: The combination of metformin and 2-Deoxyglucose regulates apoptosis in ovarian cancer cells via p38 MAPK/JNK signaling pathway', *Am J Transl Res*, vol. 8, no. 11, p. 4812, 2016, Accessed: Mar. 25, 2025. [Online]. Available: https://pmc.ncbi.nlm.nih.gov/articles/PMC5126324/

[173] M. Stein *et al.*, 'Targeting tumor metabolism with 2-deoxyglucose in patients with castrate-resistant prostate cancer and advanced malignancies', *Prostate*, vol. 70, no. 13, pp. 1388–1394, Sep. 2010, doi: 10.1002/PROS.21172.

[174] I. M. Ahmad, E. H. Mustafa, N. H. Mustafa, L. H. Tahtamouni, and M. Y. Abdalla, '2DG enhances the susceptibility of breast cancer cells to doxorubicin', *Cent Eur J Biol*, vol. 5, no. 6, pp. 739–748, Jul. 2010, doi: 10.2478/S11535-010-0060-Y/METRICS.

[175] O. N. Orobator, R. T. Mertens, O. A. Obisesan, and S. G. Awuah, 'Energy and endoplasmic reticulum stress induction by gold(III) dithiocarbamate and 2-deoxyglucose synergistically trigger cell death in breast cancer', *Journal of Biological Chemistry*, vol. 300, no. 12, Dec. 2024, doi: 10.1016/J.JBC.2024.107949/ATTACHMENT/7D8D530A-4131-444A-A02B-45975EC078CC/MMC1.DOCX.

[176] R. L. Aft, F. W. Zhang, and D. Gius, 'Evaluation of 2-deoxy-D-glucose as a chemotherapeutic agent: mechanism of cell death', *British Journal of Cancer 2002 87:7*, vol. 87, no. 7, pp. 805–812, Sep. 2002, doi: 10.1038/sj.bjc.6600547.

[177] A. N. Bhatt *et al.*, '2-deoxy-d-glucose as an adjunct to standard of care in the medical management of COVID-19: a proof-of-concept and dose-ranging randomised phase II clinical trial', *BMC Infect Dis*,

vol. 22, no. 1, pp. 1–10, Dec. 2022, doi: 10.1186/S12879-022-07642-6/TABLES/4.

[178] A. E. Papathanassiu, N. J. MacDonald, D. R. Emlet, and H. A. Vu, 'Antitumor activity of efrapeptins, alone or in combination with 2-deoxyglucose, in breast cancer in vitro and in vivo', *Cell Stress Chaperones*, vol. 16, no. 2, pp. 181–193, Mar. 2011, doi: 10.1007/S12192-010-0231-9.

[179] P. Sun *et al.*, 'Phenylboronic Acid-Modified Near-Infrared Region II Excitation Donor–Acceptor–Donor Molecule for 2-Deoxy-d-Glucose Improved Starvation/Chemo/Photothermal Combination Therapy', *Adv Healthc Mater*, vol. 12, no. 30, p. 2302099, Dec. 2023, doi: 10.1002/ADHM.202302099.

[180] C. M. J. Hu and L. Zhang, 'Nanoparticle-based combination therapy toward overcoming drug resistance in cancer', *Biochem Pharmacol*, vol. 83, no. 8, pp. 1104–1111, Apr. 2012, doi: 10.1016/J.BCP.2012.01.008.

[181] R. B. Mokhtari *et al.*, 'Combination therapy in combating cancer', *Oncotarget*, vol. 8, no. 23, p. 38022, 2017, doi: 10.18632/ONCOTARGET.16723.

[182] R. N. Woodring, E. G. Gurysh, E. M. Bachelder, and K. M. Ainslie, 'Drug Delivery Systems for Localized Cancer Combination Therapy', *ACS Appl Bio Mater*, vol. 6, no. 3, pp. 934–950, Mar. 2023, doi: 10.1021/ACSABM.2C00973/ASSET/IMAGES/LARGE/MT2C00973_0005.JPEG.

[183] Y. Li, S. Chen, X. Chang, F. He, and R. Zhuo, 'Efficient Co-delivery of Doxorubicin and Methotrexate by pH-Sensitive Dual-Functional Nanomicelles for Enhanced Synergistic Antitumor Efficacy', *ACS Appl Bio Mater*, vol. 2, no. 5, pp. 2271–2279, May 2019, doi: 10.1021/ACSABM.9B00230/ASSET/IMAGES/MEDIUM/MT-2019-00230V_M002.GIF.

[184] N. Feng *et al.*, 'Strategically engineered Au(I) complexes for orchestrated tumor eradication via chemo-phototherapy and induced

immunogenic cell death', *Nature Communications 2024 15:1*, vol. 15, no. 1, pp. 1–18, Sep. 2024, doi: 10.1038/s41467-024-52458-4.

[185] J. Yi *et al.*, 'Advances and perspectives in phototherapy-based combination therapy for cancer treatment', *J Mater Chem B*, vol. 12, no. 26, pp. 6285–6304, Jul. 2024, doi: 10.1039/D4TB00483C.

[186] M. Li *et al.*, 'NIR/pH-triggered aptamer-functionalized DNA origami nanovehicle for imaging-guided chemo-phototherapy', *J Nanobiotechnology*, vol. 21, no. 1, pp. 1–14, Dec. 2023, doi: 10.1186/S12951-023-01953-9/FIGURES/7.

[187] F. G. L. Medeiros Borsagli, I. C. Carvalho, and H. S. Mansur, 'Amino acid-grafted and N-acylated chitosan thiomers: Construction of 3D bio-scaffolds for potential cartilage repair applications', *Int J Biol Macromol*, vol. 114, pp. 270–282, Jul. 2018, doi: 10.1016/j.ijbiomac.2018.03.133.

[188] J. Petiti, L. Revel, and C. Divieto, 'Standard Operating Procedure to Optimize Resazurin-Based Viability Assays', *Biosensors (Basel)*, vol. 14, no. 4, p. 156, Apr. 2024, doi: 10.3390/BIOS14040156/S1.

[189] S. S. Verma and J. S. Sekhon, 'Influence of aspect ratio and surrounding medium on localized surface plasmon resonance (LSPR) of gold nanorod', *Journal of Optics (India)*, vol. 41, no. 2, pp. 89–93, Jun. 2012, doi: 10.1007/S12596-012-0068-Y/FIGURES/3.

[190] J. Pérez-Juste, I. Pastoriza-Santos, L. M. Liz-Marzán, and P. Mulvaney, 'Gold nanorods: Synthesis, characterization and applications', *Coord Chem Rev*, vol. 249, no. 17–18, pp. 1870–1901, Sep. 2005, doi: 10.1016/J.CCR.2005.01.030.

[191] L. Bianchi *et al.*, 'Thermal analysis of laser irradiation-gold nanorod combinations at 808 nm, 940 nm, 975 nm and 1064 nm wavelengths in breast cancer model', *International Journal of Hyperthermia*, vol. 38, no. 1, pp. 1099–1110, 2021, doi: 10.1080/02656736.2021.1956601.

[192] C. Wu and Q. H. Xu, 'Stable and functionable mesoporous silica-coated gold nanorods as sensitive localized surface plasmon

resonance (LSPR) nanosensors', *Langmuir*, vol. 25, no. 16, pp. 9441–9446, Aug. 2009, doi: 10.1021/LA900646N/SUPPL_FILE/LA900646N_SI_001.PDF.

[193] X. Huang, I. H. El-Sayed, W. Qian, and M. A. El-Sayed, 'Cancer cell imaging and photothermal therapy in the near-infrared region by using gold nanorods', *J Am Chem Soc*, vol. 128, no. 6, pp. 2115–2120, Feb. 2006, doi: 10.1021/JA057254A/ASSET/IMAGES/LARGE/JA057254AF00003.JPEG.

[194] C. Shan, Y. Huang, J. Wei, M. Chen, and L. Wu, 'Ultra-high thermally stable gold nanorods/radial mesoporous silica and their application in enhanced chemo-photothermal therapy', *RSC Adv*, vol. 11, no. 18, pp. 10416–10424, Mar. 2021, doi: 10.1039/d1ra00213a.

[195] G. Lawrie *et al.*, 'Interactions between alginate and chitosan biopolymers characterized using FTIR and XPS', *Biomacromolecules*, vol. 8, no. 8, pp. 2533–2541, Aug. 2007, doi: 10.1021/BM070014Y/ASSET/IMAGES/LARGE/BM070014YF00009.JPEG.

[196] A. Zając, J. Hanuza, M. Wandas, and L. Dymińska, 'Determination of N-acetylation degree in chitosan using Raman spectroscopy', *Spectrochim Acta A Mol Biomol Spectrosc*, vol. 134, pp. 114–120, Jan. 2015, doi: 10.1016/J.SAA.2014.06.071.

[197] N. Singh, S. K. Anand, A. Sharma, S. Singh, P. Kakkar, and V. Srivastava, 'Chitosan/alginate nanogel potentiate berberine uptake and enhance oxidative stress mediated apoptotic cell death in HepG2 cells', *Int J Biol Macromol*, vol. 257, p. 128717, Feb. 2024, doi: 10.1016/J.IJBIOMAC.2023.128717.

[198] X. D. Ren, Q. S. Liu, H. Feng, and X. Y. Yin, 'The Characterization of Chitosan Nanoparticles by Raman Spectroscopy', *Applied Mechanics and Materials*, vol. 665, pp. 367–370, 2014, doi: 10.4028/WWW.SCIENTIFIC.NET/AMM.665.367.

[199] P. Rodríguez-Zamora *et al.*, 'Revisiting the conformational adsorption of L- and D-cysteine on Au nanoparticles by Raman spectroscopy', *Journal of Raman Spectroscopy*, vol. 51, no. 2, pp. 243–255, Feb. 2020, doi: 10.1002/JRS.5782.

[200] C. Pan, J. Qian, C. Zhao, H. Yang, X. Zhao, and H. Guo, 'Study on the relationship between crosslinking degree and properties of TPP crosslinked chitosan nanoparticles', *Carbohydr Polym*, vol. 241, p. 116349, Aug. 2020, doi: 10.1016/J.CARBPOL.2020.116349.